ChemCatChem

Review
doi.org/10.1002/cctc.202501109

Chemistry Europe
European Chemical Societies Publishing

www.chemcatchem.org

Engineering Catalysts at the Multiscale: Past, Present, and Future of Catalyst Manufacturing and Shaping Processes

Ali M. Alkadhem,[a] Eduardo Perez-Botella,[b] Swantje Pietsch-Braune,[c] Hend Omar Mohamed,[a] Carlos A. Grande,[b, d] Stefan Heinrich,[c] and Pedro Castaño*[a, d]

Catalyst shaping is pivotal in optimizing catalytic performance across industrial chemical processes. The engineering of catalysts at multiple scales, ranging from nano to macro, has considerably evolved over the years, driven by advancements in shaping technology. We explore the progression of catalyst shaping, beginning with traditional methods, such as pelletizing and granulation, and advancing to modern techniques, including extrusion, spray-drying, fluidized-bed processes, and additive manufacturing (AM). This work emphasizes shaping technology tailored to specific reactor types, such as fixed-bed (up to structured catalyst) and fluidized-bed reactors. We highlight critical parameters to optimize and control catalyst properties and their direct influence on enhancing catalyst durability, activity, and selectivity. Advances in computational modeling, including multiscale simulations and machine learning-driven design, have further revolutionized catalyst shaping by enabling precise control and accelerating innovation. This review offers a comprehensive perspective on the future of multiscale catalyst shaping and underscores its potential to drive enhanced catalytic performance and sustainable chemical processes by analyzing historical developments, current trends, and emerging technology.

1. Introduction

Catalysts are essential for producing many of society's daily needs. An estimated 90% of the chemicals currently produced involve catalysts, most using heterogeneous catalysts.[1,2] In 2021, the market for industrial catalysts was valued at 21.6 billion USD, and it is anticipated to reach 27.9 billion USD by 2027.[3] Catalysts are fundamental to modern chemical processes, playing a crucial role in enhancing reaction efficiency, reducing energy consumption, and improving selectivity. A catalyst accelerates a chemical reaction without being consumed. By lowering the activation energy, catalysts enable reactions to proceed at lower temperatures and pressures, improving economic and environmental sustainability.[4]

Moreover, catalysts must meet stringent criteria, including chemical and mechanical stability, for industrial and commercial applications while maintaining consistent performance.[5] Catalysts are manufactured in various shapes, such as extrudates, tablets, spheres, and granules, optimized for compatibility with various catalytic processes to achieve these requirements.[6] These shapes can be achieved using state-of-the-art technology, including extrusion,[7] palletization,[8] spray-drying,[9] fluidized-bed spray-drying,[10] and 3D printing.[11]

Extrusion is the most common technique for catalyst shaping, owing to its operational efficiency and the ease of producing extrudates compared to alternative forms.[12] However, extrusion can be energy-intensive and limited to specific shapes and sizes. One of the challenges associated with extrusion is achieving uniformity in the catalyst composition and pore structure.[13,14]

Pelletizing is commonly employed as a preliminary forming method to prepare samples for catalyst testing in fixed-bed microreactors, starting from powders. After pelletizing, the pellets are typically crushed and sieved according to the reactor diameter requirements. Dry shaping through pelletization is generally easier to perform than wet shaping (extrusion), but it presents challenges. For instance, when applied to mesoporous materials, dry extrusion can cause a loss of surface area and porosity. These drawbacks should be considered when selecting the appropriate shaping method for catalyst preparation.[13,15]

The spray-drying process has emerged as a common technique for producing well-structured porous particles with a controlled particle size and morphology, ranging from the nano- to submicrometer scale.[16,17] Spray-drying has applications in diverse fields, such as food production,[18] cosmetics,[19] fertilization,[20] and pharmaceutical applications (e.g., drug coating).[21,22] Spray-drying is prominent owing to its low waste generation, significantly enhancing

[a] A. M. Alkadhem, H. O. Mohamed, P. Castaño
Multiscale Reaction Engineering (MuRE), King Abdullah University of Science and Technology (KAUST), Thuwal 23955-6900, Saudi Arabia
E-mail: pedro.castano@kaust.edu.sa

[b] E. Perez-Botella, C. A. Grande
Intensification of Materials and Processes Laboratory, Physical Sciences and Engineering Division, King Abdullah University of Science and Technology (KAUST), Thuwal 23955-6900, Saudi Arabia

[c] S. Pietsch-Braune, S. Heinrich
Institute of Solids Process Engineering and Particle Technology, Hamburg University of Technology, Denickestraße 15 21073, Hamburg, Germany

[d] C. A. Grande, P. Castaño
Chemical Engineering Program, Physical Science and Engineering (PSE) Division, King Abdullah University of Science and Technology, Saudi Arabia

Dr. Ali M. Alkadhem is a Postdoctoral Researcher at King Abdullah University of Science and Technology (KAUST). He holds a Ph.D. in Chemical Engineering from KAUST, specializing in heterogeneous catalysis, catalyst shaping, extrusion, and fluidized-bed technologies. His research focuses on developing technical catalysts for sustainable energy applications, including methanol-to-hydrocarbon conversion, steam reforming, photocatalytic H^2S decomposition, methane pyrolysis, and CO^2 utilization, integrating experimental design, reactor modeling, and data-driven approaches for performance optimization.

Dr. Eduardo Pérez-Botella graduated in Chemistry from the Universitat de Valéncia in 2015. He completed his PhD in 2021 at the ITQ, supervised by Fernando Rey and Susana Valencia, focusing on zeolites for gas adsorption and separation. He then worked as a postdoc with Joeri Denayer at VUB (20222023) and Carlos Grande at KAUST (20232025). Currently, he is the Laboratory Manager at Refractarios Especiales S.A., located in Riba-Roja, Valencia, Spain.

Dr.-Ing. Swantje Pietsch-Braune is a senior engineer in the Institute of Solids Process Engineering and Particle Technology at Hamburg University of Technology. She obtained her PhD in 2018 on the experimental and numerical investigations of fluidization behaviour and liquid injection in three-dimensional prismatic spouted beds. Her research is focused on particle formation in fluidized beds and CFD-DEM simulations of these processes.

Dr. Hend Omar Mohamed is a Research Scientist at the KAUST Catalysis Platform, King Abdullah University of Science and Technology (KAUST), Saudi Arabia. She obtained her Ph.D. in Bionanosystem Engineering from Chonbuk National University, South Korea. Her research spans the design of nanostructured and hybrid 2D catalysts to integrated electrochemical systems for CO_2 conversion, hydrogen production, and wastewater treatment. Her work bridges electrocatalysis and materials engineering, resulting in over 70 publications and international recognition, including the MIT Innovators Under 35 MENA award.

Carlos A. Grande is an Associate Professor in KAUST since September 2021. He graduated in Chemical Engineering from South University (Argentina) in 1998. He obtained his PhD in 2005 from Porto University (Portugal), where he also worked as a research assistant for 5 years. He worked in SINTEF Industry (Norway) as a Senior Scientist for 10 years. He leads the Intensification of Materials and Processes (IMAP) laboratory where process intensification is applied to separation and reaction processes with strong focus on adsorption and 3D printing.

Prof. Stefan Heinrich obtained his diploma in Process Engineering and a doctoral degree and a habilitation at the University of Magdeburg. In 2008, he became full professor and director of the Institute of Solids Process Engineering and Particle Technology at Hamburg University of Technology. He is editor of "Advanced Powder Technology" and "Particuology" and chairman of the EFCE Working Party on Agglomeration. His main research interests are fluidized bed technology and multiscale particle simulation methods. He received the 2015 DECHEMA-Prize and the 2025 Shell Thomas Baron Award.

Prof. Pedro Castaño is Professor of Chemical Engineering at KAUST, leading the Multiscale Reaction Engineering (MuRE) group. He completed his PhD in Chemical Engineering in 2006 from the University of the Basque Country (UPV/EHU). His research bridges catalysis, kinetic modeling, and reactor design to develop intesified or sustainable processes for coverting waste, pollutants or secondary products into fuels and chemicals. More information can be found at https://mure.kaust.edu.sa

its appeal for industrial applications.[23] Consequently, over 15,000 spray-drying processes have recently been implemented worldwide, underscoring its widespread adoption and industrial relevance.[24]

Despite the significant contributions of spray-drying to heterogeneous catalysis, the method is constrained by its ability to shape active catalyst components into spherical particles, specifically in the 40 to 100 μm size range.[9] This limitation highlights the need for further optimization or incorporating complementary shaping techniques to meet specific application requirements. Spray-fluidized beds have emerged as a promising technology for shaping technical catalysts as an alternative approach for catalyst shaping into a spherical shape, with a wide range of particle sizes from a few micrometers to millimeters. The spray-fluidized bed technique is a pivotal method for particle granulation and coating, enabling the production of large quantities of particles with precise and controlled sizes.[25] The spray-fluidized bed technique is widely used in the pharmaceutical industry for drug coating because it effectively controls drug release and enhances stability and mechanical resistance. This versatile process is extensively employed to produce food products, detergents, and agricultural chemicals, highlighting its broad applicability across sectors.[26,27]

Three-dimensional (3D) printing technology, also known as additive manufacturing (AM), has gained considerable attention due to its ability to produce complex 3D structures quickly. This technology builds complex structures layer-by-layer, guided by digital model files.[11] Some examples of commercial catalysts prepared by 3D printing are BASF's O4-115×3D® and O3-85×3D® catalysts for sulfuric acid production and N_2O abatement, respectively.[28] Shell's catalysts for gas-to-liquids (GTL) technology and environmental applications are not openly commercial, but their interest and activity in the field indicate they might be pilot-scale.[29] These and other companies, such as Vito, offer their technology and expertise for custom 3D-printed catalysts development.[30] The primary categories of 3D printing include techniques based on material extrusion, vat photopolymerization, and powder bed fusion, each encompassing several methods.[31,32]

Preparing appropriate feedstock involves using suitable solvents and additives to make catalysts suitable for 3D printing. In some cases, post-processing treatments are necessary to achieve the final product. A critical challenge in 3D-printing catalysts is the need to preserve the structure of the catalyst particles during the ink formulation process. The active species can decompose or react with other ink components, such as binders, plasticizers, or solvents, affecting the catalyst activity.[33] Therefore, attention and specialized techniques are necessary to maintain the structural and functional integrity of the catalyst throughout the 3D-printing process.

This review explores the evolution of catalyst-shaping methods from traditional techniques (e.g., pelletizing and granulation) to advanced approaches (e.g., extrusion, spray-drying, fluidized-bed processes, and AM). First, it presents a general overview of catalysts, multiscale considerations, and performance metrics for optimal catalyst design. Second, this work focuses on past developments, current trends, and future directions of catalyst-shaping technology and its optimization in shaping catalysts at various scales. The focus is on how these shaping techniques are tailored for multiple reactor configurations, including fixed-bed and fluidized-bed reactors, and their influence on catalyst properties, such as durability, activity, and selectivity.

Third, the role of computational modeling spanning multiscale simulations and machine learning (ML)-driven design in optimizing catalyst shaping is discussed. By examining historical advancements, current trends, and emerging innovations, this review aims to reach a comprehensive understanding of catalyst-shaping technology and its potential to enhance catalytic performance and promote sustainable chemical processes.

2. Background

2.1. Overview of Catalyst Manufacturing

Catalysts are generally classified into four categories: homogeneous, heterogeneous, biocatalysts, and electrocatalysts.[34] Homogeneous catalysts exist in the same form as reactants, typically liquid or gaseous, enabling uniform interaction and reaction kinetics. A prominent example is sulfuric acid (H_2SO_4), which is widely employed in esterification reactions.[35,36] In contrast, heterogeneous catalysts operate in a different phase than the reactants, commonly as solids in liquid- or gas-phase reactions. For instance, zeolite-based catalysts play a critical role in fluid catalytic cracking (FCC) in petroleum refining, facilitating the conversion of heavy hydrocarbons into valuable products.[37,38]

Biocatalysts, primarily enzymes, are naturally occurring catalysts that exhibit high specificity under mild conditions. For example, amylase is extensively used in the food industry for starch hydrolysis.[39,40] Electrocatalysts are integral to electrochemical processes, such as fuel cells and water splitting for hydrogen (H_2) production. A notable example is platinum (Pt)-based catalysts, which are commonly employed in proton-exchange-membrane fuel cells due to their superior efficiency in electrochemical energy conversion.[41]

Catalysts are essential across diverse industries and are pivotal in enhancing efficiency, sustainability, and economic viability.[42] In refining processes, catalysts facilitate chemical reactions by improving the reaction rates and selectivity, minimizing the need for extreme operating conditions, such as high temperatures, elevated pressures, or prolonged reaction times. In the petrochemical sector, catalysts are widely employed in critical processes, such as cracking and reforming.[43] Notably, zeolite-based catalysts in FCC enable the conversion of heavy hydrocarbons into high-value products, including gasoline and olefins, optimizing product yield and process efficiency.[44,45] In the hydrotreating process, nickel–molybdenum (Ni–Mo) catalysts often remove sulfur from fuels and reduce environmental pollution.[46,47] Catalysts essential for fertilizer production, such as ammonia (NH_3) synthesis in the Haber process, rely on iron-based catalysts to convert nitrogen (N_2) and hydrogen (H_2) into NH_3.[48] In methanol (CH_3OH) production (a critical component in chemical feedstock and fuel applications), copper–zinc (Cu–

Zn) catalysts are vital in enabling the efficient hydrogenation of carbon dioxide (CO_2) into CH_3OH.[49,50]

Catalysts are widely employed in environmental applications, notably in catalytic converters, where Pt-group metals –ruthenium (Ru), rhodium (Rh), palladium (Pd), osmium (Os), iridium (Ir), and Pt– are used in vehicle exhaust systems to minimize emissions of nitrogen oxides (NO_x), carbon monoxide (CO), and hydrocarbons.[51,52] Photocatalysis for water purification employs titanium dioxide (TiO_2) photocatalysts to decompose organic pollutants in wastewater treatment.[53] In sustainable energy and green chemistry, catalysts play a vital role in H_2 production, where Ni-based catalysts in steam methane (CH_4) reforming represent a critical technology.[54,55] Carbon capture and utilization are enhanced by metal–organic frameworks (MOFs) that help convert CO_2 into valuable chemicals, reducing greenhouse gas emissions.[56–58] Fuel cells use Pt-based electrocatalysts to provide clean energy solutions.[59] Catalysts are indispensable in modern chemical industries, enabling efficient, cost-effective, and environmentally sustainable processes. Advances in catalyst design, including catalyst shaping, particularly for heterogeneous catalysts, continue to drive innovation in industrial applications.

2.2. Multiscale Catalyst Engineering

In the multiscale catalyst design framework, distinguishing between catalysts used in a research laboratory and technical (industrial) catalysts is crucial because their structural characteristics, performance expectations, and operational environments significantly differ across scales. Catalysts used in a research laboratory are typically synthesized as fine powders, often comprising a single active phase in bulk or supported on a high-surface-area substrate. These formulations are primarily optimized to evaluate intrinsic activity and selectivity under idealized laboratory conditions and serve to uncover fundamental structure–activity relationships.[7,60]

However, transitioning from the laboratory to real-world industrial applications demands a more comprehensive approach spanning multiple hierarchical scales, encompassing nano-, micro-, meso-, and macrostructural features.[61] In the conventional catalyst development pipeline in Figure 1, most candidate materials are systematically screened and rejected during the primary and secondary evaluation stages due to various problems, such as poor thermal stability, low reproducibility, or suboptimal performance, under process-relevant conditions. Only a few successful catalyst developments progress to the scaling-up stage, where they are transformed into technical catalyst-engineered forms, such as pellets, extrudates, or monoliths, designed to withstand industrial demands, such as mechanical stress, thermal gradients, and mass/heat transfer limitations.[62,63]

A multiscale design strategy integrates insight from atomistic modeling and surface chemistry at the nanoscale via porosity and diffusional optimization at the mesoscale and reactor-level considerations at the macroscale. Engineering catalysts across these hierarchical levels permits the optimization of reactivity, selectivity, stability, and process efficiency.[64] The implications at different scales are the following:

- At the nanoscale, catalysts have unique electronic and surface properties critical for catalytic functions. For instance, nanoparticles offer a high surface-area-to-volume ratio, increasing the number of available active sites.[65] The size, shape, and facet exposure of nanoparticles can profoundly influence catalytic behavior, as observed in Pt-based fuel cell catalysts, where morphology control enhances the activity and durability.[41,66]
- At the microscale, structuring plays a vital role in mass transport and thermal management. Microstructure catalysts, such as hierarchical zeolites, are engineered to enhance diffusion and reduce deactivation due to pore blockage, extending catalytic lifetimes in high-throughput petrochemical processes.[67,68]
- Mesoscale engineering involves tailoring pore architectures and support materials to ensure efficient reactant access and long-term catalyst stability. Supports (e.g., mesoporous silica) offer tunable porosity and facilitate molecular transport in complex reactions, including CH_3OH-to-olefin conversions.[69,70]
- At the macroscale, catalyst placement in reactors and the overall reactor design significantly influence conversion rates and process efficiency. Structured catalysts, such as monolithic supports in automotive catalytic converters, improve mass and heat transfer, reduce pressure decrements, and enhance flow dynamics.[71] In large-scale industrial operations, such as NH_3 synthesis in the Haber process, catalyst pellet design is optimized to balance activity with fluid dynamics and heat distribution.[72,73]

By integrating the catalyst design across all scales, from the atomic to the reactor level, multiscale engineering enables a more rational and effective translation of research breakthroughs into industrial practice. This holistic approach allows precise control over the reaction environment, driving improvements in selectivity, conversion efficiency, catalyst lifetime, and overall process sustainability.[74]

Moreover, catalyst evolution across scales shows clear performance trade-offs (Table 1). At the nano-scale, shaping induces slight metal growth (Ni from ~5 to ~7 nm) and BET loss, lowering intrinsic activity.[69] At the micro-scale, binder-induced compaction increases tortuosity (~3.75) and decreases effectiveness factors ($\eta \sim 0.2$–0.35), highlighting diffusion limitations.[75] The meso-scale introduces pellet geometry effects, where ~3 mm extrudates with engineered pores balance porosity retention but still raise internal resistance.[76] Finally, at the macro-scale, reactor packing governs hydrodynamics (Pe ~ 1–10), where axial dispersion and pressure drop constrain scale-up.[77,78] Together, these insights demonstrate how properties evolve from powder to reactor, quantitatively linking structure to performance.

2.3. Evolution of Catalyst Shaping

Developing macroscopic catalysts from powder catalysts with shapes ranging from a few micrometers to several centime-

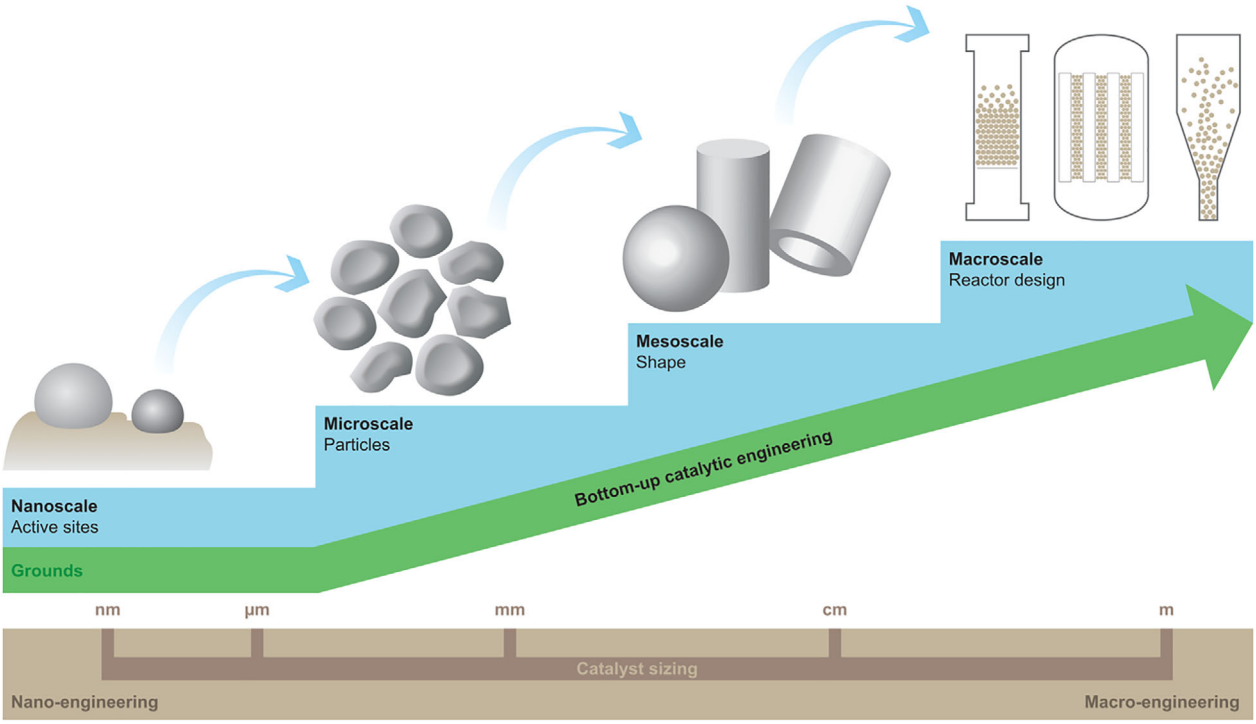

Figure 1. Scale of catalyst development from the laboratory catalyst development to technical catalysts.

Table 1. Multiscale relationships between catalyst properties and reactor performance.

Scale	Property	General trend across shaping	Case study: Ni/Al_2O_3 extrudates[79]	Performance link	Ref.
Nano	Active sites, particle size, surface area	Metal sintering or growth during shaping reduces dispersion; BET area decreases slightly.	Metal particle size increases from ~5 nm (powder) to ~7 nm (extrudates); BET decreases from ~200→150 m^2/g.	Fewer active sites per gram lowers intrinsic activity.	[69]
Micro	Pore size distribution, tortuosity, η	Binder addition decreases porosity; tortuosity increases; η decreases due to diffusion resistance.	Tortuosity measured ~3.75 in extrudates vs ~3.56 predicted; η decreases to ~0.19–0.35.	Internal diffusion limits cause sharp drop in catalyst effectiveness.	[75]
Meso	Pellet size, porosity, Thiele modulus	Larger pellets (2–5 mm) increase φ >1, lowering η; trilobes/engineered pores mitigate ΔP.	Extrudates ~3 mm diameter, with hierarchical pores engineered to improve effectiveness.	Larger pellet geometry increases internal diffusion resistance.	[76]
Macro	Reactor geometry, packing, axial dispersion (Pe)	Reactor hydrodynamics governed by Pe (1–10); smaller pellets reduce ΔP but risk attrition.	Fixed-bed packed with Ni/Al_2O_3 extrudates → Pe ≈ 1–10; ΔP on order of several kPa/m.	Axial dispersion reduces plug-flow behavior; ΔP limits scale-up.	[77, 78]

φ: Thiele modulus, η: effectiveness factor, BET: Brunauer–Emmett–Teller surface area, Pe: peclet number.

ters requires certain implementation steps, such as modifying laboratory procedures to produce multiple tons and choosing proper catalyst compositions (i.e., the type and ratio of component phases).[13,80] The technical catalysts comprise multicomponent elements, including the active material responsible for the reaction acceleration and additives to provide mechanical strength, facilitate mass and heat transfer, and enhance chemical stability.[7,60] The additives commonly applied to the technical catalyst are binders, peptizing agents, plasticizers, and lubricants.[60,81] Figure 2 illustrates an example of the ratio of components and additives integrated into shaped catalyst bodies, each chosen for its specific role, with the primary goal of enhancing mechanical strength, thermal conductivity, and catalytic activity. The binders improve the mechanical strength of the shaped catalysts.[5] Incorporating inorganic binders into the shaping process can significantly alter the properties of the resulting technical catalyst. For instance, using alumina as a binder can impart the Lewis acidity of the catalyst.

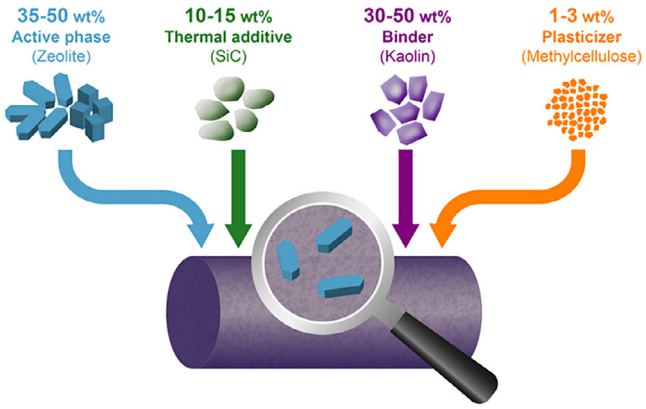

Figure 2. Example of the ratio of components and additives incorporated into shaped catalyst bodies.

Additionally, the mechanical forces exerted during catalyst shaping, as in extrusion, can modify the acidity of the catalytically active phase, potentially affecting the distribution and strength of the acid sites. These changes can have crucial implications for the overall catalyst performance.[82] Peptizing agents, such as acetic, nitric, and citric acid, improve homogeneity and disperse particles.[83] Plasticizing agents and lubricants (e.g., glycol and methyl cellulose) have the same roles and are employed in catalyst formulations to facilitate catalyst shaping due to viscosity reduction, specifically in the extrusion process.[84] At the same time, plasticizing agents can affect mechanical strength due to the creation of dispersed porosity. The shaping process and matrix design choice can significantly affect the final catalyst performance for the better or worse. The effect of the interplay between the active phase and additive material should be considered in academic research and must be well understood. The effects of binder and additive material interactions with the active phase catalyst have recently been reviewed.[85–87]

The development of an extrudate ZSM-5-based catalyst using a novel aluminophosphate binder for the CH_3OH-to-propylene (C_3H_6) reaction was achieved.[88] The new amorphous binder enhances the mechanical strength and maintains the total acidity of the zeolite with a definite decrease in the strong acidity due to the interaction of the phosphate with zeolite, minimizing the side reaction and enhancing the catalyst selectivity toward C_3H_6 at an optimized amount.

The Pérez–Ramírez group studied the effect of scaling up zeolite from powder to a technical catalyst for the methanol to hydrocarbons reaction.[89] They considered various binders, including silica, boehmite, kaolin, and attapulgite. They concluded that the zeolite interaction with attapulgite and kaolin increases the microporosity and enhances mass transfer due to the larger particle size. The acidity varies due to the zeolite partial dealumination or ion exchange, reducing the intrinsic catalyst activity. They observed no direct correlation with the selectivity or catalyst lifetime (see comprehensive reviews for further studies on the influence of binders and catalyst formulation on technical catalyst performance[60,90]). Similar outcomes were observed in our recent work,[91] where NH_3-TPD was employed to evaluate the total acidity, while pyridine-FTIR was used to differentiate and quantify Lewis and Brønsted acid sites. Moreover, the accessibility of these sites was found to vary among the different catalysts.

2.4. Shaping Technology Based on Reactor Type

Catalyst shaping is critical in optimizing performance and addressing specific challenges associated with packed and fluidized-bed reactors. Several factors influence particle shape selection for particular applications: active surface area per unit volume, structural integrity, ease of fabrication, manufacturing costs, bed void, pressure loss across the bed, and thermal and mass transport properties.[92] Many potential shapes can be excluded from consideration due to their impracticality or economic inefficiency in fabrication and insufficient structural strength to withstand crushing and attrition. Particles lacking adequate strength are prone to disintegration under intense loading, leading to dust and fragments that can clog the spaces between pellets, particularly for fixed-bed reactors.[93] Therefore, appropriately shaping catalysts to align with the specific reactor type and application is crucial. The following section emphasizes the critical challenges encountered in fixed-bed and fluidized-bed reactors that can be effectively addressed via strategic catalyst engineering.

2.4.1. Catalyst Shaping for Fixed-Bed Reactors

Fixed-bed reactors are predominantly operated under stationary conditions, maintaining consistent operating parameters over long production cycles. Therefore, design efforts are primarily directed toward optimizing these reactors for steady-state operation, ensuring sustained efficiency and effectiveness throughout extended production runs. The pressure loss, heat transfer, and mass transfer must be managed to reach extended reaction runs from the viewpoint of catalyst engineering, minimizing channeling. The shape and size of catalyst particles can significantly affect the pressure loss across a packed-bed reactor.[94,95] Optimizing these parameters can improve the flow of reactants, reducing the pressure loss and enhancing the reactor efficiency.

The most common particle shapes encountered in packed-bed reactors are spheres, rings, (hollow or cylinders), and extrudates with other shapes. Different particle shapes affect the bed structure, resulting in varying pressure loss in packed beds. Due to their symmetrical form, spheres do not affect bed structure through orientation. However, the orientation of nonspherical particles significantly influences permeability and the overall bed structure.[96] Moreover, beds comprising solid cylinders typically exhibit voidage values of around 0.30, compared to approximately 0.40 for beds of spheres.[97,98] Thus, more cylindrical pellets can be accommodated in a given bed volume.

However, to mitigate the increased pressure loss associated with such configurations, the basic shape of solid cylinders is often altered. Modifications may include using hollow cylinders with one or more axially drilled holes, which help to enhance flow characteristics.[92] The following hierarchy is generally observed in evaluating catalyst shapes based

on their influence on the pressure loss in reactors: monoliths < rings < extrudates < powders. Monoliths offer the lowest pressure loss among these shapes due to their structured channels.[93] In the study of packed-bed reactor dynamics, pressure loss behavior was nearly linear, with significant dependency on catalyst packing density, gas flow velocity, and reactor length. Notably, reactors using a structured packing with lower catalyst density demonstrated lower pressure loss than reactors featuring random packing configurations. This finding underscores the importance of the packing structure in optimizing reactor performance.[99,100]

In many industrial catalytic processes, heat transport and thermal catalyst properties often constrain reaction rates. Mitigating internal temperature gradients, commonly called "hot spots," is crucial for optimal reactor performance.[101] Catalysts with high thermal and hydrothermal stability, superior thermal conductivity, minimal thermal expansion, robust thermal shock resistance, and low thermal mass are particularly advantageous. The significance of each thermal property varies depending on the catalyst type and its specific application.[102–104] Properly shaped catalysts, such as those with a high surface area or specific geometrical configurations, can improve heat and mass transfer rates, achieving a more uniform temperature distribution.

The thermal properties of catalysts can be enhanced via surface modification, bulk modification, and material substitution. For instance, coating catalyst particles with a chemical vapor deposition diamond layer of up to 50 μm thick can reduce axial and radial temperature gradients, enhancing reactor efficiency.[105] Additionally, incorporating silicon carbide particles can markedly boost the thermal conductivity and thermal shock resistance of alumina-based catalysts.[106] An analysis of cross-sectional temperature distributions revealed that the structured packed-bed reactor has lower temperature gradients than the randomly packed-bed reactor despite its larger diameter. This observation implies that the effective heat transfer coefficient of the structured packed-bed reactor surpasses that of the randomly packed counterpart, highlighting its superior thermal management capabilities.[99] Catalyst shaping can also reduce the risk of channeling, where reactants preferentially flow through specific paths, leading to uneven distribution and reduced conversion rates.[107,108]

2.4.2. Catalyst Shaping for Fluidized-Bed Reactors

Fluidized-bed reactors are extensively employed in industry for granulation, drying, combustion, and FCC. Their popularity stems from their excellent mixing capabilities, outstanding heat transfer efficiency, and effective gas–solid interaction, collectively improving process performance.[109,110] Despite their advantages, fluidized beds have a significant drawback: the particles in the bed experience substantial mechanical stress due to frequent interparticle collisions against the reactor walls, leading to particle attrition.[111,112] Thus, selecting materials with high mechanical strength and optimizing particle size distribution by shaping catalysts to be more robust and durable can reduce attrition.[113] Moreover, the fluidization behavior is influenced by the particle characteristics, including their size, sphericity, density, and the properties of the fluidizing medium. Proper shaping ensures that particles remain suspended in the gas or liquid medium, promoting better mixing and contact with reactants.[114] Furthermore, tailoring the catalyst shape makes it possible to control reaction pathways, improving selectivity and conversion rates in fluidized reactions.[115]

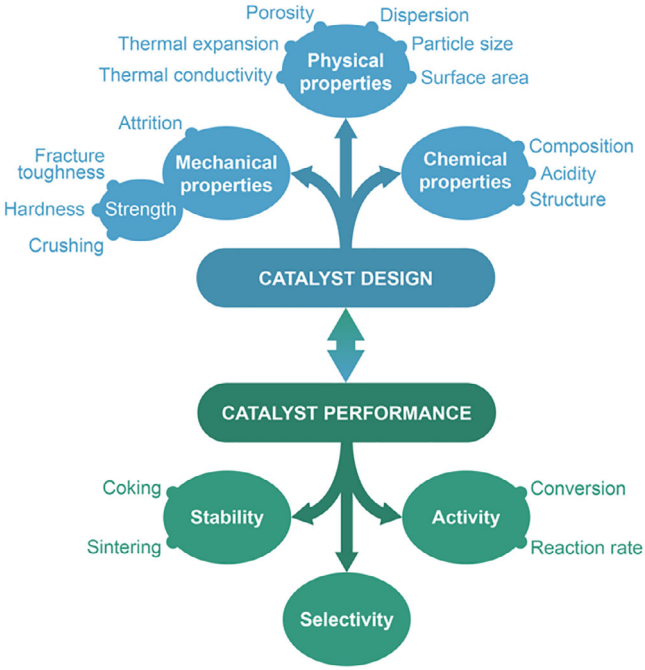

Figure 3. Catalyst design mapping carefully balancing interdependent mechanical, chemical–physical, and catalytic properties.

2.5. Performance Metrics in Catalyst Manufacturing

In 1989, Richardson introduced the concept of the catalyst design triangle, illustrating that designing an effective catalyst involves optimizing its physical, mechanical, chemical, and dynamic properties. Figure 3 presents the concept of catalyst design via a careful balance of interdependent mechanical, chemical–physical, and catalytic properties. This optimization requires selecting component materials, including the active phase, promoter, and support. The active phase and promoter combination are typically selected based on scientific research data. The catalyst design must consider the catalyst geometry (e.g., pellets, extrudates, or spheres) and the distribution of the active phase and promoter in these forms. Engineering considerations (e.g., minimizing the pressure loss via the catalyst bed and maximizing the reactant fluid access to the active catalytic phase) are crucial in determining the catalyst form, shape, and size.[14] The following subsection explores the three interdependent metrics for optimizing the catalyst design.

2.5.1. Mechanical Strength

The testing method for the mechanical strength of solid catalysts has been a subject of interest. Therefore, efforts have been made to establish a standardized approach for measuring this mechanical strength. The crushing strength test emerged as the recognized standard in many countries because it accurately replicates the mechanical stresses that catalysts experience, especially in fixed-bed industrial reactors.[5] The mechanical performance of the catalyst bed is primarily influenced by the pellets or extrudates with the lowest strength rather than by the overall strength of all particles in the bed.[116] Thus, catalyst strength distribution is crucial to mechanical reliability and can be defined statistically by the Weibull modulus. A higher Weibull modulus signifies less variation in crushing strength, indicating that the material is more consistent with uniformly distributed defects throughout the extrudate.[117]

Hardness reflects the resistance of a material to localized plastic deformation, typically assessed through indentation displacement. This process involves pressing a hard, rigid indenter, often made of diamond and with a specific shape, into the material surface. Hardness is calculated by dividing the applied load by the projected area of the displacement indentation, measured after the load is removed.[118]

Fracture toughness indicates the capacity of the material to resist crack growth. This property is usually assessed using large specimens, such as plates or slabs with a predefined crack length. During testing, a tensile load is gradually applied until the specimen fractures. The fracture toughness is calculated by analyzing the crack length and stress that led to the fracture.[119] Apart from the fixed-bed catalyst testing, in fluidized-bed units, the loss of the catalyst due to the generation of fines from attrition is a significant problem. Therefore, resistance to attrition is critical when selecting catalysts for fluidized-bed units. The attrition test is the most commonly applied method for evaluating and ranking fluidized-bed catalysts.[120]

2.5.2. Chemical and Physical Properties

The physical properties of catalysts encompass particle size, density, pore volume, porosity, pore size and distribution, surface area, dispersion, and thermal conductivity. Pore volume and diameter significantly influence the rates at which molecules diffuse into and out of pores, determining the accessibility of reactants to the catalyst surface. Bed porosity and pellet size are crucial for flow dynamics and mass transport properties (e.g., pressure loss). The surface area measures the total support area for dispersing the catalytic phase and contacting the gas phase. In a shaped catalyst, evaluating the textural properties should prominently account for the dilution effect of the binder. This consideration is crucial because binders can significantly alter the porosity and surface area of a catalyst, affecting its overall activity and performance.[89] Catalyst dispersion ensures that the catalytic material is employed efficiently, maximizing the surface area for chemical reactions.[14,121]

Moreover, the catalysts are usually made with conductive metals. The heat transfer performance is primarily linked to the thermal conduction in the solid matrix.[122] Thermal expansion refers to the tendency of a material to change its dimensions, typically expanding when subjected to a temperature change. The extent of thermal expansion in a catalyst body depends on its material composition. Materials have different thermal expansion coefficients, measuring how much the material expands per degree of temperature increase.[123,124]

The chemical properties of catalysts encompass the acidity, composition, oxidation state of the catalytic phase, and structure. Acidity includes Brønsted acidity, referring to the ability of the material to donate protons, and Lewis acidity, the capacity to capture electrons. Catalyst shaping and binders substantially modify the original acidity of the active catalyst, with the effect largely depending on the binder type. For example, alumina alters acidity, which is distinct from silica or clays.[7,125–127] The oxidation state denotes the chemical state or valence of the catalytic phase. The chemical structure involves the geometric arrangement of atoms, the properties of electron configurations, and the bonding characteristics between atoms.[128]

2.5.3. Catalytic Performance

The catalytic performance of catalysts encompasses three essential aspects: activity, selectivity, and stability. Activity refers to the ability of the catalyst to accelerate a chemical reaction. Recognizing activity definitions is essential, such as the conversion of a particular reactant, the reaction rate in moles per mass of catalyst per unit time, and the specific rate per catalytic site, also known as turnover frequency. The reaction rate can also be based on various factors, including the catalyst mass, volume, or surface area, active surface area, and number of available catalytic sites. Selectivity denotes the capacity of the catalyst to direct the reaction toward a desired product while minimizing by-products. Stability indicates how well the catalyst performs under operational conditions.[129] The measurement of the amount of coke formed over the catalyst is an indication of the resistance and stability of the catalyst.

As discussed, technical catalysts are complex composites rather than single-component materials.[130] These composites incorporate elements designed to enhance texture, porosity, robustness, and physical strength, allowing them to withstand high temperatures and abrasion. Their additional components notably influence the behavior of these composite catalysts. For example, binders can either improve or impair catalyst properties, and the performance of a catalyst–binder composite is not simply a linear combination of the individual phase properties.[131–133] This complexity makes scaling catalysts to technical bodies or shapes challenging.

3. Past Developments

Catalyst-shaping technology has evolved significantly over the decades, with the earliest approaches focusing on relatively simple mechanical methods. These early shaping techniques, including pelletizing, granulation, and extrusion, collectively laid the groundwork for more sophisticated catalyst designs and

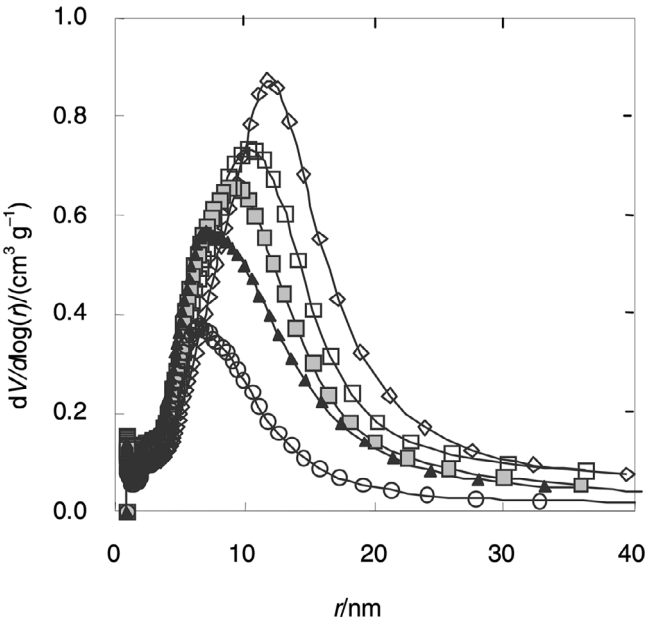

Figure 4. Mesopore distribution from the physical desorption of nitrogen over catalysts pelletized at 0 (◇), 4 (□), 6 (■), 8 (▲), and 10 MPa (°). Reproduced with permission from Ref. [139] Copyright Degruyter, 2009.

engineering. Although their physical principles and implementation differ, each method aims to enhance catalyst usability, strength, and handling during reactor operation.[15,134]

Pelletizing is one of the oldest and most straightforward methods used in catalyst shaping, involving compressing dry catalytic powders into cylindrical or spherical pellets, typically ranging from 1 to 10 mm in diameter. This compression is usually achieved using mechanical or hydraulic presses that apply sufficient force to shape the material. In a typical setup, the catalytic phase or carrier powders are placed into a die and compressed between two opposing punchers, one of which also ejects the formed pellet after compaction.[125–127] The appeal of pelletizing lies in its simplicity and adaptability to a wide range of catalytic compositions. The resulting pellets have good mechanical strength and handling properties, which are particularly suitable for fixed-bed reactors.[135,136] Achieving pellets with optimal characteristics depends on operational parameters, such as the applied pressure, vibration frequency to facilitate powder flow into the die, and the physicochemical properties of the feed powder, including granulometry, chemical composition, hydrophobicity, and particle morphology.[134]

The production of mechanically robust pellets requires that the powder bed be subjected to a nearly uniform triaxial pressure during compaction.[137] However, the high compaction forces often required can cause internal pore collapse, significantly reducing the available surface area and limiting the accessibility of active catalytic sites.[138] This reduction in porosity adversely affects catalytic activity, particularly in reactions where high surface interaction is crucial.

As illustrated in Figure 4, the pore size distribution of a Co−Mn−Al mixed oxide catalyst shifts significantly with increasing pelletization pressure. Specifically, higher compaction pressures lead to a pronounced reduction in the fraction of mesopores, primarily due to the collapse of intraparticle voids.[139] This reduction underscores the trade-off between mechanical strength and textural properties that must be carefully balanced in pelletizing.

A critical factor influencing the feasibility of pelletization is the intrinsic properties of the raw material. Due to their physical characteristics, certain powders derived from diamonds, hard metals, and refractory oxides are often regarded as nonpelletizable.[13] Moreover, the chemical state of the material significantly affects its suitability for pellet formation. For instance, catalyst powders in their oxidized form typically have tensile strengths ranging from 2 to 5 N/mm^2, enabling them to endure the mechanical stresses encountered during pelletization. In contrast, when these powders undergo reduction, their tensile strength can decline dramatically to between 0.5 and 2 N/mm^2, increasing the likelihood of pellet fracture during ejection from the die. Substantial volumes of binders are often introduced to enhance the mechanical integrity of the pellets and mitigate this problem.[137] However, incorporating such additives must be carefully controlled, as excessive quantities can negatively affect the mechanical stability, porosity, and catalytic activity of the final product. Various studies have highlighted the delicate balance required in formulating catalyst pellets, emphasizing the potential detrimental effects of overusing binders on the performance of industrial catalysts.[140–142]

Granulation was developed to address some of the challenges posed by pelletizing, particularly in applications involving fluidized or moving bed reactors. In this method, fine powders are agglomerated into larger, free-flowing granules using mechanical agitation, typically in a granulator or mixer, with the aid of binders and sometimes liquid sprays. These granules are dried and calcined to achieve structural stability.[143,144]

Granulated catalysts offer flowability, dust suppression, and ease of handling. Their spherical or quasi-spherical shapes help maintain uniform fluid dynamics in reactors, minimizing channeling and ensuring better contact between reactants and active sites. The granule size can be tailored based on the reactor design, typically ranging from 0.5 to 3 mm.[145]

However, granulation presents challenges. One primary challenge is the mechanical fragility of the resulting granules, which often suffer from attrition and breakage during handling or under reactor conditions, particularly in fluidized or packed-bed operations.[146,147] An inhomogeneous pore structure and binder distribution in granules can negatively affect the mass transfer and catalytic activity, leading to inconsistent performance.[80] The chemical incompatibility of binders with active phases may also lead to surface coverage or modification of active sites, reducing the overall catalytic efficiency.[14] Another significant problem is the poor flowability of granulated powders, which can result in blockages or feeding inconsistencies in reactors. Furthermore, component segregation during mixing or drying can introduce variability in product quality.[148] The thermal treatment in granule drying or calcination may induce sintering or phase transitions, adversely affecting the surface area and pore accessibility of the granules.[149] Scaling-up limitations are commonly encountered due to differences in equipment geometry, mixing dynamics, and moisture control, often requiring exten-

sive re-optimization during the transition from the laboratory to industrial scales.[150] Addressing these limitations is essential for applying granulation in large-scale catalyst manufacturing and powder processing.

Introduced alongside the traditional methods, extrusion significantly improved the production of continuous catalyst structures. Extrusion involves forcing a moistened paste comprising catalytic powders, binders, and other additives through a die of a specified geometry, producing extrudates that are cut to the desired length, dried, and calcined.[55,151] Early extrusion was appreciated for producing uniform, elongated shapes, such as cylinders or rods, with better dimensional consistency than pelletizing or tableting.[152,153] This method enabled higher production throughput, particularly for applications requiring large volumes of shaped catalysts. Additionally, extrusion was adaptable to creating hollow or multiholed geometries, improving mass transfer and reducing internal diffusion limitations.[82]

However, extrusion faces limitations in its initial form. The process requires careful control over the paste rheology to ensure a smooth flow through the die and to prevent cracking or deformation during drying. Paste formulations are sensitive to moisture content, binder type, and particle-size distribution, influencing the mechanical integrity and catalytic activity of the final extrudate.[15,152] Nonuniform drying and calcination could cause warping, cracking, or shrinkage gradients in the extrudates.[154] Moreover, early extrusion systems lack the automation and feedback mechanisms to adjust process variables in real time, leading to inconsistent quality. Surface skin formation and internal voids due to trapped air further reduce structural homogeneity.[155] Despite these challenges, extrusion became a widely adopted shaping method due to its scalability and ability to produce innovative geometries that were impossible with other techniques at the time.[82]

However, it is important to recognize that catalyst shaping approaches in general exhibit distinct trade-offs in strength, porosity, scalability, and reactor suitability, as summarized in Table 2. Pelletizing produces moderately strong pellets (~1–2 MPa) with acceptable porosity retention (~70%), offering a low-cost and scalable option for industrial applications such as fertilizers and catalysts, particularly in fixed-bed reactors where uniform packing and reduced pressure drop are desirable.[6,80,156] Granulation, including spray or pan methods, yields somewhat weaker particles (~0.5–1.5 MPa) but preserves porosity more effectively (~85%), with medium costs due to binder and equipment requirements. It is scalable to industrial throughput and is widely used for fluidized- and moving-bed systems where uniform spherical granules (0.5–2 mm) enhance fluidization performance.[6,80,156] Extrusion remains the dominant method for technical catalysts, delivering the highest mechanical strength (~2–6 MPa, with trilobes >6 MPa) and engineered hierarchical porosity (~90%) while balancing moderate costs. Its scalability and versatility make it the standard for industrial Ni/Al_2O_3, zeolite, and hydroprocessing catalysts, particularly in fixed-bed reactors where trilobe and cylindrical shapes help minimize pressure drop.[55,80,157] In contrast, spray-drying offers excellent porosity retention (~95%) and full industrial scalability (e.g., FCC catalysts) but produces fragile particles (~0.2–0.5 MPa) prone to attrition. Although costly due to atomization and drying equipment, it remains indispensable for slurry and fluidized-bed processes that benefit from the excellent flowability of spherical microspheres.[13,80]

Furthermore, attrition resistance varies substantially across catalyst shaping methods and is strongly dependent on both material composition and process conditions. As shown in Table 3, pelletized catalysts typically display attrition losses of ≤5%–7% when tested by the ASTM D4058 rotating drum method, with strength improved through higher binder fractions and calcination.[161–163] Extrudates, also evaluated by ASTM D4058, are engineered to achieve <5% attrition loss, where binder optimization, rheology control, and post-calcination rehydration treatments are effective mitigation strategies.[161,164,165] In granulated forms, friability drum tests report acceptable mass losses of ≤1%–2%, with mechanical robustness enhanced through binder addition, density control, and optimized granulator operating conditions.[166–168] Spray-dried catalysts, particularly those used in FCC units, are evaluated by ASTM D5757, where fresh samples often exhibit attrition indices of 3%–10 wt%, and improved formulations with silica–sol binders and hierarchical porosity can significantly reduce fines formation. Collectively, these results highlight how shaping routes not only dictate catalyst attrition resistance but also require tailored mitigation strategies to balance strength with porosity and reactivity.[120,169]

4. Current State-of-the-Art

4.1. Extrusion

The extrusion process is an economical technology for manufacturing catalysts, widely applied in shaping fixed-bed catalysts.[170] The primary benefit of extrusion is the flexibility of the end-product porosity. Altering the porosity of solid catalysts to a range between 30% and 60% is feasible by adjusting the liquid-to-solid ratio in the extrusion paste.[171,172] The extrusion process can be divided into four steps. The first step is mixing and kneading the catalyst powder with binders, water, and other additives, such as plasticizers and peptizing agents, to facilitate the extrusion process. The second step is extrusion to extrudates that can be cut into suitable lengths using a cutting device. The third and fourth steps are drying the extrudate bodies and calcination for the shaped catalysts, respectively.[80,173]

The catalyst extrusion process can be conducted using two extrusion configurations: ram or auger extrusion. The ram extrusion method, called piston extrusion, is a batchwise process. The extrusion paste is loaded into a cylindrical barrel with a pusher piston and die plate on the other end. Shaped bodies exit through the die when the paste is under sufficient pressure. The ram extrusion has the advantages of low shear stress and allowing for paste extrusion with a low solid-to-liquid ratio.

Auger extrusion, commonly called screw extrusion, is a continuous process resulting in a high production rate compared with ram extrusion.[80,170] In screw extrusion, the paste is first poured into a feeding hopper, from which it is directed to a

Table 2. Comparative assessment of catalyst shaping techniques: strength, porosity, scalability, and reactor suitability.

Shaping Technique	Mechanical Strength (MPa)	Porosity Retention	Cost	Scalability	Reactor Compatibility	Ref.
Pelletizing	≈ 1–2 MPa (typical pressed pellets, depending on binder content and pellet size)	~70% (binder reduces BET area, maintains mesoporosity)	Low–simple pressing & binders	Industrial scale (fertilizer & catalyst industries)	Fixed-bed reactors (good packing, reduce ΔP)	[6, 80, 156]
Granulation	≈ 0.5–1.5 MPa (spray-granulated alumina-based catalysts)	~85% (gentle shaping preserves micro/mesopores)	Medium–binder & spray granulation equipment	Pilot/Industrial	Fluidized-bed (uniform granules 0.5–2 mm)	[80, 158–160]
Extrusion	≈ 2–6 MPa (extruded alumina with binders; trilobes can reach >6 MPa)	~90% (hierarchical pores can be engineered)	Medium–requires binder optimization	Industrial (standard for Ni/Al_2O_3, zeolites, reforming catalysts)	Fixed-bed (extrudate geometries reduce ΔP)	[55, 80, 157]
Spray-drying	≈ 0.2–0.5 MPa (spherical microspheres; fragile, prone to attrition)	~95% (excellent retention of micro/mesopores)	High–atomization & drying equipment	Fully industrial (FCC)	Slurry & fluidized-bed	[13, 80]

Table 3. Attrition resistance of catalyst shaping methods.

Shaping Method	Attrition Metric (Test)	Typical Attrition Index	Mitigation Strategies	Ref.
Pelletizing	ASTM D4058 (rotating drum, % loss)	Robust pellets show ≤5%–7% loss on attrition	Higher binder fraction (e.g., colloidal silica, aluminosilicates); calcination.	[161–163]
Extrusion	ASTM D4058 (rotating drum, % loss)	Industrial extrudates engineered for <5% attrition loss	Binder optimization (boehmite, silica sol), post-calcination rehydration, slurry rheology tuning	[161, 164, 165]
Granulation	Friability drum, % mass loss	Acceptable friability ≤1%–2% for coated pellets	Binder addition increases strength; granule density/shape control; optimized drum speed	[166–168]
Spray-drying	ASTM D5757, % mass loss	FCC catalysts: Attrition index (AI)~3%–10%wt (fresh)	Silica–sol binder; hierarchical porosity; calcination.	[120, 169]

single-flighted rotating screw. The screw is rotated using a linkage between the gearbox arrangement and motor. As a result of friction between the paste and the barrel, the paste is forced toward the die assembly, where enough pressure is built to push the paste through the die and produce an extruded catalyst.[174]

Figure 5 summarizes some advantages and challenges of using ram and screw extrusion technology. Screw extrusion presents several significant advantages in catalyst shaping, particularly due to its continuous operation, enhancing process efficiency and consistency.[175] This method is known for producing highly homogeneous products and minimizing dead-zone formation areas in the extruder where material might stagnate, potentially leading to inconsistency in the final product.[176] However, screw extrusion also comes with challenges. Thus, managing the rheological properties of the material is very challenging, potentially affecting the extrusion product quality.[174,177]

In contrast, ram extrusion addresses some of the rheological challenges in screw extrusion, making it more suitable for materials with difficult flow properties.[178] However, this method has limitations. Ram extrusion is more susceptible to dead-zone formation, which can produce less homogeneous products.[176] Additionally, ram extrusion is typically less efficient for continuous production because it often operates in batch mode.[179] Moreover, the post-extrusion drying step is crucial because it significantly contributes to the overall process time and complexity, affecting the final product quality, as illustrated in Figure 5. In addition, the process may suffer from the "dog teeth defect," an irregularity affecting the uniformity of the extruded catalyst.[154] Despite these drawbacks, screw and ram extrusion techniques are versatile and capable of producing a wide variety of catalyst shapes, making them valuable tools in catalyst manufacturing.

A well-designed die and optimized paste rheology properties are needed for extrusion to obtain high-quality extruded catalysts.[180] If the die head quality is high, then finding the right extrusion operation conditions, such as mixing, extrusion temperature, extrusion speed, amount of liquid content, pH (additives), and binder type, is essential to minimize the defect output.[154,181,182] Several variables might directly or indirectly affect the final quality of the shaped catalyst.[183,184] Because of the high potential number of combinations that must be considered during extrusion, this work only highlights the formulation preparation step (i.e., liquid-to-solid ratio and additive effects) and extrusion stage (i.e., extrusion temperature and rate).

4.1.1. Extrusion Optimization

The first step toward catalyst formulation optimization is considering the particle size distribution. A broad distribution with a majority of small-sized particles is essential because the small sizes ensure strong packing between particles. In contrast, larger

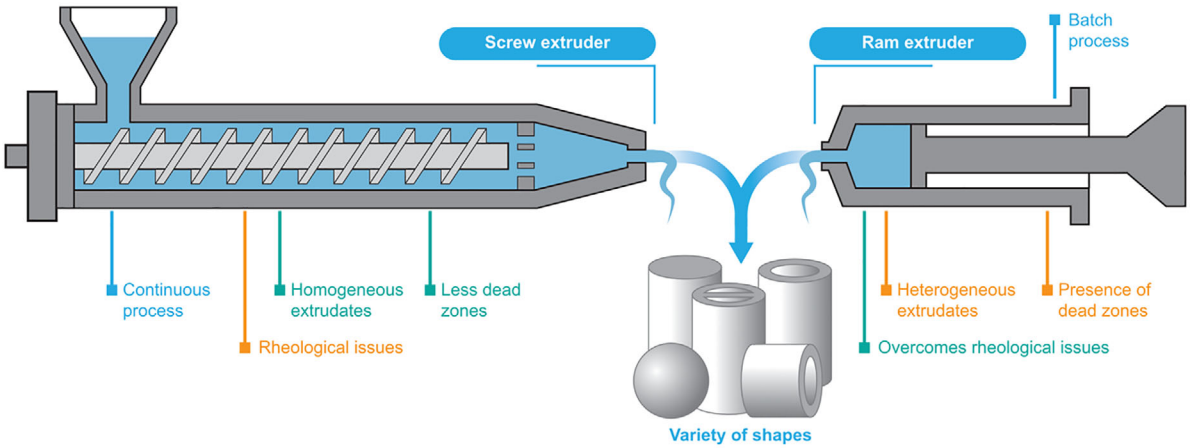

Figure 5. Challenges, advantages, and disadvantages of ram and screw extrusion technology.

sizes facilitate linkage with the applied binder.[154] Combining large particles of 600 μm with particles of 125 μm results in better cohesion than using equal quantities of both sizes.[185] The liquid-to-solid ratio is essential in determining the rheological properties, significantly affecting the extrusion product quality and flow inside the extruder.[180,186] Adding a high quantity of water during mixing and kneading could cause seepage.[154]

In contrast, adding a small volume of water to powder creates high shear stress and sometimes prevents paste extrusion.[186,187] In addition, applying a high liquid-to-solid ratio could result in lamination defects and a decline in the mechanical strength of the shaped catalysts.[185,186] Thus, an optimal value should be applied to ensure a smooth flow and minimum defects. Additives (e.g., plasticizers and lubricants) are commonly used in the extrusion process to ease the paste flow rate and reduce the risk of structural defects during extrusion due to the alteration of the rheological properties.[188] Peptizing agents (e.g., acetic acid) directly influence the paste pH and are essential for achieving homogeneity in the catalyst matrix. Adding acetic acid to the paste formulation is essential for achieving high zeolite dispersion and preventing the formation of large binder clusters. This approach results in better zeolite–binder connectivity and enhances the mechanical strength of the shaped catalyst.[7]

Controlling the extrusion process is essential to maintaining the rheological properties of the slurry during the extrusion. Thus, optimizing the extrusion temperature and production rate is critical to attaining a high-quality extrudate.[180] The increased temperature due to the shear stress between the paste and barrel during extrusion might cause water evaporation, leading to paste drying and die blockage, whereas lowering the temperature facilitates smooth extrusion by maintaining the wet strength and favoring the plastic behavior of the paste. Experiments at different temperatures (19 to 45 °C) demonstrate the optimal extrusion temperature: 19 to 20 °C.[154] Determining the optimal extrusion speed is essential to avoiding many surface defects at high extrusion speeds.[185] However, working at a high speed enhances the mass distribution and produces a uniform paste.

In contrast, working with a low extrusion speed could create voids in the green extrudate body, compromising the structural integrity of the final product. Balancing extrusion speed is critical for maintaining the quality and consistency of the extruded catalyst, as excessively high speeds can lead to surface cracking, whereas those that are too low can cause internal voids and weak points in the material.[14] Therefore, several experiments should be run to control the extrusion speeds better, one of which is recording the extrusion speed vs. the extrusion pressure. The pressure and extrusion speed must have a linear relationship.[154]

4.1.2. Mathematical Modeling

Mathematical models of extrusion processes anticipate the process parameters (e.g., temperature and pressure along the screw length, flow rate, and power on the shaft) to gain a deep understanding of the physical process with accurate simulations for the application.[189,190] In extrusion and many similar processes, the general balance equations, including the momentum, mass, and energy balance equations, are applied with the constitutive equation to address four unknown variables: velocity, pressure, stress, and temperature.[191] Mathematical models can be divided into three subgroups based on mathematical complexity: the 1D flow of Newtonian and non-Newtonian fluids under shear conditions, 2D flow of non-Newtonian fluids, and 3D flow of non-Newtonian fluids.[192] Due to the complexity of mathematical models, most current industrial designs of extruders are based on empirical studies.

The following empirical formula analyzes the generated pressure as a result of the catalyst paste entering a narrow extrusion channel:[177]

$$P = 2\,(\sigma_0 + \alpha_e v)\,\ln\left(\frac{D_0}{D}\right) + 4\left(\frac{L}{D}\right)(\tau_0 + \beta v) \quad (1)$$

where P denotes the generated pressure, σ_0 represents the initial bulk yield stress of the paste, α_e indicates the velocity of the bulk yield stress, v denotes the mean extrudate velocity, D_0 is the barrel diameter, D represents the diameter of the extrusion channel, τ_0 indicates the initial wall shear stress of the paste, and β denotes the velocity factor of the wall shear stress.

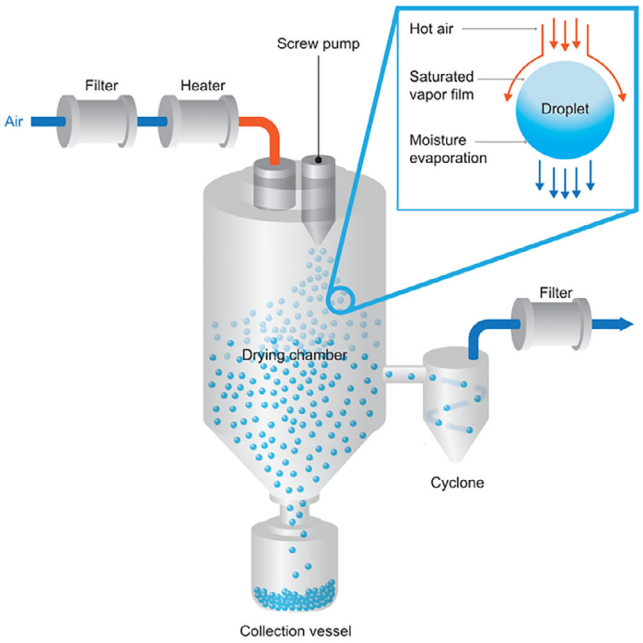

Figure 6. Typical spray-drying setup comprising various components.

4.2. Spray-Drying

Spray-drying has emerged as a critical multiscale tool in catalyst manufacturing, connecting nanostructural control with bulk particle shaping for industrial reactor applications. The method enables the design of spherical catalyst particles with a tailored morphology, porosity, and size, which are critical for ensuring fluidizability and activity in fixed and fluidized-bed reactors.[16,17] During spray-drying, a liquid or slurry is converted into a dry powder by atomizing it into a heated drying medium. The process is well-known as a low-waste generator, making it very attractive for industrial implementation.[23] Therefore, more than 15,000 spray-drying processes have been implemented worldwide.[24]

The spray-drying process has several components influencing performance (Figure 6).[193] Typically, the process starts with a feed solution pumped into the drying chamber via an atomizing nozzle. At the atomizer level, the feed solution encounters pressurized hot gas, usually air, for droplet atomization. Alternatively, rotating disks can break the liquid into fine droplets. Then, the atomized droplets are converted to particles inside the drying chamber due to rapid moisture evaporation, with a residence time typically of a few milliseconds based on the process conditions. Finally, the dried particles are collected using cyclones or filters.[193–195]

In engineering catalysts at the multiscale, spray-drying embodies a bridging technology, enabling the transfer of a nanoscale compositional and textural design (e.g., template-derived porosity) into microscale particle architectures with optimized aerodynamic and mechanical behavior. Such hierarchical structuring is vital to meet the dual demands of activity and stability in actual reactor environments.[196,197] The importance of spray-drying in catalyst production lies in integrating the precursor chemistry, droplet drying dynamics, and the final particle structure in a single, scalable step. The resulting particles serve as direct precursors for calcination, impregnation, or coating steps in synthesizing supported and composite catalysts, representing the industrial standard in refinery and emission control technology (e.g., SCR, TWC, hydrodesulfurization).

In current industrial practices, spray-drying is often applied for manufacturing catalysts in FCC, hydroprocessing, and environmental catalysis, highlighting its versatility and maturity. Spray-drying has gained traction in producing next-generation catalyst systems, such as MOFs, perovskite-based oxygen carriers, and hierarchical porous materials, where morphology and accessibility of active sites must be preserved.[16,198] Thus, the spray-drying process is an excellent example of how historical developments (initially geared toward pharmaceuticals and food) have been co-opted and evolved for advanced catalyst design.

Particle formation in spray-drying includes three primary stages to develop a well-structured and controlled particle shape. The first stage focuses on the effect of the precursor solution on the final particle morphology and porosity. The second development stage concerns the atomization of particle droplets. The third stage involves the drying process, addressing the droplet conversion to particles.[17] The first and third stages have received great attention in particle formation research to produce a controllable structure of porous particles. Moreover, intensive theoretical and empirical descriptive models have been encountered, as discussed in the following sections.[196,199]

4.2.1. Influence of Precursor Properties

Using well-defined porous templates could be considered the most controllable and straightforward approach for catalyst particle production.[200] Therefore, the particle components are adapted to the porous structure of the template. A detailed description of the effect of the droplet precursor preparation is beyond the scope of this literature review (refer to the comprehensive review of the template-assisted spray-drying method by Nandiyanto et al.[17]). However, this paragraph summarizes the primary effective parameters and mentions relevant literature. The mass ratio of particle components to assisted templates is crucial in determining the final porous structure. Thus, the probability of producing dense spherical particles is enhanced when the particle components primarily exist in the precursor solution. In contrast, if the template ratio is significantly higher than that of the particle components, the formation of hole structures is more likely. Therefore, the optimum ratio must be determined to create the desired porosity.[201]

Moreover, the particle, template, and solution charges are vital in designing the particle shape and porosity. A similar charge of particle components and template would result in a repulsive force, creating a porous structure,[202] whereas with an opposite charge, the attraction would result in moth-eye structures.[203] However, several interactions can change the resulting particle structures using a charged solution. For example, for similar charges of component particles and templates and the opposite droplet solution charge, a shell-like film would

develop during the drying process, resulting in a hollow particle structure due to the faster movements of particle components and the trapped template in the center.[204] In contrast, using similarly charged droplets and components would result in irregular shapes due to the tendency of all components to escape.[205] A similar charge of template and droplets and an opposite charge of particle components would result in a more porous particle structure.[206] Figure 7 illustrates this complex behavior of the charge role in the final particle shape.

4.2.2. Influence of Atomization

Atomization is a crucial parameter for controlling the particle size distribution. Nozzle-based (pressure or two-fluid), rotary, or ultrasonic atomizers are typically applied in chemical, food, and pharmaceutical industries.[207] The resulting droplet size depends on the ratio of applied pressure to the feed rate of the solution. Generally, a pressure nozzle generates droplets ranging in size from 10 to 800 µm, whereas smaller droplets ranging from 5 to 300 µm are produced with two-fluid nozzles, making the latter the first choice for laboratory-scale dryers. The rotary or centrifugal atomizers typically generate droplets in the 1 to 600 µm range, and droplets range from 5 to 1000 µm with ultrasonic atomizers.[208,209] These atomizers differ in relevant driving force (pneumatic, electrostatic, etc.). In principle, droplet formation in atomizers is influenced by mechanical, inertial, gravity, or surface tension forces. However, one of the simplest cases is dripping–droplet formation, where the gravity and surface tension forces are in equilibrium, expressed as follows:

$$\rho g \frac{\pi}{6} d^3 = \left(\frac{6 d_0 \sigma}{\rho g}\right)^{\frac{1}{3}} \quad (2)$$

This approach is only applicable to large droplets and very slow velocity conditions. When the nozzle atomizes the liquid solution, the balance between gravity and surface tension cannot be maintained; thus, the dripping state becomes a jetting state.[209] The critical Weber number can describe this transition. Accordingly, Clanet and Lasheras[210] obtained a critical value for the Weber number by extending Taylor's model:

$$We_c = 4 \frac{Bo_0}{Bo} \left(1 + KBoBo_0 - ((1 + KBoBo_0)^2 - 1)^{\frac{1}{2}}\right) \quad (3)$$

where Bo and Bo_0 are bond numbers based on the inside and outside diameters of the nozzle at the orifice, respectively, and K is a constant.

A more general empirical formula for the droplet size determination was developed based on the atomizer type, liquid viscosity, surface tension, and other physical properties, as expressed below:[211]

$$D_d = K_f Q^n \left(\rho^a \sigma^b \mu^c\right) \quad (4)$$

where K_f, Q, and n represent equipment properties, and a, b, and c are related to the droplet solution.

Moreover, the gas type, pressurized gas-flow rate, and liquid feed-flow rate influence the droplet formation and size distribution.[194,212] Various gases (e.g., air, CO_2, and N_2) can be applied for droplet atomization. Often, low-density gases are employed to obtain smaller droplet sizes. Considering the flow rate of the pressurized gas and the flow rate of the feed liquid, high flow rates of pressurized gas generally result in smaller droplet sizes, whereas high flow rates of liquid feed yield larger droplet sizes.[212]

4.2.3. Influence of Other Process Conditions

Besides the composition of the precursor solution and the atomization step, the process parameters during droplet-to-particle conversion affect the final morphology and particle size during spray-drying. The standard approach for understanding the drying mechanism and evaluating the influence of process parameters on product properties is based on conducting several experiments with a laboratory-scale dryer.[213] Specific process parameters (e.g., drying gas temperature, gas flow rate, feed flow rate, and relative humidity [RH]) are varied, and the final particle structure is characterized using Raman spectroscopy, scanning electron microscopy, or X–ray diffraction. However, this approach lacks in situ tracking of the drying process, which requires sophisticated instruments to capture the dynamic behavior of a thousand droplets during drying. Hence, Pearce et al.[214] proposed novel techniques to track the droplet dynamics at various positions in the drying chamber using liquid N. Another approach for understanding the drying mechanism is conducting in situ single droplet experiments.[215] Although the single droplet does not experience the same environment and conditions as in the spray-drying process due to missing droplet–droplet and droplet–wall interactions, the approach is still advantageous in predicting the particle morphology during certain drying conditions.[215,216]

When focusing on the actual process parameters during spray-drying, the temperature is considered a primary parameter that affects droplet-to-particle formation because it is directly connected to the heat and mass transfer phenomena.[194] Thus, the gas inlet temperature strongly affects the final particle size and morphology.[217] Generally, the gas inlet temperature is directly proportional to the droplet evaporation rate. Accordingly, increasing the inlet temperature increases the evaporation rate, resulting in a faster crust formation at the outer surface of the droplets. The slow diffusion of the solutes to the center compared to the fast evaporation rate causes a hollow or irregular shape due to the trapped liquid solvent.[218] Moreover, when the inlet temperature is higher than the boiling point of the solvent, a volume expansion phenomenon for the droplet is significantly expected due to the fast crust formation and trapped liquid, increasing the particle diameter.[219] In contrast, lowering the gas inlet temperature reduces the evaporation rate, delaying crust formation and causing a dense core and spherical small particles. In addition, Lin et al.[219] concluded that low drying temperatures result in dense, small, and regular-shaped particles in the investigated material system.

In addition to the inlet gas temperature, RH plays a critical role in drying. The gas temperature is directly proportional to the evaporation rate; however, the RH is inversely proportional to the

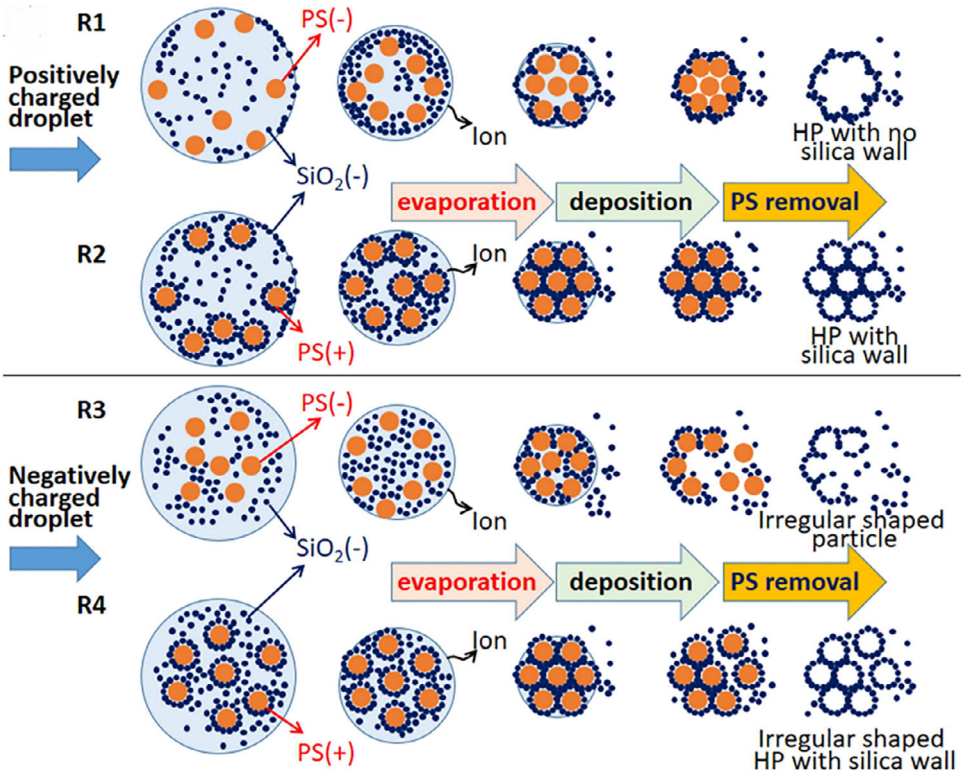

Figure 7. Schematic of particle formation depending on the charge of the host components, templates, and droplets. Reproduced with permission from Ref. [17] Copyright Elsevier, 2019.

evaporation rate and is a critical point for an effective drying process at a given gas temperature. At 100% RH, drying would not occur; however, increasing the RH to an extent results in a lower evaporation rate, resulting in homogenous and dense solid particles, given enough time for solute diffusion.[220] Griesing et al.[221] studied the influence of varying RH on the final particle diameter and porosity for mannitol-water droplets and found that increasing the RH decreases the evaporation rate, producing smaller particle diameters and lower porosity. Another important parameter to consider during the drying process is the feed-flow rate to the drying chamber. Smaller droplets are formed when the atomizer rotation speed or spray air pressure is higher, producing smaller particle sizes.[222]

4.2.4. Mathematical Modeling

Kemp and Oakley classified the modeling of the spray-drying process into four levels, which were later extended to five levels.[223] On the first level, only the heat and mass transfer are considered. This approach is unsuitable for representing the spray-drying performance and tracking particle behavior. The second level is the "scoping level," which includes a rough estimation of the drying equipment size using a simple theoretical model for drying kinetics. The third level is the "integral" or "scaling-up" model that uses pilot plant experiments of the drying curve for upscaling. The fourth level is called the "incremental" or "one-dimensional" model, which has a set of simultaneous equations to be solved in incremental steps along the drying axis. The fifth level is called the "detailed model," which is solved using computational fluid dynamics (CFD).

The 3D flow patterns of gas and particles can be tracked using CFD, and the heat and mass transfer of evaporation and solidification is considered in individual droplets.[224] The Eulerian–Lagrangian approach is typically applied for spray-drying studies, where the gas phase and droplets or particles are treated as interpenetrating continua. The gas phase is described by Navier–Stokes equations, accounting for the drag force exerted by the particles, and solved using the Eulerian grid. The particles or droplets are considered a discrete phase described by Newton's Second law of Motion, solved using the Lagrangian approach.[225,226]

These models can also be extended to account for droplet–droplet and droplet–wall interactions by implementing a probabilistic approach.[225] The evolution of modeling approaches for spray-drying, from empirical correlations to high-fidelity CFD with discrete element method (DEM) simulations, reflects the broader trajectory in multiscale catalyst engineering. By capturing droplet behavior, mass transfer, and aggregation at multiple scales, these models contribute to predictive design, accelerating scaling-up and enhancing the reproducibility of the catalytic function. Integrating particle-level drying models with macroscopic dryer simulations exemplifies how multiscale modeling can derisk development and support continuous processing strategies in catalyst shaping (see reviews by Dosta et al.[227] and Mezhericher et al.[228] for more on multiscale modeling).

Moreover, two approaches for modeling drying kinetics exist: the distributed-parameter and lumped-parameter

approaches.[229,230] In the distributed-parameter approach, the drying droplet is identified at various drying periods with varied evaporation rates in response to the crust-formation level of the particle.[230] Ranz and Marshall published the first theoretical modeling of the drying droplet.[231] Later, several studies on distributed-parameter modeling were published. Mezhericher et al.[197,232] published a comprehensive review and developed a model.

In contrast, the lumped-parameter approach considers the physical properties and components of the drying materials, which are uniform throughout the particle, using the concept of the characteristic drying rate curve (CDRC) and the reaction engineering approach (REA).[229,233] The CDRC is a dimensionless representation of the drying behavior of a material, plotting the normalized drying rate against the normalized moisture content to predict the drying kinetics under varying conditions.[234] The drying rate of a moist solid or droplet can be expressed as follows:[235,236]

$$\frac{dm}{dt} = -h_m A \left(\rho_{v,s} - \rho_{v,b}\right) \quad (5)$$

where m is the mass of the droplet-particle, t denotes the time, h_m represents the convective mass transfer coefficient, A indicates the surface area of the droplet particle, $\rho_{v,s}$ denotes the vapor concentration at the particle–gas interface, and $\rho_{v,b}$ represents the bulk vapor concentration.

Chen and Xie[237] initially developed the REA, which Chen and Lin later amended.[235] The REA is based on the reaction engineering concept that considers the drying process to be a competitive, reversible process between evaporation and condensation reactions, where evaporation is an activation process that must overcome the barrier energy of water evaporation while assuming condensation is a nonactivation process. The REA relates the apparent activation energy to the moisture content, a measurable characteristic property of the drying droplets. Therefore, the vapor concentration at the gas–liquid interface can be evaluated as a function of the moisture content.[237]

Chen and Lin[235] validated REA and the CDRC with experimental data for milk droplet drying. They found that the REA produces the experimental data more precisely than the CDRC model. In later work, Lin and Chen[238] predicted milk droplet drying under high humidity by applying the REA. Moreover, the REA was successfully used to predict the drying patterns of cream, lactose, and whey proteins, with high agreement with the experimental results.[236,239]

Patel and Chen[229,240,241] applied the REA to detail the spray-drying process for industrially applied material systems (e.g., whey protein concentrate, skim milk, and lactose). They found that the REA is very accurate and sensitive to changes in operating parameters and is very useful in predicting product property variations due to operating condition alterations.

In summary, spray-drying exemplifies a multiscale engineering tool, enabling the bottom-up translation of a material design into structured catalyst forms. This role is expected to expand as digitalization and process simulation converge toward closed-loop control, enabling the dynamic tailoring of product properties to meet application-specific catalytic demands.

4.3. Fluidized-Bed Spray Granulation

Fluidized beds are widely applied in the chemical, pharmaceutical, and food industries due to their enhanced heat, mass, and momentum transfer and scalability. The fluidizing gas is introduced at the bottom of the apparatus via a gas distributor plate, fluidizing the particles. At low gas velocities, the bed remains in a fixed-bed mode. The transition from a fixed to a fluidized-bed state increases as the air velocity increases. This velocity is called the minimum fluidization velocity of the investigated material. At this point, particles are suspended and mixed well by the upward gas flow, allowing effective processing.[242] Typically, the cross-sectional area of the fluidized bed increases with increasing height, decreasing the gas velocity in the expansion zone, causing particles to move back into the process chamber.

Fluidized-bed spray granulation describes the injection of a liquid onto the bed of fluidized particles, resulting in a size enlargement when the liquid solvent evaporates, forming a solid film or bridge. The process generally starts by feeding the particles into the bed. Then, the particles are fluidized using a flow of hot gas from the bottom, and the liquid binder is atomized into droplets and sprayed onto the bed of particles, forming larger particles due to the resulting particle–droplet and particle–particle interactions.[243]

"Granulation" is often an umbrella term for agglomeration, granulation, or coating. The primary goal of these processes is to alter the physical properties of powders to meet specific product criteria, including size, shape, flowability, density, solubility, and porosity.[244,245] These are cornerstone processes in the physical engineering of catalysts, where multiscale control from droplet wetting to granule formation to reactor integration is vital. This process is relevant for manufacturing catalysts with controlled particle-size distributions and structural homogeneity because these properties directly influence transport phenomena, mechanical stability, and catalytic performance. If agglomeration, granulation, or coating occurs, it depends on the particular process conditions and materials.[245,246] The injected droplets connect individual particles via liquid bridges during spray agglomeration. Due to the (typically heated) gas stream, the liquid bridges solidify, resulting in blackberry-shaped particles. The agglomeration process is commonly used for food and catalyst production because the resulting product typically has a high porosity and specific surface area.[27]

In contrast, the liquid forms a layer around single particles during granulation. As the solvent evaporates, the layer solidifies, resulting in an onion-like growth of particles. Spray granulation is widely employed in the food and pharmaceutical industries and in detergent and fertilizer production.[247] Coating is similar to granulation, where the layer heights are typically smaller. The process is commonly applied in the pharmaceutical industry to control drug release and increase tablet stability and mechanical resistance.[248,249] Figure 8 presents a schematic of the potential growth pathway of catalyst particles in a fluidized bed with a bottom-spray configuration.[250] Initially, a primary dust forms due to the overspray from spray-dried droplets.[251] These fine particles agglomerate with spray droplets to form seed particles. In the initial stages, growth is primarily driven by agglomeration.

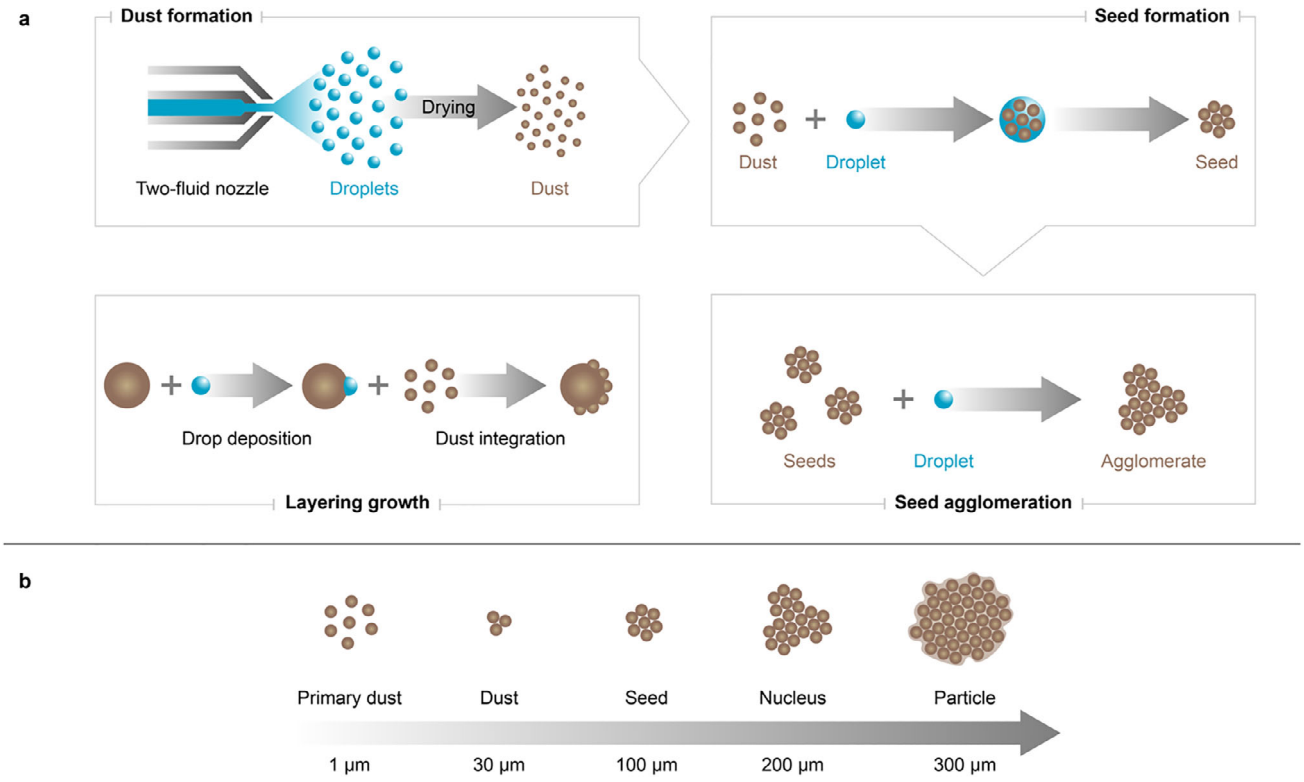

Figure 8. a) Stages of particle formation and growth. b) Particle classification and approximated size ranges. Reproduced with permission from Ref. [250] Copyright Elsevier, 2019.

However, as the particles enlarge, their increased surface area facilitates the capture and deposition of dust, fostering surface layering rather than further agglomeration.[252,253] Understanding the interplay between dust integration via surface layering and seed formation via agglomeration is critical because both processes compete for the same dust supply.

The fluidized-bed spray granulation application spans diverse industries and catalyst types, including automotive emission control catalysts, enzyme carriers, and supported metal oxides. The process facilitates shaping and integrating catalytic or functional layers onto inert cores, forming composite particles employed in structured reactors or monoliths. This process can be operated in two modes: batch or continuous. The batch mode has attained much research attention during the last few decades and is frequently applied in industry, especially in the pharmaceutical industry. However, for many economic reasons, the continuous operation mode is more attractive for industrial applications due to its higher throughput, lower downtime, and lower labor cost than batch processes.[21] However, the particle residence time distribution is a well-known challenge of the continuous mode. For most applications (e.g., drying and granulation), the residence time distribution should be as narrow as possible to achieve a constant and homogeneous product quality, which is often difficult.[254–257]

The particle growth in a fluidized bed depends on parameters that determine the final particle-size distribution and morphology. Several recent studies have explored the parameters and their effect on particle growth.[230–234] These studies have classified these parameters into three categories: the reactor geometry, such as the shape of the granulator and nozzle position; the process parameters, including the airflow rate, temperature, and atomization; and the material parameters, such as the type and concentration of the binder. The categories are detailed in the following sections.

4.3.1. Reactor Geometry

The geometry of a fluidized-bed reactor is crucial because it directly affects fluidization dynamics, particle coating or granulation efficiency, and overall reactor performance.[258] The critical geometric elements include the fluidization chamber shape (e.g., cylindrical and conical), the design of the distributor plate, and the design and position of the nozzles or internals.[259] The design of the distributor plate affects the gas flow pattern and fluidization quality.[260,261] Baffles or other internal structures can enhance mixing, control flow patterns, or prevent dead-zone formation.[245] Studies have observed that the nozzle position significantly affects the final particle size.[254,262] Depending on the nozzle position, three configurations of the spray process can be differentiated: top-spray, bottom-spray, and tangential-spray fluidized beds. Each configuration has advantages, disadvantages, and challenges.

Top-spray configuration: The top-spray position of a nozzle in a fluidized bed is well-known for its simplicity and efficiency, derived from commercial fluidized-bed dryers. This configuration offers high capacity and low capital costs.[263] The spray nozzle is positioned at the top of the chamber, allowing a liquid injection

countercurrent to the fluidization gas. Typically, the spray nozzle is either binary (two-fluid) or pneumatic. The operation mode is applied on a broad scale range, from 2 L laboratory-scale setups to industrial units exceeding 2,000 L.[264–266]

Figure 9a presents a schematic view of the top-spray configuration in the batch mode. Particles are randomly exposed to the sprayed liquid and pass through the wetting zone. The random circulation of particles means that the droplet travel distance is uncontrolled, risking early drying, similar to spray-drying. In contrast, a long mean free path allows droplets to spread and wet multiple particles before coalescence, promoting agglomeration, making the top-spray configuration less suitable for film and controlled-release coatings.[263,267]

The spraying area depends on the nozzle position above the bed and its spray angle. Studies on top-spray granulation reported that the nozzle at a low position results in larger particle sizes than those at a higher position at the same binder flow rate. This result is attributed to the increased ability of the binder to wet and diffuse into the particle due to the shorter distance. Nozzle positions that are too high must be avoided because this increases the risk of clogging and wetting the granulator walls.[268] Therefore, crucial challenges include optimizing the spray parameters to control agglomeration and temperatures, as well as overcoming unknown travel distances of droplets to particles, which could affect product quality. However, the top-spray configuration is suitable for taste masking and barrier, cosmetic, and functional coatings, where precision is less critical.[263]

Bottom-spray configuration: In the bottom-spray-fluidized bed configuration, the spray nozzle is at the bottom, directing the spray upward through the bed of fluidized particles. The mean free path length of the droplets is shorter than in the top-spray configuration, as the droplets quickly interact with high-velocity particles in a confined spray zone. This interaction permits a more precise coating, rather than an uncontrolled agglomeration, making it ideal for encapsulation and layering. The bottom-spray-fluidized bed can also be performed with an additional tube in the center, the Wurster tube, separating the wetting and drying zones.

Wurster first invented this system in the middle of the twentieth century.[269] The Wurster system has been widely employed in many industrial applications[270] (Figure 9b). Due to the separation effect, the system is highly effective for coating particles as small as 100 µm, allowing better spray penetration and a more uniform coating. Unlike the conventional top-spray technique, which recycles particles through the coating zone in seconds, the Wurster system offers a more controlled fluidization pattern. The concurrent path of the droplet toward the particles is short, eliminating early droplet evaporation and allowing the film-forming droplets to spread, creating a dense film with exceptional physical quality,[270–273] making it the preferred system for coating.[21] The challenges include nozzle clog prevention (especially with high-viscosity binder solutions) and precise control of spray parameters and fluidization conditions to ensure optimal performance.

Tangential-spray configuration: The tangential-spray fluidized-bed configuration involves spraying the binder solution tangentially into the fluidized or rotary fluidized-bed. In a rotary fluidized bed, the particles are suspended and mixed by the upward gas flow and rotational motion of the bottom plate (rotating disk), enhancing the heat and mass transfer efficiency. The improved mixing results in a more uniform coating and granulation.[266,267] Three distinct forces drive particle circulation in the tangential system. First, the rotating disk or tangential spray of the solution generates a centrifugal force, pushing the particles toward the wall. Second, the air passing through the disk creates a lifting force, accelerating the particles upward in the chamber. Third, gravity pulls the particles downward toward the disk. The interplay of these forces results in a homogeneous spiral motion of the particles.[274,275] Figure 9c demonstrates the tangential spray in a fluidized bed in the batch mode. The challenges of tangential-spray fluidized beds include uniform spray coverage to avoid dead zones and complex operation optimization to achieve quality products.

4.3.2. Influence of Process Parameters

Several parameters influence particle-size enlargement during agglomeration or coating in the fluidized-bed spray-drying process. These parameters are often interrelated, but each has a certain extent of influence on particles when other parameters are fixed. The following paragraphs address the four primary process parameters: the spray rate, fluidizing air-flow rate, temperature, and particle feed rate.

Spray-rate effect: In general, two approaches exist to investigate the effect of the spray rate. The first method is to vary the spray rate by altering the atomizing air at a constant binder-solution content. The second method alters the spray rate by changing the binder solution flow rate while maintaining a constant atomizing airflow.[254,255] The first approach identifies a linear relationship between the particle diameter and increased spray rate, corresponding to the layering growth mechanism.[255] Similarly, increasing the atomizing airflow results in consistent homogeneous layering growth. Increasing the binder solution flow rate while maintaining a constant atomizing airflow produces particle agglomeration and larger particle sizes, which could cause earlier defluidization.[254] Increasing the binder solution flow rate in the spray-fluidized bed of primary glass particles results in larger agglomerates and increased porosity.[276]

Particle Feed-rate effect: Increasing the particle feed rate generally increases bed mass. Accordingly, this increase reduces the particle wetting rate for a constant spray rate and reduces the probability of wet particles colliding. An increased particle feed rate leads to a decreased porosity and agglomerate size.[276] Furthermore, a further decrease in particle feed rate can result in earlier defluidization.[245]

Air inlet temperature effect: The particle-size enlargement behavior depends on the equilibrium between the drying and

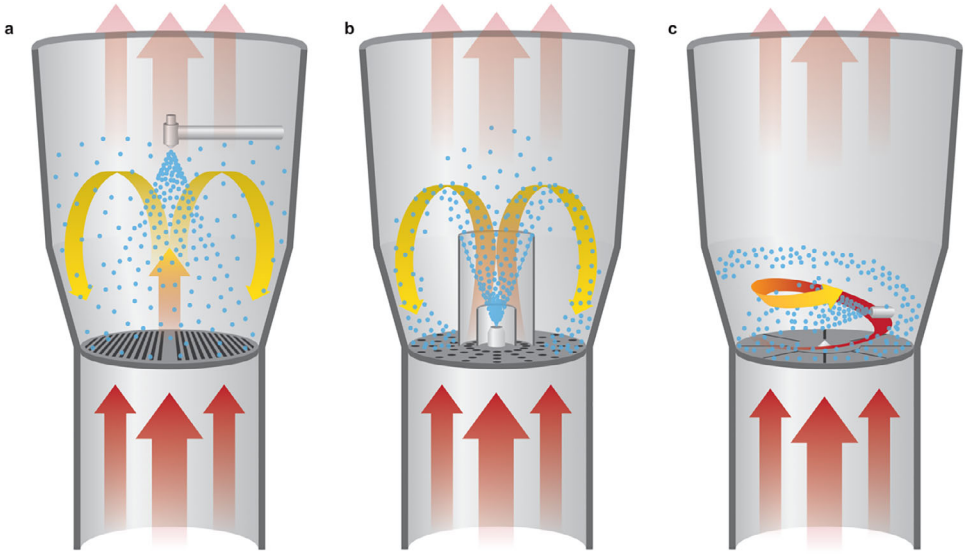

Figure 9. Schematic of fluidized-bed spray granulation in the batch mode: a) top-spray configuration, b) bottom-spray configuration, and c) tangential-spray configuration. Adapted from the Glatt website.[274]

wetting rates. If the drying rate is faster than the wetting rate due to a high air inlet temperature, the particle layering is expected to increase. Conversely, if the air inlet temperature is low, a sizable agglomerate formation is likely, which might cause earlier defluidization.[277] Studies on the effect of varying the inlet air temperature on cornstarch coated with nano-silica found that the temperature has little influence on the granule size enlargement compared to changing the spray flow rate.[255] Additionally, increasing the air inlet temperature decreases the agglomeration size and slightly reduces porosity.[276]

Airflow rate effect: The airflow rate has an inverse relationship with the agglomerate size and fluidization time. A higher airflow rate induces a high relative collision velocity, increasing the probability of particle breakup rather than coalescence. A high airflow rate also causes more attrition, resulting in smaller particle sizes.[277,278] Studies on the effect of varying the fluidized airflow on the granule growth of rice powder found that higher airflow rates result in smaller granules.[279] Similarly, increased air velocity reduces agglomerate size due to significant breakage forces.[276]

4.3.3. Influence of Material Parameters

Effect of the binder solution nature: The nature of the binder solution significantly influences droplet deposition over the particle surface. Droplets with high viscosity splash less upon colliding with the particle surface.[280] Therefore, the probability of a successful coalescence for the collided particles is higher. Although other physicochemical properties might affect the growth mechanism, viscosity is the most effective.[257]

Effect of the binder solution concentration: The binder concentration has less influence on the granule size growth than the nature of the binder solution.[281] Increasing the binder concentration could lead to smaller agglomeration sizes, which is attributed to the lower water content in the concentrated solution.[255] Conversely, other observations have indicated that an increased binder concentration could result in larger agglomerates.[254] These differing results can be attributed to the viscosity of the binder solution, which varies with changes in the concentration.[281]

4.3.4. Controlling Active Phase Dispersion

Incorporating active metal components onto catalyst supports has conventionally been achieved via impregnation techniques, typically employing aqueous solutions of metal precursors.[282] The porous support is brought into contact with the precursor solution during the impregnation process. The method can be broadly categorized as i) capillary impregnation, where the support is initially dry, and ii) diffusional impregnation, where the support is presaturated with the solvent phase.[283,284]

In both cases, air trapped in the pore network of the support may impede efficient solution penetration. The entrapped gas is compressed as the liquid penetrates the porous matrix under capillary forces. Liquid flow halts when the internal gas pressure balances the capillary pressure. The pore volume is often pre-evacuated to eliminate trapped air and facilitate complete impregnation.[285]

Following impregnation, a drying step is typically undertaken at temperatures ranging from 50 to 250 °C to remove the solvent.[286] During drying, solvent transport occurs through the capillary-driven flow and diffusion mechanisms. Concurrently, the metal precursor distribution may be altered via adsorption and desorption phenomena, influencing the final spatial distribution of the active phase in the support.[285,286]

Many studies have focused on controlling the metal distribution profile in catalyst particles. Four principal distribution types are commonly reported: uniform, egg-yolk, egg-white, and egg-

shell configurations (Figure 10a).[285,287,288] The optimal distribution is linked to the targeted catalytic performance parameters: activity, selectivity, stability, and intrinsic reaction characteristics, including kinetics and mass transfer limitations. For instance, in a theoretical study, Becker and Wei[289] demonstrated that an egg-yolk-type distribution is favorable under kinetic control (i.e., a low Thiele modulus). In contrast, the egg-white and egg-shell profiles are advantageous under diffusion-limited conditions (i.e., a high Thiele modulus). Zimmermann et al.[290,291] demonstrated that core–shell (egg-white type) catalyst pellets can significantly enhance reaction heat management. Catalyst pellets coated with the thickest inert shell exhibited up to 30% higher methane selectivity compared to uncoated pellets under conditions with external mass transport limitations. This improvement is attributed to the differential diffusion rates of reactants and products through the inert shell, which alters the internal equilibrium composition within the catalyst. Notably, the inert shell promotes selectivity toward the desired product, particularly when the preferred product has a higher diffusion coefficient in the shell, making its formation more favorable.

A dry impregnation technique has also been explored in a fluidized bed, depositing precursor solutions onto porous particles without excess liquid. Although relatively less studied, this approach has promising results. For example, metal precursors have been successfully deposited onto porous supports via spray impregnation in a hot fluidized bed, with nearly complete deposition efficiency.[292–295] The extent of metal loading is primarily governed by process parameters, such as the spraying time, solution concentration, and flow rate.

A critical determinant of the final metal distribution is the dynamic interplay between the drying rate (influenced by operating conditions) and the capillary penetration rate (depending on the physicochemical properties of the system). Under slow drying conditions, the active phase is uniformly deposited throughout the particle. Conversely, rapid drying produces precursor accumulation near the external surface, yielding an egg-shell-type structure.[296]

The microscopic analysis corroborates these findings. For instance, in the impregnation of fine porous silica particles (average diameter of 120 µm) with an iron nitrate solution, slow drying generates a homogeneous internal distribution of the metal species (Figure 10b.1). In contrast, fast drying causes the precursor to concentrate at the particle surface (Figure 10b.2).[297]

A recent work[91] systematically investigated catalyst shaping using a top-spray fluidized-bed granulation process and examined its influence on the catalyst properties at multiple scales. This work analyzed particle growth mechanisms, the spatial dispersion of zeolite in the formed catalyst bodies, and the effect on active site accessibility and catalytic performance in the methanol to hydrocarbons reaction. Fine-tuning the shaping parameters achieved optimized zeolite dispersion in the catalyst matrix, significantly improving zeolite utilization from about 70% under nonoptimized conditions to nearly 100% under optimized shaping protocols.

A novel dual-staining protocol was employed in conjunction with confocal laser scanning microscopy to gain insight into the internal architecture of the shaped catalyst particles. As illustrated in Figures 10c, and 3d reconstructions of two representative catalyst samples (μ_2 and A_2) indicate the distribution of the Brønsted acid sites associated with the zeolite domains (in blue) in the macroporous matrix (in pink). The μ_2 sample, which underwent seed formation during growth, displayed a poor zeolite dispersion with large aggregates (Figure 10c.1). In contrast, the A_2 sample, characterized by dust-mediated growth (Figure 10c.2), demonstrated a high degree of zeolite dispersion with considerably smaller aggregates. These findings underscore the critical relationship between catalyst particle formation mechanisms and internal structure, highlighting the importance of growth control strategies in tailoring the catalyst architecture for improved performance.

4.3.5. Mathematical Modeling

The complexity of the fluidized-bed spray granulation process is evident from the multiple physical processes that co-occur and interact with each other, such as droplet deposition, evaporation, particle interaction, agglomeration, and breakage, resulting in various scenarios occurring during particulate processing in the fluidized-bed spray-drying process.[254] When droplet size is small relative to the particle size, two mechanisms may occur: layering growth due to the rapid drying of droplets or agglomeration growth from wet particles colliding. However, breakup and layering growth can also occur if cohesive forces are weak. In the second scenario, agglomeration is more likely when the droplet size is larger unless the breakup force exceeds the cohesive force, leading to small agglomerates and layering growth. Three mechanisms for agglomerate fracture have been proposed: attrition, binary breakage, and fragmentation.[278]

A fluidized-bed spray granulation model must account for all submicro processes. Various models for these complex phenomena have been proposed in recent years.[246,298–301] Thus, multiscale simulation frameworks are needed, which integrate micro-level phenomena (e.g., droplet impact and drying, binder spreading) with macro-level reactor hydrodynamics. Previous research has primarily focused on two approaches. The first approach employs the population balance equation (PBE) to track the particle size distribution change during the process.[246,301] The second approach involves the combined CFD discrete element method (DEM) model, which considers the interactions between the three phases: gas, solid, and liquid.[302] The CFD–DEM model also uses the PBE to track changes in particle size.[298,299]

The effective use of the PBE relies on the ability to solve the equation numerically because analytical solutions are rare.[303] Therefore, the PBE is commonly solved numerically using the Monte Carlo (MC) approach.[304,305] The MC method is effective because it can consider all submicroprocesses, such as droplet deposition, wet–wet particle collision, and droplet drying, which are crucial in the size enlargement process. A volume constant MC algorithm was introduced to overcome the complications of solving multivariate PBEs and predict the general shape of the agglomerate size distribution.[301] This model was later modified to account for porosity changes with changes in agglomerate size and process conditions.[246,306]

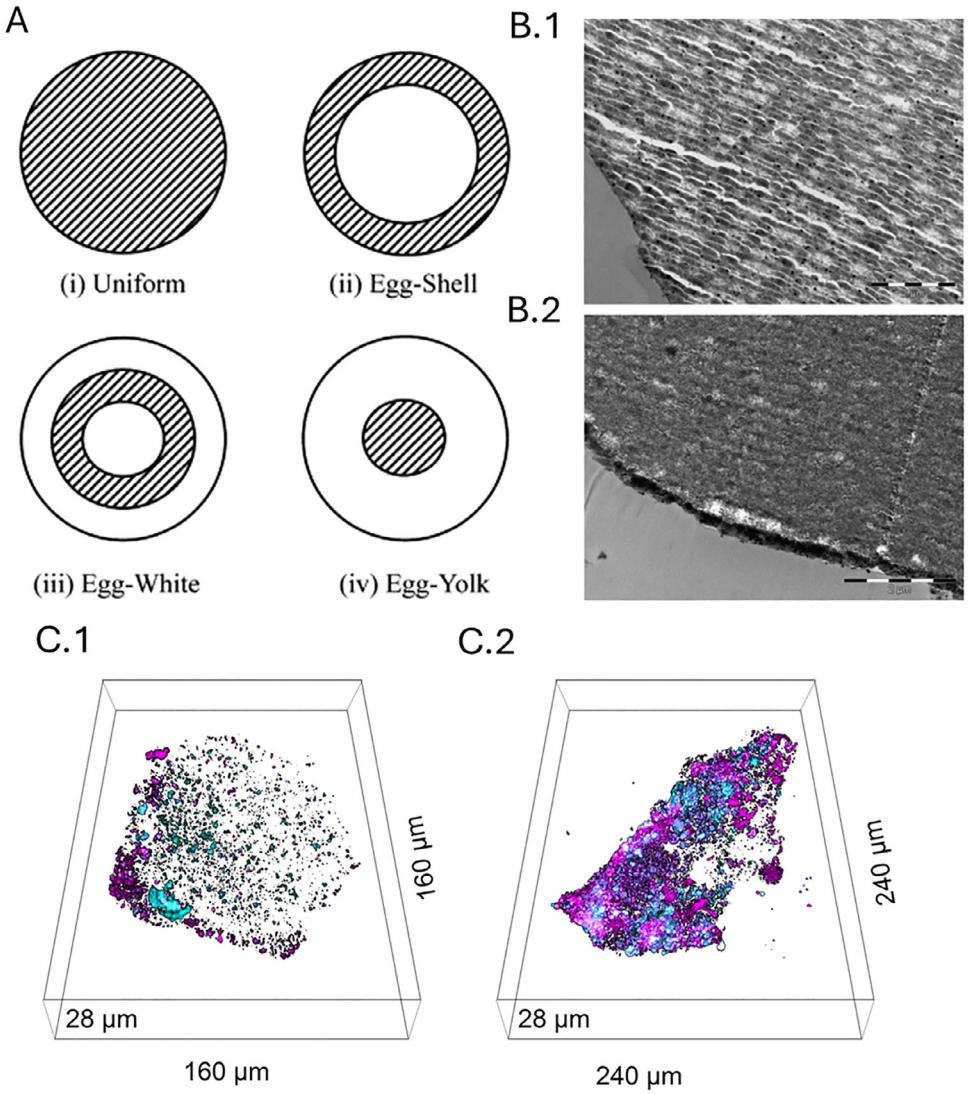

Figure 10. Metal distribution profile of catalyst particles: (A) uniform, egg-yolk, egg-white, and egg-shell configurations. Reproduced with permission from Ref. [285] Copyright ACS, 2001. Impregnation of fine porous silica particles with an iron nitrate solution, slow drying (B.1) and fast drying (B.2), adopted from Barthe et al.[297] 3D reconstructions of two representative catalyst samples (μ_2 and A_2), c.1 and c.2, respectively, via confocal laser scanning microscopy. Reproduced with permission from Ref. [91] Copyright Elsevier, 2025.

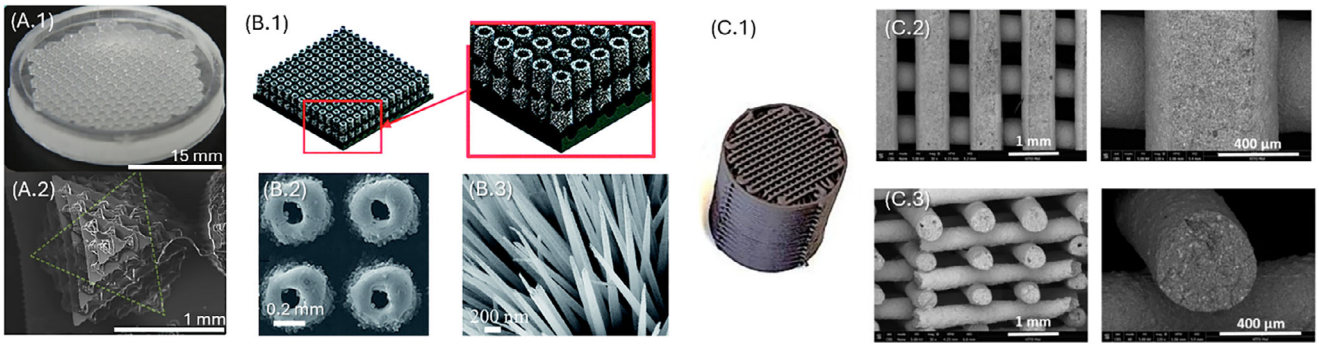

Figure 11. Macroscale vs. microscale images of structures obtained via 3D-printing: A) Fractal relief on a photocatalyst printed using vat photopolymerization with liquid crystal display, with features as small as tenths of microns. Reproduced with permission from Ref. [332] Copyright ACS, 2023. Adapted from Kang et al. B) Stainless-steel hollow cones printed using powder-bed-fusion with selective laser melting (B.3) with $NiCo_2S_4$ nanoneedles grown in a posterior hydrothermal synthesis step. Reproduced with permission from Ref. [339] Copyright RSC, 2019. C) Cylindrical woodpile $CuZnAl_2O_3$ catalyst printed using material extrusion. Reproduced with permission from Ref. [340] Copyright Elsevier, 2024.

Recently, a coupled CFD–DEM and MC approach was introduced, where CFD–DEM tracks particle dynamics in fluidized beds, and the MC method predicts the coating layer.[299] Coupling CFD–DEM models with PBEs or MC simulations enables the quantitative tracking of particle-size distributions and structural heterogeneity. This approach can serve as a starting point for digital twin concepts in catalyst production. In future catalyst manufacturing, such frameworks will likely play a critical role in adaptive process control, enabling the real-time adjustment of process parameters in response to evolving material characteristics.

In summary, fluidized-bed spray granulation is a critical upscaling step in transforming engineered precursor systems into application-ready catalysts. This approach bridges the gap between nanoscale design, macroscale functionality, and reactor integration.

4.4. 3D Printing and Additive Manufacturing

Recently popularized as 3D printing and historically known as solid freeform fabrication, AM is a relatively novel manufacturing approach, encompassing technology based on diverse scientific principles. The characteristic feature of AM is that it constructs the parts layer-by-layer, providing considerable flexibility in building complex shapes.[307] This method has attracted attention from researchers, companies, and the public due to its flexibility and broad applicability prospects in numerous fields, such as biomaterials,[308] construction,[309] food processing,[310] and catalysis.[29]

4.4.1. Technology and Materials

The AM technique comprises a technology bundle developed for the bottom-up production of structured materials. Common AM technology can be classified into bulk methods and selective deposition methods. Below is a brief classification of the existing AM technology and suitable materials:[311]

- In bulk methods, including vat and powder bed methods, the piece is printed from the bulk of the starting material found in a container -generally- below the printing head and is gradually built.
  - Vat photopolymerization (VPP): Vat methods use various types of photocurable resins (with acrylate or epoxide groups) contained in a vat in liquid form. The resin can be combined with finely dispersed ceramic powders to produce ceramic pieces.[312–314] Typical printing resolutions via these methods are around 25 to 50 µm.[315] Depending on how resins are cured, several methods can be applied:
    - Stereolithography (SLA): Light is projected following a path on the resin surface to produce layers of partially cured material. The piece can "grow" vertically by increasing the depth of the vat during the printing process or by growing the piece "upside-down" while hanging from the printer head.
    - Digital light processing (DLP): This method is similar to SLA, but the light is projected in full layers onto the surface using micromirrors.
    - Liquid-crystal display (LCD): This approach is similar to DLP, but the light is projected using a laser light source masked using an LCD screen, also known as masked SLA.
  - Powder bed methods, in which the piece is constructed layerwise inside a bed of powdered solids, have a disposition similar to vat techniques. After a layer is printed, a new layer of fresh starting material is deposited on top of the previous layer. The resolution is of the same order as the VPP methods.
    - Binder jetting (BJT): The powder can be selectively bound by adding binder solution at specified positions on the bed. Materials, including common catalyst supports and other ceramics, can be processed to produce a 3D object.[316,317]
    - Powder bed fusion (PBF): The powder is bound by location-specific sintering or melting induced by a concentrated energy source, such as a laser (e.g., selective laser sintering or melting) or electron beam (e.g., selective electron beam melting). These methods suit thermoplastic materials, such as nylon, polystyrene, or metal.[318,319]
- Selective deposition methods: In contrast to vat or bed methods, the starting material in these methods is deposited layerwise to form the printed piece.
  - Material extrusion (MEX): This method is also known as robocasting or direct ink writing (DIW)[320,321] and involves a digitally controlled deposition of a viscoelastic solid–liquid suspension that operates by extrusion. A precursor suspension consisting of a mixture of powders (including binders) and liquids confers adequate rheological properties. Similar to ceramic processing, the printed body is carefully dried and calcined or pyrolyzed to produce the final piece. Virtually any material that can be processed via conventional extrusion can be processed via robocasting after tuning the rheological properties of the paste to match the pressure limitations of the extrusion 3D printer. The highest printing accuracy found in the literature was 0.2 mm, but in most cases, the accuracy is between 0.4 and 1 mm.
  - In fused deposition modeling (FDM), also known as fused filament fabrication, a filament of a thermoplastic material, such as polylactic acid, is melted at the nozzle and selectively deposited to form the piece. The typical printing resolution is 0.1 mm.
  - In direct energy deposition, a metal filament or powder is selectively deposited and melted on the printed piece using an energy source (e.g., a laser, electron beam, or plasma arc).[322] This technique is relatively infrequent for the AM of catalysts.
  - In material-jetting methods, droplets of precursor suspension (i.e., ink) are selectively deposited in a continuous or drop-on-demand manner. Piezoelectric or electrothermal actuators execute drop-on-demand jetting. The preparation of thin-layered catalysts based on metal oxides (e.g., titania) and catalyst supports (e.g., alumina) has been reported

Table 4. Summary of research (2023–2025) implementing AM technology to shape catalysts.

AM Technology	Additional treatment	Material	Structure	Scale; resolution (mm)	Application	Ref.
BJT and MEX	Thermal (air, 1100 °C), impregnation, thermal (air, 400 °C), thermal (H_2, 400 °C)	Pt/Al_2O_3	Perforated cylinder	$d = 18$, $h = 3$; 0.41 (DIW)	Green H_2: dehydrogenation of perhydro-dibenzyl toluene	[334]
FDM	Debinding (acetone bath), thermal (air, 600 °C), thermal (air, 900 °C to 1400 °C), impregnation, thermal (air or H_2, 800 °C)	$MnOx/Al_2O_3$, Pt/Al_2O_3	Cylindrical honeycomb with hexagonal channels	$d = 20$, $h = 15$; 0.4	Aerospatial: H_2O_2 decomposition	[353]
FDM	Thermal (Ar, 1200 °C), surface activation (optional), impregnation, thermal (air, 400 °C)	NiO/CeO_2/steel	Cylindrical honeycomb with square channels	$d = 26$, $h = 50$; 0.25	CCUS: CO_2 hydrogenation to CH_4	[354]
FDM	Electro-deposition	Ni/Carbon-PLA, Ni/Graphene-PLA	Cuboid	50*5*0.8; 0.1	Green H_2: O evolution reaction	[355]
FDM (sacrificial template)	Curing, thermal (N_2, 900 °C), impregnation (multiple), thermal (N_2, 500 °C)	$NiO\text{-}CeO_2/MgCO_3$/pyrolyzed resorcinol-CH_2O polymer	Cylinder with an infill comprising interconnected rings perpendicular to the flow axis	$d = 22$, $h = 38$; 0.15	CCUS: CO_2 hydrogenation to CH_4	[356]
MEX	Thermal (air, 1100 °C)	Mullite (kaolin)	Cuboid honeycomb with nine square or four triangular channels	25*25*12, 20*20*20; 1	CCUS: CO_2 desorption enhancement from monoethanolamine solution	[357]
MEX	Thermal (air, 550 to 650 °C)	ZSM-5	Cylindrical woodpile (offset angle and string distance varied)	$d = 30$; 1	CCUS: CO_2 desorption enhancement from monoethanolamine solution	[358]
MEX	Thermal (air, 500 °C)	$Cu\text{-}ZnO\text{-}Al_2O_3$/H-ZSM-5/$Al_2O_3$	Cylindrical or cuboid 90° woodpile	$d = 14$–25, $h = 40$–60; 0.5	CCUS: CO_2 hydrogenation to dimethyl ether	[340]
MEX	Thermal (air, 500 °C)	$CuO\text{-}ZnO\text{-}ZrO_2$/ZSM-5	Cylindrical 90° woodpile	$d = 12.8$, $h = 40$; 0.65	CCUS: CO_2 hydrogenation to dimethyl ether	[359]
MEX	Thermal (air, 450 °C)	Ni/SiOC	Cylindrical woodpile (offset angle and stacking pattern varied)	$d = 8$, $h = 30$; 0.2	CCUS: CO_2 hydrogenation to CH_4	[343]
MEX	Freeze-drying (only when bentonite is the binder), thermal (N_2, 550 °C), impregnation	Na-Fe/C/ pyrolyzed polyacrylonitrile or Na-Fe/C/ bentonite	Cylindrical woodpile (offset angle and stacking pattern varied)	$d = 12$; 0.4	CCUS: CO_2 hydrogenation to olefins	[360]
MEX	Thermal (air, 700 °C)	$Ce1-xCoxNiO_3$/CaO Perovskite	Cylindrical 90° woodpile	$d = 10$; 0.5	CCUS: dry reforming of CH_4	[361]
MEX	Freeze-drying, thermal (inert, 1000 °C), infiltration, thermal (inert, 1000 °C)	$Co@Co_3O_4\text{-}C/Al_2O_3/SiO_2$	Cylindrical woodpile	$d = 23$, $h = 10$; 0.8	Clean air: O_3 decomposition in the presence of H_2O	[362]
MEX	Freeze-drying, thermal (air, 550 °C)	Cu-SSZ-13@SiO_2	Cylindrical 90° woodpile (highly deformed)	$d = 10$, $h < 5$; 1	Clean air: selective catalytic reduction of NO with NH_3	[363]

Table 4. (Continued)

AM Technology	Additional treatment	Material	Structure	Scale; resolution (mm)	Application	Ref.
MEX	Crosslinking (acid bath), freeze-drying	Mn-Cu-O, Mn-Fe-O, Mn-Ce-O,	Cuboid honeycomb with different cell densities	42*42*2; 0.41	Clean water: catalytic wet peroxide oxidation of methylene blue	[364]
MEX	Thermal (N_2, 800 °C), hydrothermal growth, thermal (N_2, 450 °C), surface activation (HNO_3 bath), impregnation	Pd/TiO_2/ pyrolyzed lignine	Cuboid 90° woodpile	10*10*5; 0.51	Clean water: photocatalytic reduction of 4-nitrophenol	[365]
MEX	Freeze-drying, reduction in HI	Graphene-TiO_2	Cuboid 90° woodpile	6*6*2; 0.35	Clean water: photoelectro-catalysis using a self-powered photo-fuel cell	[366]
MEX	Thermal (Ar, 1100 °C), dealloying (acid bath), thermal (Ar, 850 °C), hydrothermal growth	Cu_4Fe_6-R, HKUST-1/Cu_4Fe_6-R	Cylindrical woodpile (highly deformed)	$d = 10$, $h = 10$; 0.3	Fuel & chemicals, clean water: 4-nitrophenol reduction/cyclization	[367]
MEX	Freeze-drying, optional: thermal (Ar, 700 °C), chloride coordination (HCl bath)	Metal single-atom catalysts on gelatin/ methacrylic, gelatin, agarose, alginate, or pyrolyzed gelatin/ methacrylic anhydride	Cuboid 90° woodpile	30*15*3; 0.3	Fuel & chemicals, clean water: electrocatalytic nitrate reduction to NH_3	[368]
MEX	Thermal (air, 550 °C), dopamine coating, impregnation, thermal (air, 50 °C)	Pt/Al_2O_3	Cylindrical woodpiles with different offset angles (30°, 45°, 60°, 90°) and a helicoidal rotation pattern	$d = 8$, $h = 30$, 0.6	Fuel & chemicals: catalytic oxidation of toluene	[341]
MEX	Thermal (air, 550 °C)	TS-1	Split cylindrical 90° woodpile (two pieces) with porosity gradients	$d = 80$ mm, $h = 39.6$; 0.8	Fuel & chemicals: catalytic oxidation of ethylene to ethylene glycol	[369]
MEX	Thermal (air, 550 °C)	3D-NiMo/Al_2O_3-MMT	Cylindrical woodpile	$d = 30$; 1.6	Fuel & chemicals: hydrodesulfurization	[370]
MEX	Impregnation, thermal (air, 500 °C), thermal (H_2, 350 °C)	Cu/γ-Al_2O_3	Cylindrical 90° woodpile	$d = 10$, $h = 10$; 0.5	Fuel & chemicals: CH_3OH steam reforming	[371]
MEX	Thermal (air, 550 °C)	Ionic liquid (1-vinyl-3-dodeca-midazolium phosphomolybdate), mordenite, bentonite	Cylindrical 90° woodpile	$d = 22$, $h = 7$; 1	Fuel & chemicals: oxidative desulfurization of fuel	[372]
MEX	Thermal (air, 550 °C or H_2, 800 °C)	MoC/Al_2O_3	Cylindrical 90° woodpile	$d = 10$, $h = 17$; 0.84	Fuel & chemicals: reverse water-gas shift reaction	[373]
MEX	Thermal (conditions not specified), thermal (H_2, 500 °C)	Co/Al_2O_3	Cylindrical 90° woodpile	$d = 20$, $h = 50$; 0.8	Fuel & chemicals: selective oxidation of benzyl alcohol to benzaldehyde	[374]
MEX (+ gelation)	Printing inside n-heptane/NH_3 bath, gelation, solvent exchange (2×), supercritical CO_2 drying	Au nanorod/TiO_2 aerogel	Cuboid 90° woodpile aligned vs. alternate stacking	15*15*(0.7 to 3); 0.25	Green H_2: photocatalytic H_2 production from H_2O/CH_3OH mixtures	[375]

Table 4. (Continued)

AM Technology	Additional treatment	Material	Structure	Scale; resolution (mm)	Application	Ref.
MEX (photo-curing)	Extrusion-based printing is aided by photocuring	Carbonic anhydrase/ hydrogel	Cylinder with alternating layers of linear patterns with different offset angles	$d = 20$, $h = 100$; 1	CCUS: biocatalytic CO_2 capture into a K_2CO_3 solution	[376]
PBF (SLM and SEBM)	Thermal (air, 500 °C), dip-coating, thermal (air, 500 °C)	$Fe_2(MoO_4)_3/SiO_2/Ti_6Al_4V$, $Fe_2(MoO_4)_3/SiO_2/AlSi_{10}Mg$	Cylinder with BCC lattice infill (various cell densities)	$d = 30$, $h = 100$; 0.15	Fuel & chemicals: partial oxidation of CH_3OH to CH_2O	[319]
PBF (SLM)	None	Cu (anodes), Stainless steel (cathodes)	Porous rods	$d = 3.5$, $h = 80$; 0.055	CCUS: CO_2 electroreduction	[377]
PBF (SLM)	Electro-deposition, thermal (air, 500 °C), thermal (H_2, 750 °C)	Ni/stainless steel, Ce/ stainless steel, Ni/Ce/ stainless steel, Ni-Ce/ stainless steel	Cylindrical honeycombs with square, triangular, hexagonal, and circular channels and various channel densities	$d = 20$, $h = 25$; 0.04	CCUS: dry reforming of CH_4	[378]
PBF (SLM)	Surface activation (acid), electro-deposition	Co/stainless steel	Cuboids with BCC and overlapping BCC lattices	15*15*(4.5 to 15); 0.05	Clean water: antibiotic (sulfamethoxazole, norfloxacin, bisphenol A) removal from water	[379]
PBF (SLM)	None	Cu-Ti	Cube with a diamond lattice infill	10*10*10; 0.04	Clean water: ciprofloxacin (antibiotic pollutant) removal	[380]
PBF (SLM)	None	Co with stainless steel	Cylindrical honeycombs with square and hexagonal channels and various channel densities	$d = 10$, $h = 12$; 0.07	Green H_2: borohydride hydrolysis	[381]
PBF (SLM)	Hydrothermal growth, thermal (N_2, 400 °C), grafting, impregnation	Pd/Cu-BDC-NH_2/Cu, Cu-Pd/C-PhN_2/Cu	Cylindrical honeycomb with various channel densities	$d = 23$, $h = 70$; 0.02	Green H_2: catalytic H_2 production from liquid-phase H_2 carriers	[382]
PBF (SLM)	Hydrothermal growth	$NiCo_2S_4$ nanoneedles on stainless steel	Plate with column/ cone arrays with various porosity values and perforation patterns	16.7*16.7; 0.1	Green H_2: O evolution reaction	[339]
PBF (SLM)	Electrochemical deposition and hydrothermal growth	CoNiCH nanoneedles/Ni/Ti_6Al_4V	Solid and porous cylinders with vertical square channels and horizontal circular channels	$d = 15$, $h = 2$; 0.03	Green H_2: O evolution reactions and water splitting	[383]
PBF (SLS or SLM)	Dealloying (base bath), thermal (air, 260 °C), thermal (H_2, 280 °C), reduction (CH_3OH vapor, 280 °C)	Cu-$ZnO_{50}/Al_{45}Cu_5Zn$	Cylinder with a gyroid infill	$d = 20$, $h = 50$; 0.045	Fuel & chemicals: CH_3OH steam reforming	[338]
PBF (SLS)	Selective electrochemical dissolution, thermal (H_2, 400 °C)	Ni/Hastelloy X ($Ni_{50}Cr_{21}Fe_{17}Mo_9$ alloy)	Cylindrical honeycomb with square channels	$d = 23$, $h = 70$; 0.06	CCUS: CO_2 hydrogenation to CH_4	[384]
PBF (SLS)	None	NiMo, NiCr, NiFe, NiCo	Ring with textured surface	$d = 25$, $h = 15$, $w = 5$; 0.02	Green H_2: oxygen and hhydrogen evolution reactions	[385]

Table 4. (Continued)

AM Technology	Additional treatment	Material	Structure	Scale; resolution (mm)	Application	Ref.
VPP (DLP)	Thermal (air, 1180 °C or 1250 °C), impregnation, thermal (air, 400 °C), thermal (H_2, 400 °C), repeat the impregnation and thermal treatment	Pt/Al_2O_3, Pt/cordierite	Cylinders with gyroid or triangular honeycomb infills (various voids)	d = 24.5, h = 33.5; x,y = 0.057, z = 0.05	Aerospatial: H_2O_2 decomposition	[329]
VPP (DLP)	Thermal (air, 350 °C)	CuO-ZnO-ZrO_2/ZSM-5	Cube with gyroid infill	10*10*10; 0.064	CCUS: CO_2 hydrogenation to CH_3OH	[386]
VPP (DLP)	Surface activation (base bath), dopamine coating, Ag coating (Tollens reaction), impregnation	Ag/resin, $C_{12}H_{26}S$-Ag/resin	Cylinders or cuboids with BCC or BCC-based overlapping lattice infills	10 to 15; 0.1	Clean water: organic pollutant removal	[327]
VPP (DLP)	Thermal (air, 650 °C), impregnation, thermal (air, 200 °C)	Fe_2O_3/TiO_2/Al_2O_3	Cubes with Kelvin (truncated octahedra) lattice infills	10*10*10; 0.035	Clean water: photo-Fenton reaction for acetaminophen and methylene blue removal	[387]
VPP (DLP)	None	Bi-MOF/resin	Cuboid honeycomb with hexagonal channels	18*18*2; 0.05	Clean water: rhodamine B removal	[388]
VPP (DLP)	Thermal (Ar, 900 °C), dip-coating (2×) hydrothermal growth	ZnO/pyrolytic carbon	Cube with a simple cubic lattice	10*10*10; 0.01	Clean water: rhodamine B removal	[389]
VPP (DLP)	Impregnation, growth	NiFe metaborate oxyhydroxide/resin	Plates with various reliefs (sea urchin-inspired)	10*10*2; 0.1	Fuel & chemicals, clean water: electrocatalytic nitrate reduction to NH_3	[390]
VPP (DLP)	Thermal (air, 1200 °C), seed impregnation, thermal (air, 550 °C), hydrothermal, thermal (air, 550 °C), ion exchange (2×), thermal (air, 550 °C	42% H-ZSM-5, mullite, cristobalite	Cylindrical 90° woodpile	d = 15, h = 10; 0.08	Fuel & chemicals: catalytic cracking of n-octane and 1,3,5-triisopropylbenzene	[391]
VPP (DLP)	Thermal (air, 1200 °C), seed impregnation, thermal (air, 550 °C), hydrothermal (2×), thermal (air, 550 °C), ion exchange (2×), thermal (air, 550 °C)	36% nanoH-ZSM-5/H-ZSM-5, mullite, cristobalite	Cylindrical 90° woodpile, alternated stacking	d = 15, h = 14.3; 0.08	Fuel & chemicals: catalytic cracking of polyethylene-derived pyrolysis oils	[392]
VPP (DLP)	Thermal (air, 600 °C), infiltration with boehmite, thermal (air, 600 °C)	Al_2O_3	Cylinder with various infills (square 2D channels, gyroid, Schwartz P, FCC lattice)	d = 10, h = 20; 0.04	Fuel & chemicals: ethanol dehydration to diethyl ether	[393]
VPP (DLP)	Thermal (N_2, 1000 °C), impregnation (multiple), thermal (N_2, 380 °C), thermal (H_2, 300 °C)	Cu-Zn-Al-Zr/Al_2O_3/pyrolyzed resin	Cuboid with gyroid, Schwartz, diamond, neovius, lidinoid, and split P lattices infill	10*10*150; 0.056	Fuel & chemicals: CH_3OH steam reforming	[394]
VPP (DLP)	Thermal (air, 1400 °C or 1500 °C), impregnation, thermal (air, 850 °C)	MnOx- and Na_2WO_4 over Al_2O_3 (corundum) or kaolin	Cylindrical honeycomb with hexagonal channels	d = 12, h = 6; x,y = 0.03, z = 0.05	Fuel & chemicals: oxidative coupling of CH_4	[395]

Table 4. (Continued)

AM Technology	Additional treatment	Material	Structure	Scale; resolution (mm)	Application	Ref.
VPP (DLP)	Thermal (air, 600 °C), infiltration, thermal (air, 600 °C), impregnation, thermal (air, 300 °C)	Au/Al_2O_3	Cylinders with different infills: Schwartz primitive, gyroid, FCC	$d = 10$, $h = 20$; 0.04	Fuel & chemicals: oxidative dehydrogenation of bioethanol	[396]
VPP (DLP)	Thermal (N_2, 900 °C), electrodeposition	Cu or Ni over pyrolyzed resin	Cube with a simple cubic lattice infill	10*10*10; 0.01	Green H_2: hydrogen evolution reaction	[397]
VPP (DLP)	Surface activation (oxidation), ion exchange, reduction, electroless Ni deposition, chemical deposition of NiFe phosphite	$NiFe(PO_3)O(OH)/PA$	Plates with various reliefs (flat, simple cubic, BCC, BCC octahedron, and cup array)	10*10*2; 0.1	Green H_2: O evolution reaction	[398]
VPP (LCD)	Thermal (Ar, 450 °C), thermal (air, 600 °C), thermal (air, 1000 °C),	Co/SiC, Ni–Co/SiC	Cuboids with simple cubic or Kelvin (truncated octahedra) lattice infills	10*10*10 or 20*20*0.7; 0.06	Clean water: methylene blue removal	[399]
VPP (LCD)	Surface activation (cold plasma discharge), polyvinyl-phosphonic acid coating, complexation-assisted precipitation grafting, complex-ation-assisted precipitation	Ni-MOF/BiOI/$AgVO_3$/resin	Fractal imprint on a plate	$d = 30$; 0.01	Clean water: photocatalytic rhodamine B removal	[332]
VPP (LCD)	Surface activation (cold plasma discharge), poly-dopamine coating, grafting, complex-ation-assisted precipitation (2×)	$SrAl_2O_4$:Eu_2+,Dy_3+/Ni-MOF/BiOBr/resin	Fractal imprint on a plate	$d = 30$; 0.01	Clean water: photocatalytic rhodamine B removal; Green H_2: photoelectrocatalytic hydrogen evolution reaction	[400]
VPP (LCD)	Thermal (inert, 1000 °C), atomic layer deposition	Pd/SiOC	Cylindrical 90° woodpile	$d = 15$, $h = 2.5$; 0.05	Fuel & chemicals: 4-phenylphenol synthesis by Suzuki–Miyaura coupling	[401]
VPP (LCD)	Thermal (N_2, 700 °C)	MoO_3/Al_2O_3/ pyrolyzed resin	Cube with gyroid infill	20*20*20, 0.05	Fuel & chemicals: oxidative desulfurization of fuel	[402]
VPP (LCD)	Thermal (N_2, 750 °C), surface activation (base bath), hydrothermal growth	$MoWO/SiO_2$/pyrolyzed resin	Cube with tetrahedral-octahedral lattice infill	18*18*12; 0.05	Fuel & chemicals: oxidative desulfurization of fuel	[403]
VPP (LCD)	None	Ni/CN_x (single-atom catalyst), CN_x	Screw-like reactor	$d = 6$, $h = 60$; 0.05	Fuel & chemicals: photocatalytic oxidation of benzyl alcohol to benzaldehyde	[404]

Table 4. (Continued)

AM Technology	Additional treatment	Material	Structure	Scale; resolution (mm)	Application	Ref.
VPP (not specified)	Thermal (Ar, 950 °C), impregnation	Ni, Fe/ pyrolyzed resin	Flower	13*13*10; 0.05	CCUS: CO_2 electrocatalytic reduction	[328]
VPP (SLA)	None	TiO_2/resin	Impeller with 10 arms	Tenths; 0.05	Clean water: rhodamine B removal	[405]
VPP (SLA)	Spray-coating (2×)	Cobalt telluride-conductive carbon/resin	Plate with a pattern of conical spikes	10*10, spikes $d = 0.5$, $h = 3$; 0.025	Green H_2: oxygen and hydrogen evolution reactions	[326]

Note: Material nomenclature has been simplified. Resolution indicates the minimum feature size that was accurately printed. AM: additive manufacturing, BCC: body-centered cubic, BJT: binder jetting, CCUS: carbon capture utilization and storage, DIW: direct ink writing, DLP: digital light processing, FCC: face-centered cubic, FDM: fused deposition modeling, LCD: liquid-crystal display, MEX: material extrusion, MOF: metal–organic framework, PBF: powder bed fusion, PLA: polylactic acid, SEBM: selective electron beam melting, SLA: stereolithography, SLM: selective laser melting, SLS: selective laser sintering, VPP: vat photopolymerization, ZSM: zeolite socony mobile.

using this method.[323] This method can also be employed for printing photocurable inks, which can contain dispersed solid particles of various natures.[324]

- In sheet lamination, sheets of material (usually adhesive paper, metals, or thermoplastics) are bonded to form a part. No explicit reports of sheet lamination for shaping catalysts were found, although some recent advances in industrial catalyst support configurations indicate that similar principles are currently used.[325]

These methods have been implemented differently in developing catalytic processes, given their material restrictions and compatibilities. Methods based on VPP are practical for direct 3D printing of low-temperature catalyst supports for electrocatalytic or photocatalytic applications.[326–328] However, the possibility of adding ceramic or metal particles to the resin mix has expanded their overall application scope to other material types.[329–331] Very small architectures can be accurately printed using VPP methods (Figure 11a).[332]

Moreover, BJT methods are not frequent, and the catalyst shapes reported in the scientific literature are relatively simple,[333–335] but more fundamental work has demonstrated that this technique could be promising with the proper post-treatment strategies.[317,336] The PBF methods can attain high precision and shape complexity and are less susceptible to shrinkage and optimization problems than VPP methods, although they require relatively harsh multistep post-processing to achieve functional surfaces.[337,338] In addition, PBF methods allow for small features to be printed with high accuracy (Figure 11b), and post-treatment can provide a highly hierarchical structure (Figure 11b.3).[339]

In addition, MEX has been the most frequently accessed technique for AM for catalysts due to its conceptual simplicity and similarity to traditional extrusion. Virtually any material can be printed using this technique after the proper formulation of the paste by tuning the rheology,[340] although its performance is limited by its printing resolution (>0.2 mm) and the shape deformation of the printed materials.[341,342] The internal designs attainable by MEX techniques are mostly woodpile-based (Figure 11c),[340] revealing how this technique falls short in terms of shape optimization.[343] Nevertheless, the prospects for shape optimization from advances in rheological property control and printer/nozzle characteristics are promising and largely unexplored. The FDM method has become very popular due to the surge of home 3D printers for hobbyists. This method is limited by the number of available thermoplastic options for filaments and the difficulty of producing tailored filaments with the right windability and printability.[344] Due to the limitations of producing objects in shapes other than thin layers, material-jetting methods are practical for AM of advanced electronics but have received much less attention in general catalyst shaping.[345]

4.4.2. Recent Advances

In the late 1990s to early 2000s, Cesarano et al.[320,346,347] reported the first application of AM in catalyst production called "robocasting." Their work from 2004 reported the preparation of a

"woodpiled" monolith with no line-of-sight paths for CH_4 catalytic combustion. The catalyst was made of alumina coated with barium manganese hexaaluminate or hexaaluminate alone as the robocasted material.

Despite other AM methods being developed in the late 1980s, their use in catalyst shaping was not reported until later. In the case of VPP methods, their first implementation for catalyst shaping was in 2010, when Zahraa et al.[348] produced a photocatalytic reactor for air treatment, where elongated mixers with various designs were coated with TiO_2 nanoparticles and tested for CH_3OH removal as the model pollutant. The FDM method was first employed in catalyst shaping in 2014 when Liu et al.[349] used an acrylonitrile butadiene 3D-printed piece to support an in situ grown Cu-BTC MOF. The composite material was tested in the removal of methylene blue. In 2015, Ambrosi et al.[350] demonstrated the entry of PBF methods into the catalyst-shaping option, reporting on producing helical stainless-steel electrodes coated with IrO_2 for the oxygen evolution reaction.

Since then, researchers have increasingly become involved in developing catalysts using existing and novel AM approaches. Recently, several authors reviewed AM for catalyst and reactor production.[351,352] Therefore, this work restricts the scope of this section to research published from 2023 to 2025, covering catalyst shaping via 3D printing.

Table 4 summarizes the work included in this study. In the last few years, VPP has been the most frequently employed method (25/67) for producing 3D-printed catalysts (Figure 12a). Most catalysts produced via VPP were tested for the production of fuel or chemicals (11/25), followed by wastewater treatment (8/25). The MEX method is the next-most popular technique (24/67) to produce 3D-printed catalysts, which were tested in fuels and chemicals production (9/24) or in carbon capture utilization and storage (CCUS) applications (8/24). The PBF methods are also relatively popular (14/67), with a notable amount of work addressing green hydrogen production or transport (6/14). Finally, FDM (4/67) and BJT (1/67) have been the least frequently reported catalyst production methods since 2023. Overall, the 3D-printed catalysts have been developed and tested in the context of relevant industrial applications (Figure 12b), such as fuel and chemical production (23/67), CCUS (15/67), wastewater treatment (13/67), and green H_2 production (13/67), with scarce testing in aerospatial applications (2/67) and air cleaning (2/67).

4.4.3. Case Studies

The potential of AM techniques to enable the rational design of catalysts at various scales is enormous. The number of accessible geometries is virtually unlimited, especially for VPP and PBF methods, with unprecedented control over surface features down to a few micrometers. Developing ceramic- and metal-loaded resins for VPP or filaments for FDM offers the possibility to shape materials that are sensitive to water or pressure or are highly hydrophobic and cannot be easily shaped via conventional approaches, such as granulation, pelletization, extrusion, casting, or foaming.[60,63] Moreover, the accessibility of computer-aided design software or online 3D-model repositories allows researchers new to the field to develop shaping procedures rapidly for their materials.

This work discusses several highly illustrative examples of this revolution in catalyst design. The rise of 3D printing for catalyst and reactor manufacturing is heavily supported by CFD simulations, allowing the optimization of object geometry to control the mass and heat flow and improve catalytic performance.[351] The summary below discusses some fascinating research topics and concepts that illustrate the power of 3D printing to design catalysts and catalytic processes rationally.

A crucial strength of 3D printing is the possibility of fine-tuning the structure based on the CFD simulation results. Inspired by helical structures in some arthropod exoskeletons, Xu et al.[341] proposed a series of Pt/Al_2O_3 woodpile catalysts prepared using robocasting and impregnation for toluene catalytic oxidation. They studied various offset angles (α) of the stacked linear patterned layers (Figure 12a) and found that the catalyst with a helicoidal arrangement of layers $\Delta\alpha = 30$ produced the best catalytic activity (90% conversion at 190 °C and a WHSV = 30 L/g/h), closely followed by others with $\alpha = (30°, 45°, 60°)$. The typical $\alpha = 90°$ woodpile performed the worst. As determined using CFD simulation, the reason for this performance was that the helicoidal and nonright-angle arrangements create more intense turbulence, favoring mass transfer despite a slightly higher pressure drop.

Tsubaki et al.[360] tested a similar idea by studying robocasted woodpile configurations of Na–Fe/C MOF-derived catalysts for hydrogenating CO_2. Of the three studied stacking configurations, the typical woodpile, an alternated alignment woodpile, and helicoidal stacking, the latter performed best in terms of the olefin-to-paraffin ratio, olefin selectivity, temperature distribution, and time-on-stream stability, and the lowest selectivity toward CO. The helicoidal woodpile presented the highest local velocity, indicating high turbulence, moderate pressure loss, and the best temperature homogeneity, diminishing the risk of hot spots and thermal runaway. The mechanical strength was very poor (<0.5 MPa) using the bentonite binder, whereas pyrolyzed polyacrylonitrile-bound catalysts had a crush strength of 1.7 MPa, which is acceptable for a structured catalyst. Overall, the helicoidal catalyst performed comparably to other Fe–Na-based catalysts but had one of the best space-time yields.

Wu et al.[403] studied the effect of the surface microstructure on the flow pattern, pressure loss, and catalytic performance of molybdenum tungstate (MoWO) catalysts for oxidative desulfurization of fuels. They prepared a porous open-cell structure catalyst based on tetrahedral–octahedral units via LCD 3D printing, pyrolysis, alkaline etching, and growth of the active MoWO phase. The catalyst prepared this way displayed well-dispersed needle-like MoWO features (0.1 × 0.01 μm) on the surface, which were absent if the microcrystalline cellulose was absent in the ink formulation or formed dense aggregates if the etching step was skipped (Figure 12b). The catalyst with recognizable needle-like microstructures presented the highest sulfur removal at 70 °C, about 100% after 100 min with a turnover frequency of 1.34/h, which only decreased by 3% after 25 cycles. The CFD simulations revealed enhanced mixing and mass transfer due to the higher turbulence in catalysts displaying needle-like features.

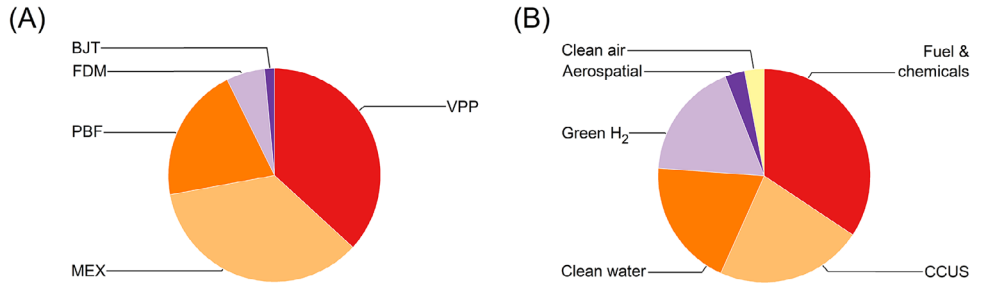

Figure 12. Three-dimensional printing method frequency trends: a) catalyst production methods and b) application fields.

Despite poor reported mechanical strength (0.27 MPa), the catalyst was successfully shaped as an impeller, as demonstrated at the laboratory scale.

Busse et al.[406] studied various catalyst support structures to assess their prospects in heat management. Based on their previous results on support geometry optimization, they prepared several catalysts comprising metallic support printed as a porous open-cell structure using PBF methods, which were later dip-coated in $Fe_2(MoO_4)_3$ and tested in the partial oxidation of CH_3OH to formaldehyde (CH_2O). These supported $Fe_2(MoO_4)_3$ catalysts provided close to 100% CH_3OH conversion, >92% CH_2O selectivity, and low CO selectivity, but the support primarily determined the heat transfer. The support phase with the highest conductivity (i.e., $AlSi_{10}Mg$) demonstrated five times lower temperature gradients than a SiC powder or alumina bead-supported catalyst and gradients four times lower than a 3D-printed Ti_6Al_4V alloy. Manufacturing a catalyst with a positive porosity gradient along the flow axis (Figure 13c) decreased the temperature gradients by 70%.[319]

In photocatalysis and photoelectrocatalysis, light exposure, and light harvesting optimization parameters can be significantly improved via a rational design and AM. Interesting examples are observed in the manufacture of catalysts based on gold (Au) nanoparticles supported on TiO_2 nanostructures, where researchers have studied manufacturing parameters to address light utilization and catalyst performance at various scales.

Casanova et al.[407] robocasted a simple woodpile TiO_2 support without a binder, which they impregnated with Au nanoparticles for the photocatalytic production of H_2 from water/ethanol vapor mixtures. The authors studied the effect of pre- and post-impregnation, finding that the post-impregnation route was superior because it led to Au nanoparticles deposited exclusively on the surface, achieving activities that were two to three orders of magnitude higher at a lower total Au nanoparticle loading. Materials robocasted with the thinnest possible material filaments (0.2 mm) presented the highest activity due to a higher exposed surface area despite very similar irradiance (Figure 14a).

Koziej et al.[375,408] proposed a substantially different approach to improve catalyst efficiency in the photocatalytic production of H_2 from H_2O/CH_3OH. They combined robocasting with gelation similar to some 3D-printing techniques for biological materials and produced translucent Au/TiO_2-loaded gels as simple and alternating woodpile structures (Figure 14b.1). The alternating woodpile (called an FCC unit cell by the authors) results are optimal because it uses light similarly to an unstructured aerogel (Figure 13b.2) with a pressure decrease that is five-orders of magnitude lower. The H_2 evolution rate was about five times higher than when the nanoparticle powder was the catalyst.

Guo et al.[409] reported another interestingly structured $Au/TiO_2/Al_2O_3$ catalyst for photocatalytic N_2 fixation to NH_3 (Figure 14c). The catalyst was printed as a forest-like arrangement of vertically aligned needles with a diameter of 0.6 mm each, regularly spread across a 1 cm^2 square alumina support. The TiO_2 hydrothermal growth, as nanorod arrays and Au nanoparticles self-assembled, produced the final catalyst with a 15-fold higher photocatalytic N-fixation performance than planar TiO_2 films decorated with Au nanoparticles.

Further, AM of electrically conductive materials enables unique preparation routes and applications in catalysis by taking advantage of micro-, meso-, and macroscopic properties. Ding et al.[339] developed highly efficient electrodes for the oxygen evolution reaction via PBF and the hydrothermal growth of $NiCo_2S_4$ nanoneedles (Figure 11b). They screened performance, converting from a planar stainless-steel substrate to several configurations consisting of column and cone arrays, including modifications of wall porosity and additional hole creation (macropores). The 3D printing approach allowed them a 7-fold increase in the substrate surface area, as per the model, translating into a 9-fold increase in the electrochemically active surface area in the printed material and a 21-fold increase when compared after $NiCo_2S_4$ nanoneedle growth. This method resulted in excellent electrocatalytic activity with very low overpotential (226 and 277 mV at current density values of 10 and 100 mA/cm^2, respectively) and fast bubble-escaping properties.

Reproduced with permission from Ref. [375] Copyright ACS, 2023. (C) Plasmonic forest-like TiO_2-based microstructures prepared via a combination of 3D printing and post-treatment. Reproduced with permission from Ref. [409] Copyright Wiley, 2021.

Vidal et al.[378] studied the manufacture of stainless-steel honeycomb monoliths prepared using PBF to support CH_4 dry-reforming catalysts. The most promising catalyst was obtained using the sequential electrodeposition of cerium (Ce) and then Ni, producing conversions of 94% to 97% for CH_4 and of 96% to 98% for CO_2, and H_2/CO selectivity of 0.71 to 0.79, without deactivation after 44 h (750 °C with a 1:1 CH_4/CO_2 mol ratio).

Zhou et al.[394] developed a series of electrically conductive catalysts based on Cu–Zn–Al–Zr/Al_2O_3/C for CH_3OH steam reforming capable of direct electric heating via the Joule

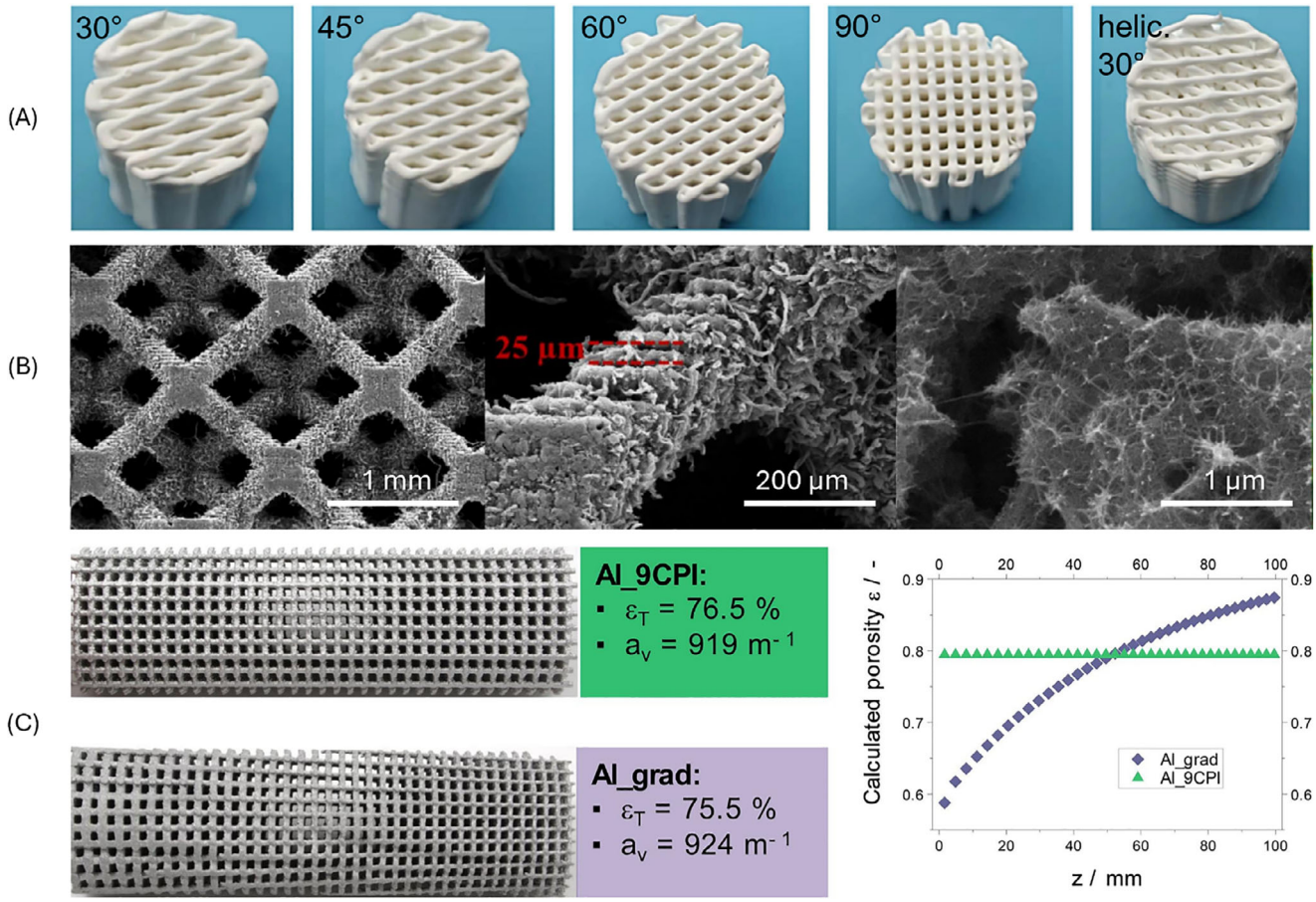

Figure 13. Catalysts produced via 3D-printing approaches modeled and studied via CFD simulations: a) alumina woodpile structures with various offset angles. Reproduced with permission from Ref. [341] Copyright Elsevier, 2023. b) Needle-like MoWO-based catalyst grown on a tetrahedral–octahedral periodic open-cell structure comprising pyrolyzed resin. Reproduced with permission from Ref. [403] Copyright Elsevier, 2025. c) Highly conductive $AlSi_{10}Mg$ alloy printed as a cubic lattice with constant and gradient porosity for improved thermal transfer. Reproduced with permission from Ref. [319] Copyright Elsevier, 2024.

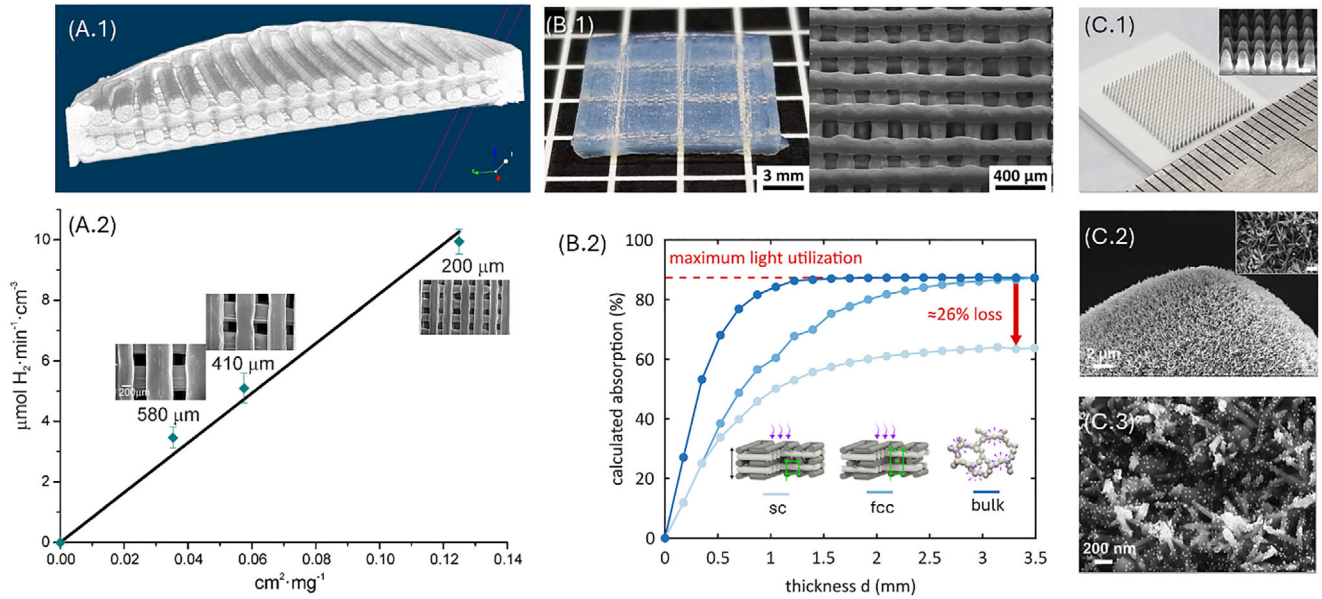

Figure 14. Approaches maximizing light utilization in TiO_2-based photocatalysts: a) TiO_2 printed using material extrusion (MEX); smaller nozzle openings employ light better. Reproduced with permission from Ref. [407] Copyright Springer Nature, 2019. b) Translucent TiO_2-containing gel printed via MEX in a face-centered-cubic woodpile structure, improving the light utilization, pressure decrease, and mass transfer.

effect. They printed an Al_2O_3-loaded (65% weight) acrylate-based pyrolyzed resin using DLP, which impregnated the catalyst precursors. The catalysts were interconnected and included diamond-, Schwarz-, and gyroid-type structures. The catalysts displayed excellent electrothermal stability (>12 h) and fast heating and cooling to 300 °C (100 s). A maximum CH_3OH conversion of 98% and an H_2 production rate of 101 mmol/h were achieved on the Schwarz-type structure, with a 76.3% lower power consumption than in external heating.

There are multiple other examples where 3D printing has contributed to innovative processing or design approaches to control the properties and applicability of the manufactured material at various scales. For instance, Wu et al.[327] developed a DLP-printed device with ultra-fast oil/water separation, catalytic activity for dye removal, and antibacterial properties. The device was printed, forming complex structures based on a body-centered cubic porous open-cell structure, where the unit cell overlapped at certain degrees (0% to 40%) with the surrounding unit cells. The printed pieces were impregnated with silver (Ag) or a stepwise combination of Ag and dodecane thiol, rendering hydrophilic and hydrophobic materials, respectively. The Ag-impregnated material with an overlap of 35% displays over twice as fast reaction kinetics and fluxes than conventional lattices with equivalent density and high mechanical strength values.

In a different use case, Yu et al.[338] developed a PBF-printed metallic (Al–Cu–Zn alloy, 50:45:5 mass ratio) support as a cylinder with a gyroid infill, the surface of which was subject to dealloying, oxidation, and selective reduction treatments to form a catalytic surface of Cu/ZnO. They demonstrated that the catalytic site activity can be tuned by varying the conditions in the activation step. The catalyst demonstrated good mechanical strength (7.61 MPa) and enhanced catalytic activity in CH_3OH steam reforming compared to a commercial $Cu/ZnO/Al_2O_3$ beaded catalyst, with higher CH_3OH conversion and H_2 yield at lower temperature, lower CO selectivity, and similar time-on-stream stability. The CFD simulations revealed that the structured catalysts present much faster mass and heat transfer than a catalyst bed containing commercial catalyst beads.

4.4.4. Technical Challenges

Today, AM has revolutionized the field of catalyst shaping by introducing an unprecedentedly wide range of possibilities in terms of shapes, materials, and applications. The applicability prospects still have room to expand, especially as the techniques continue to develop and their limitations are overcome. Therefore, the current limitations of AM as a whole and in individual 3D-printing technology must be discussed.

Scaling up is the first and most critical limitation of AM in catalysis. Catalysts produced using AM techniques typically involve a much longer production time than similarly sized pieces produced via extrusion. Complex or expensive post-treatment steps (e.g., pyrolysis, surface conditioning, and multiple thermal treatments) may be necessary.[367,383,391] Few studies have explicitly addressed production upscaling.[340] The sizes in which catalytic materials have been produced using 3D printing have typically been less than 10 cm (Table 4), although larger pieces have been reported.[318,369,394,410] There is also interest in out-scaling instead of upscaling (i.e., increasing the number instead of the size) for 3D-printed reactors.[351]

Other critical limitations are specific to the technique. For instance, VPP techniques can be employed to print photocurable mixtures containing ceramics, but the penetration depth of the light limits the ceramic content of the mix.[399,401] This problem can diminish the mechanical strength and catalyst loading, increase shrinking, decrease the overall material yield, and worsen the sustainability parameters.

However, some post-treatment strategies can improve the mechanical strength and overall performance of some materials. For instance, Lin et al.[391,392] demonstrated that crush strength and cracking activity are enhanced via the hydrothermal treatment of a 3D-printed metakaolin and diatomite precursor (after debinding and sintering) to promote in situ transformation to a zeolite phase. For alumina, infiltration with colloidal boehmite suspensions after debinding can improve the mechanical resistance with a minor effect on catalyst porosity compared with high-temperature sintering.[396] Moreover, FDM technology requires a windable filament to operate, which (similarly to VPP) limits the ceramic content and decreases the final material yield.[344] If the resin or filament is meant to be pyrolyzed, this requires specific heating equipment that operates in a vacuum or controlled atmosphere, which can be very expensive from an upscaling perspective.

The PBF methods yield materials with high mechanical strength, especially when the starting material is a metal.[338,379] Metal-supported catalysts have various interesting use cases due to their thermal and electrical conductivity but are still limited due to their high weight, opacity, and possible chemical incompatibilities. In addition, MEX technology is very flexible regarding which materials can be shaped, but the resolution is typically low (>0.2 mm). Most shapes are based on piling printed strings (woodpiles and variants), and the mechanical strengths are frequently poor.

Generally, the mechanical properties and structural defects of 3D-printed catalysts are not often discussed.[307] In most cases reported in the literature, especially in MEX and VPP methods, the mechanical strengths are well below those of extruded or granulated catalyst particles, increasing packaging and transportation prices and preventing the use of these catalysts in applications that involve high pressure or mechanical wear of other types. Furthermore, many MEX approaches result in pieces with many surface defects and deformed features, leading to bias if an idealized structure is modeled.

5. Emerging Technologies

5.1. Intricate Structures

As a shaping approach, AM offers more flexibility and control over the specific material properties and geometry a priori, allowing for greater complexity and intricacy, which can be

based on the composition distribution and geometry. Regarding compositional intricacy, multimaterial 3D printing enables composition gradients and transitions throughout the printed object that can result in the spatial distribution of physicochemical properties. Multimaterial 3D printing was first proposed as a viable approach for a direct energy deposition method to produce a metallic object with distinct compositional regions.[322] Later, Cesarano et al.[411] proposed robocasting, and Jafari et al.[412] extended this method to FDM, and Wicker et al.[413] used multiple resin vats to extend it to SLA.

This approach has been expanded in several ways. Rocha et al.[414] studied multimaterial DIW using two different nozzles loaded with graphene- and Cu-based inks to prepare high-capacitance electrodes. In addition, Credi et al.[415] printed a Ni circuit on a resin support using a dual precursor SLA approach, in which the support was first printed using photocurable resin, and the circuit skeleton was printed on top of it using Ni-particle-loaded resin and posterior etching and additional electroless Ni deposition.

Schlögl et al.[416] developed multimaterial objects presenting regions with substantially different mechanical properties using a dual-wavelength vat approach combining two resin monomers. The monomers were selectively cured under irradiation at a specific wavelength. Helmer et al.[417] developed a DLP method, where the resin composition was gradually modified by adding a porogen throughout the printing process, resulting in the final printed objects having porosity, translucency, hydrophilicity, and mechanical strength gradients.

Ye et al.[363] produced core-shell Cu-SSZ-13 on SiO_2 monoliths using a DIW approach with a coaxial two-compartment nozzle for NH_3-selective catalytic reduction. The hierarchical porosity generated by the outer silica shell significantly improved the mass transfer and catalytic performance. They demonstrated that their novel multimaterial DIW method could also be applied to other material combinations, although the shape fidelity of the printed pieces was relatively poor, probably due to low resistance to the flow of ink. These examples inspire methods of tuning catalyst properties using multimaterial AM approaches. These approaches hold great promise for photocatalyst shaping.

The spatial resolutions of the available techniques must be examined regarding geometric intricacy. The highest resolution reported in a commercial 3D printer is 0.1 µm, available for micro 3D printing and patterning via SLA, mostly using flat surfaces as support.[418] This technology could be implemented in photocatalyst 3D printing at a small scale or in electrocatalysis to produce optimized electrode surfaces, assuming that resins can be modified to contain the desired active phases in pre- or post-printing. However, this patterning technology has not yet been implemented in centimeter- or decimeter-sized 3D structured substrates, preventing it from wider adoption in other catalysis applications. From a more generic perspective, the greatest detail and geometrical complexity in catalytic bodies can be achieved through the VPP and PBF methods with typical layer resolutions of tenths of a micrometer.

Additionally, these methods can produce mechanically stable and strong structured catalysts if the process parameters (primarily the composition and thermal treatment) are optimized. Furthermore, fueled by the interest in material development, the pool of printable materials using these methods is continuously expanding, and improvements to the techniques are on par with the emerging material needs. The FDM methods can also be developed as new filament materials are produced and printing resolutions are enhanced.[344,419] The MEX method is still one of the simplest AM approaches, with great potential to produce mechanically strong materials with substantial structural freedom compared with extruded monoliths despite their relatively low printing resolution.

Nevertheless, paste rheology optimization for extrusion-based 3D printing is a very complex process, where a compromise must be found between i) extrudability, ii) printability (i.e., the geometrical fidelity of the green piece compared to the digital model), and iii) structural stability.[340,365,386,409] A deviation from the typical woodpile-based structures should be sought for this technique to remain competitive with others from an innovation viewpoint. Various approaches can favor this development and enable further heat and mass transfer optimization (e.g., changing the relative angle between the flow and 3D printing directions or multipiece printing with posterior assembly). Additionally, controlled in situ drying, gelation, or photocuring could substantially contribute to the structural and geometric possibilities accessible through MEX methods.

Beyond extrusion-based AM, alternative structuring approaches have been widely explored to optimize catalyst performance through advanced control of heat and mass transfer. Microchannel reactors, also known as microreactors, have been increasingly applied in catalysis because their microstructured channels enable efficient heterogeneous catalysis by reducing mass transfer limitations and ensuring uniform temperature profiles, which is especially important in highly exothermic reactions.[420,421] Various manufacturing methods have been developed to form microstructured reactors, including lithography, selective chemical vapor deposition, laser machining, and more recently, AM.[422,423]

Monolithic foams and aerogels represent another important class of catalytic supports. These highly porous, structured materials combine large surface areas with efficient flow and thermal properties that boost both activity and selectivity.[424–426] Monolithic foams are typically produced from ceramics, metals, or carbon via replica templating, freeze casting, direct foaming, powder sintering or preforming with a temporary pore forming agent, which yield mechanically robust structures with controlled pore size and low pressure drop.[427–429] Aerogels, in contrast, are commonly synthesized via sol–gel chemistry followed by supercritical or ambient-pressure drying, producing ultralight materials with extremely high surface area but lower mechanical strength.[430] Both classes of materials can be functionalized with nanoparticles or active phases to further enhance catalytic performance. These structural and chemical advantages enable applications in selective oxidation, hydrogenation, biomass conversion, and environmental catalysis, where improved reactant accessibility, thermal management, and catalytic efficiency are critical.

Finally, **catalytic membranes** have emerged as multifunctional platforms that integrate catalytic activity with selective

separation in a single unit operation. Constructed from polymers, ceramics, or mixed-matrix composites, these membranes embed catalysts via immobilization, coating, or in situ synthesis, allowing precise tailoring of both active site distribution and transport properties.[431] They can be fabricated from polymers, ceramics, or mixed-matrix composites, with catalysts incorporated via immobilization, coating, or in situ synthesis, allowing precise control over active sites and transport properties.[432] Such systems are particularly suited for hydrogen production, selective oxidations, biomass valorization, and other catalytic processes where coupling reaction and separation reduces equilibrium limitations, enhances energy efficiency, and facilitates continuous operation.

5.2. Machine Learning and Artificial Intelligence

The design and discovery of efficient catalytic materials are fundamental to advancing chemical transformations in industrial processes, renewable energy applications, and environmental remediation. Traditionally, catalyst development has followed empirical and mechanistic pathways involving iterative synthesis, testing, and optimization cycles. However, these approaches are time-intensive and limited in scope. With the advent of artificial intelligence (AI) and ML, the field has undergone a transformative shift, enabling data-driven design and rapid screening of catalysts. These methods facilitate the prediction of optimal catalyst shapes, compositions, and reactivity by learning from high-dimensional experimental and computational data.[433–435]

Moreover, the recent developments in openly accessible, chemically rich material databases have significantly advanced the implementation of data-driven strategies in computational catalysis. Notably, bulk materials repositories, such as the Materials Project, have been instrumental in training advanced ML potential models, including CHGNet and M3GNet.[436–438] In parallel, initiatives (e.g., the Open Catalyst Project) have provided extensive ab initio datasets focused on catalytic surface reactions, supporting the development of highly generalizable models for surface energetics.[439,440] The increasing availability of high-quality computational data has permitted integrating multisource datasets and data fusion frameworks, enhancing the performance and cross-domain transferability of ML potential models. These surrogate models are widely employed in descriptor-based catalyst screening to accelerate the identification of promising candidates, often combined with active learning algorithms.[441,442] This hybrid approach reduces the computational cost of traditional density functional theory (DFT) simulations and efficiently optimizes complex catalytic surface structures across broad chemical spaces.

5.2.1. Data-Driven Design

The data-driven design applies extensive datasets derived from experiments, simulations, and curated databases to train ML models capable of predicting catalytic activity, selectivity, and stability based on structural and compositional descriptors. This approach enables researchers to streamline the discovery process by prioritizing the most promising catalyst candidates, reducing the need for exhaustive experimental screening.[443] The selection of suitable ML algorithms for catalyst property prediction is governed primarily by the distribution and size of the training dataset. In many catalytic studies, the limited availability of high-quality data (attributable to the high computational or experimental cost of generating each data point) represents a significant constraint in model development. Therefore, researchers often rely on narrowly focused, application-specific datasets, where catalysts display constrained compositional variability and structurally analogous active sites.[444] In such datasets, physicochemical descriptors, including surface energy, atomic radius, and electron affinity, are commonly employed as input features for ML model training.[445,446] A variety of regression algorithms, such as ridge regression,[447] decision tree regression,[448] polynomial regression,[449] artificial neural networks (ANNs),[450] and Gaussian process regression, have been explored for this purpose.[451] The performance of these models is typically assessed using independent validation sets, with accuracy, generalizability, and computational efficiency as crucial evaluation criteria.

In heterogeneous catalysis, data are often generated under continuous operational conditions, allowing for the controlled variation of a limited number of process parameters. This setup facilitates the efficient generation of large, high-quality datasets. Thus, the field of heterogeneous catalysis has amassed a significantly more extensive body of data and literature than its homogeneous counterpart.[452,453] Xin et al.[454] demonstrated a compelling application of this strategy, proposing an integrated ML framework designed to screen bimetallic catalysts rapidly for CH_3OH electro-oxidation. The model uses adsorption energies of *CO and *OH species on {111}-terminated metal surfaces, alongside fingerprint descriptors of active sites, as input and output parameters. These values were obtained using DFT calculations. By training ML models on approximately 1,000 idealized bimetallic surfaces, they achieved strong predictive performance, navigating the vast compositional landscape of bimetallic catalysts. Each stable low-index facet of a bimetallic crystal can host hundreds of potential active sites.

Similarly, Nørskov et al.[455] introduced an innovative ML strategy employing neural network potentials to model the surface behavior of Ni–gallium (Ga) bimetallic catalysts for the electrochemical reduction of CO_2. This approach significantly reduced the computational demand, achieving accurate activity predictions with fewer explicit DFT calculations by an order of magnitude. The ML-driven analysis identified the most effective active site motifs as isolated Ni atoms embedded in a Ga matrix, consistent with recent experimental findings highlighting the catalytic efficiency of Ni–Ga systems.

In a notable advancement, Jinnouchi and Asahi[456] employed an ML approach based on Bayesian linear regression to investigate the direct decomposition of nitric oxide (NO) on Rh–Au alloy nanoparticles. The model incorporated a local similarity kernel that enabled the analysis of catalytic

behavior as a function of the local atomic environment. This method demonstrated high efficiency in predicting the adsorption energy of atomic and molecular species on nanoparticle surfaces and the formation energy of the nanoparticles. The model was trained using DFT data derived from single-crystal systems, allowing it to generalize effectively to more complex nanoscale structures.

Furthermore, catalyst shaping through processes (e.g., extrusion and granulation) is a critical engineering step that bridges laboratory-scale catalyst synthesis and industrial reactor performance. This approach directly influences parameters, including surface area, porosity, mechanical strength, and mass transfer characteristics, collectively influencing catalytic efficiency and durability under operational conditions.[14] Extrusion and granulation enable the formation of structured catalyst bodies, such as pellets, monoliths, or extrudates, optimized for specific reactor configurations. However, traditional trial-and-error shaping approaches are time-consuming and often fail to capture the complex relationships between formulation, processing conditions, and resulting catalyst properties.

Recent advancements in AI and ML have transformed this space by enabling predictive modeling and process optimization. For instance, AI algorithms can analyze high-dimensional datasets covering rheological behavior, formulation parameters, and process settings to predict extrusion outcomes (e.g., shape fidelity, mechanical strength, and pore architecture).[457] Furthermore, ML models trained on historical process data can guide the real-time control of extrusion variables to guarantee consistent catalyst quality, minimizing waste and improving scalability.[458] These data-driven approaches have significant promise for accelerating the development of mechanically robust and highly active catalysts for specific industrial applications.

Building on this foundation, catalyst shaping represents a critical engineering stage that bridges laboratory-scale powders with industrial-scale reactor implementation. Traditional methods such as extrusion, pelletizing, granulation, and spray-drying strongly affect catalyst performance by dictating surface area, porosity, tortuosity, mechanical strength, and reactor hydrodynamics. Recent advances in AI and ML have begun to unravel these complex interdependencies, offering predictive capabilities that replace the conventional trial-and-error approach. For example, ANNs have been applied to model extrusion pressures and mechanical strength as a function of formulation variables,[459] while digital twin regression frameworks can forecast throughput and ensure process consistency in real-time.[460] Similarly, Gaussian process regression (GPR) and Bayesian optimization have proven effective in optimizing shaping conditions across multi-fidelity simulations.[461] Moreover, physics-informed neural networks (PINNs) are now being deployed to predict microstructural evolution, including porosity and defect formation, thereby linking shaping conditions to transport phenomena.[462] The comparative applications of these ML approaches across shaping methods are systematically summarized in Table 5, which highlights their utility in extrusion, granulation, and pelletizing.

5.2.2. Accelerating Process Optimization

Traditional methods, such as extrusion and granulation, are often highly complex due to multiscale variables, such as binder content, paste rheology, mixture viscosity, and drying conditions.[467–470] Moreover, ML and AI are increasingly used to model, simulate, and optimize catalyst-shaping processes across all stages, from formulation to final morphology, to address these challenges.[465,471–473]

In extrusion-based catalyst shaping, AI integration has demonstrated significant potential in optimizing various aspects of the extrusion process. Traditional optimization approaches heavily rely on trial-and-error methods to identify suitable process parameters, such as the screw configuration and die geometry, that would yield desirable outcomes.[474] However, these methods are often time-consuming and inadequate for managing the complexity of modern, high-dimensional systems. Recent advances have introduced data-driven frameworks with inverse classification methods to overcome these limitations.

One such method involves inverting a neural network classifier and incorporating a stacked autoencoder and softmax layer to predict optimal process parameters based on the target output properties. Unlike conventional grid search techniques, which become computationally intractable with increasing dimensionality, this AI-driven method permits the rapid and efficient identification of process settings. Moreover, this method requires only a single simulation set to construct the database and can be applied to existing datasets, enhancing scalability and adaptability in extrusion modeling.[475]

Granulation processes are complex and governed by dynamic mechanisms, such as nucleation, growth, aggregation, and breakage.[148,476] Traditionally, the population balance model (PBM) has served as the principal mathematical framework for describing the evolution of particle-size distributions over time. However, solving PBMs typically requires simplifying assumptions that can limit their accuracy and applicability, particularly under variable process conditions.[477–479] Recent research has increasingly focused on integrating AI techniques to enhance the predictive capability of traditional PBMs to address the limitations of traditional PBMs.

One promising direction involves the development of hybrid modeling frameworks combining PBMs with data-driven approaches, such as ML, to refine model parameters dynamically based on experimental or simulated data.[480] A novel approach known as PINNs has gained traction in the scientific ML community due to its ability to solve partial differential equations, including those governing PBMs. PINNs embed physical laws directly into the neural network architecture, allowing for the approximation of PBM solutions while maintaining consistency with the underlying physical principles.[481] This method offers a robust alternative to traditional numerical solvers by simultaneously learning the solution of the PBM and preserving its physical constraints, enabling more accurate and computationally efficient simulations of granulation processes under a broad range of operating conditions.

In parallel, purely data-driven modeling approaches have gained traction as viable alternatives to physics-based mod-

Table 5. Machine learning and simulation techniques applied to catalyst shaping.

Shaping Method	Technique	Target Application	Ref.
Extrusion	Artificial Neural Networks (ANN) (e.g. MLP, RBFNN, CNN, RNN)	Predict extrusion pressure and uniaxial compressive strength	[459,463,464]
Extrusion	Machine Learning Regression (Digital Twin)	Predict throughput and process behavior in extrusion systems	[460]
Granulation	Artificial Neural Network (ANN)	Predict granule size distribution in twin-screw granulation	[465]
Pellet Geometry Design	Neural Network Parameterization	Optimize extruder mixing element geometry using generative parameterization	[466]
Shaping Process Optimization	Deep Gaussian Process (DGP) with Bayesian Optimization	Multi-fidelity optimization of reactor or process simulations	[461]
Additive Manufacturing (AM)	Physics-Informed CNN (PI-CNN)	In situ porosity prediction in metal AM	[462]

The multilayer perceptron (MLP); the radial basis function neural network (RBFNN), the convolutional neural network (CNN), the Kohonen network, and the recurrent neural network (RNN).

els. These methods establish functional relationships between input variables and process outputs without explicitly deriving governing equations.[482] Linear regression techniques have been employed to predict granule properties and optimize input parameters;[483,484] however, their capacity to model nonlinear interactions and complex dependencies among process variables remains limited. More advanced AI methods (e.g., ANNs and fuzzy logic systems) have been investigated because they can capture intricate input–output dynamics and facilitate accurate process scale-up to overcome these constraints.[485,486] When employed independently or in conjunction with PBMs, these AI-enhanced approaches can improve process control, optimize granule quality, and accelerate robust granulation strategy development.

6. Conclusions

The advancement of catalyst-shaping technology has been pivotal in bridging the gap between laboratory-scale catalyst discovery and industrial-scale application. This review thoroughly explores the historical development, current state, and emerging future of catalyst-shaping methods, focusing on how these techniques address the evolving demands of modern catalytic processes. Shaping is no longer considered a peripheral step in catalyst preparation. Still, it is a core element of catalyst engineering, directly influencing critical performance metrics, such as activity, selectivity, and long-term stability.

Traditional shaping techniques (e.g., pelletizing, granulation, and extrusion) have laid the groundwork for industrial catalyst manufacturing. Although these methods offer essential benefits in handling, mechanical strength, and compatibility with specific reactor configurations, they also have limitations, particularly regarding textural uniformity, porosity, and active site accessibility. Modern extrusion technology, particularly screw and ram extrusion, has evolved to address these challenges, offering better control over shape, porosity, and mechanical properties. However, the performance of extruded catalysts remains sensitive to paste rheology, extrusion speed, temperature, and formulation variables, such as binder type and liquid-to-solid ratios, highlighting the need for continuous optimization.

Spray-drying has emerged as a versatile multiscale shaping method, producing spherical particles with tailored size, porosity, and morphology. Spray-drying is especially well-suited for shaping catalysts in fixed- and fluidized-bed reactors. Integrating atomization control, drying kinetics, and precursor chemistry has enabled spray-drying to transition from a batch-based process to a continuous, scalable solution for advanced catalyst manufacturing. Moreover, its compatibility with modern modeling approaches, such as CFD and reaction engineering, has enabled predictive design and optimization, reduced development time, and enhanced reproducibility.

Similarly, fluidized-bed spray granulation has gained significant traction as a shaping method that ensures robust particle formation and allows for layering, coating, and controlled particle growth. The technique is valuable in applications requiring enhanced thermal and mechanical stability, such as FCC and environmental catalysis. The reactor configuration, nozzle design, and operating conditions (e.g., the spray rate, airflow, and temperature) contribute to the final granule properties, and recent advances have facilitated its transition to continuous operation for large-scale production.

Throughout the review, the importance of multiscale catalyst design is emphasized. Each level is critical in determining the final catalyst performance from nanoscale active site configuration and mesoscale porosity to macroscale particle shaping and reactor integration. The central challenge remains to translate highly active powder catalysts into mechanically durable, thermally stable, and mass-transfer-optimized shaped bodies. Prop-

erly engineered catalyst shapes can mitigate pressure decreases, improve heat and mass transfer, and reduce channeling or attrition, depending on the reactor type.

Applying the catalyst design triangle and balancing mechanical, chemical–physical, and catalytic properties remains crucial in shaping development. The interplay of binders, plasticizers, and active components must be carefully managed to preserve catalytic functionality while enhancing mechanical robustness. The review also highlights the influence of shaping techniques on catalyst acidity, porosity, and thermal conductivity, which are critical in industrial settings where long-term operation and regeneration cycles are essential.

Integrating ML, process modeling, and AM represents a transformative opportunity in catalyst shaping. Digitalization enables the rapid optimization of shaping parameters, formulation screening, and defect prediction, and AM offers new directions for highly customized catalyst architectures. Together, these innovations push the boundaries of catalyst design toward greater precision, sustainability, and reactor-specific performance.

In conclusion, catalyst shaping is no longer merely a scaling-up step but is a central pillar of catalyst design and optimization. By employing multiscale engineering principles, advanced manufacturing methods, and digital tools, the next generation of shaped catalysts can be better equipped to meet the demands of sustainable, high-efficiency chemical processes across diverse industrial sectors.

Nomenclature

A	Surface area of the droplet or particle, m^2
Bo	Bond number based on the internal nozzle diameter
Bo_0	Bond number based on the external nozzle diameter (orifice)
D	Diameter of the extrusion channel, m
D_0	Diameter of the barrel, m
D_d	Droplet diameter based on the nozzle type, m
d_d	Diameter of the droplet, m
d_0	Diameter of the orifice or capillary, m
g	Acceleration of gravity, m/s^2
h_m	Convective mass transfer coefficient, $kg/m^2{\cdot}s$
K	Clanet and Lasheras model constant
K_f	Equipment constant (related to the atomizer type)
L	Length of the extrusion channel, m
m	Mass of the droplet or particle, kg
n	Exponent related to the effect of the liquid flow rate
P	Generated pressure during extrusion, Pa
Q	Liquid flow rate, m^3/s
ρ	Density of the liquid, kg/m^3
$\rho_{v,b}$	Bulk vapor concentration, kg/m^3
$\rho_{v,s}$	Vapor concentration at the particle–gas interface, kg/m^3
t	Time, s
v	Mean extrudate velocity, m/s
We_c	Critical Weber number
a	Empirical exponents for the droplet size
b	Empirical exponents for the droplet size
c	Empirical exponents for the droplet size
α	Velocity factor of the bulk yield stress, Pa·s/m
α_e	Velocity factor of the bulk yield stress, Pa·s/m
β	Velocity factor of the wall shear stress, Pa·s/m
σ	Surface tension, N/m
σ_0	Initial bulk yield stress of the paste, Pa
τ_0	Initial wall shear stress of the paste, Pa
μ	Dynamic viscosity, Pa·s
φ	Thiele modulus
η	effectiveness factor

Acknowledgments

This work was conducted with the financial support of the King Abdullah University of Science and Technology (KAUST, BAS/1/1403). The authors thank Jose Valecillos for his support in making some of the graphical material.

Conflict of Interests

The authors declare no conflict of interest.

Keywords: Catalyst manufacturing · Industrial catalysis · Shaping · Technical catalyst

[1] J. J. Bravo-Suárez, R. V Chaudhari, B. Subramaniam, *Nov. Mater. Catal. Fuels Process*, Vol. *1132*, ACS Symposium Series, Washington, DC **2013** pp. 3–68.
[2] P. T. Anastas, M. M. Kirchhoff, T. C. Williamson, *Appl. Catal. A Gen.* **2001**, *221*, 3–13.
[3] Industrial Catalyst Market: Global Industry Trends, Share, Size, Growth, Opportunity and Forecast 2022–2027, **2022**.
[4] W. N. R. W. Isahak, A. Al-Amiery, *Green Technol. Sustain.* **2024**, *2*, 100078.
[5] D. Wu, J. Zhou, Y. Li, *AIChE J.* **2007**, *53*, 2618–2629.
[6] J. Hagen, *Industrial Catalysis: A Practical Approach*, John Wiley & Sons, Weinheim, Germany **2015**.
[7] G. T. Whiting, S.-H. Chung, D. Stosic, A. D. Chowdhury, L. I. van der Wal, D. Fu, J. Zecevic, A. Travert, K. Houben, M. Baldus, B. M. Weckhuysen, *ACS Catal.* **2019**, *9*, 4792–4803.
[8] J. C. Kim, J. Lee, S. W. Han, H. Park, H. Park, J. Y. Park, R. Ryoo, *Microporous Mesoporous Mater.* **2023**, *357*, 112610.
[9] T. Shoinkhorova, A. Dikhtiarenko, A. Ramirez, A. Dutta Chowdhury, M. Caglayan, J. Vittenet, A. Bendjeriou-Sedjerari, O. S. Ali, I. Morales-Osorio, W. Xu, J. Gascon, *ACS Appl. Mater. Interfaces* **2019**, *11*, 44133–44143.
[10] P. Bachmann, K. Chen, A. Bück, E. Tsotsas, *Particuology* **2020**, *50*, 1–12.
[11] J. Y. Lee, J. An, C. K. Chua, *Appl. Mater. Today* **2017**, *7*, 120–133.
[12] S. Devyatkov, N. Kuzichkin, D. Murzin, *Chim. Oggi* **2015**, *33*, 57–64.
[13] C. Perego, P. Villa, *Catal. Today* **1997**, *34*, 281–305.
[14] C. H. Bartholomew, R. J. Farrauto, *Fundamentals of Industrial Catalytic Processes*, John Wiley & Sons, Ltd, Weinheim, Germany **2005**.
[15] V. G. Baldovino-Medrano, C. Alcázar, M. T. Colomer, R. Moreno, E. M. Gaigneaux, *Appl. Catal. A Gen.* **2013**, *468*, 190–203.
[16] A. B. D. Nandiyanto, K. Okuyama, *Adv. Powder Technol.* **2011**, *22*, 1–19.
[17] A. B. D. Nandiyanto, T. Ogi, W.-N. Wang, L. Gradon, K. Okuyama, *Adv. Powder Technol.* **2019**, *30*, 2908–2924.
[18] V. Truong, B. R. Bhandari, T. Howes, *J. Food Eng.* **2005**, *71*, 55–65.
[19] C. Su, J. C. Wang, C.-Y. Chen, K. Chu, C.-K. Lin, *Materials (Basel).* **2019**, *12*, 706.
[20] L. L. Messa, C. F. Souza, R. Faez, *Polym. Test.* **2020**, *81*, 106196.
[21] N. Hampel, A. Bück, M. Peglow, E. Tsotsas, *Chem. Eng. Sci.* **2013**, *86*, 87–98.
[22] K. Sarabandi, P. Gharehbeglou, S. M. Jafari, *Dry. Technol.* **2020**, *38*, 577–595.

[23] J. R. Rostrup-Nielsen, T. S. Christensen, I. Dybkjaer, in *Stud. Surf. Sci. Catal.* (Eds: T. S. R. P. Rao, G. M. Dhar), Elsevier, Amsterdam, the Netherlands **1998**, pp. 81–95.
[24] S. Wang, T. Langrish, *Food Res. Int.* **2009**, *42*, 13–25.
[25] M. Schmidt, T. Hoffmann, A. Bück, E. Tsotsas, *Procedia Eng.* **2015**, *102*, 565–574.
[26] R. Boerefijn, M. J. Hounslow, *Chem. Eng. Sci.* **2005**, *60*, 3879–3890.
[27] S. Palzer, in *Granulation* (Eds: A. D. Salman, M. J. Hounslow, J. P. K. Seville), Elsevier Science B.V., Amsterdam, the Netherlands **2007**, pp. 591–671.
[28] J. Perregaard, Shaping tomorrow's catalysts with today's technology, https://chemical-catalysts-and-adsorbents.basf.com/global/en/sustainability-process-catalysts/X3D, **n.d.**
[29] J. Meeuwissen, L. van Haande, Unique catalyst designs enabled by 3D printing, https://www.shell.com/what-we-do/digitalisation/3d-printing/unique-catalyst-designs-enabled-by-3d-printing.html, **2023**.
[30] Dirk Vangeneuden, Make chemical processes more efficient with 3D-printed catalysts, https://vito.be/en/applications/3d-printed-catalysts, **n.d.**
[31] C. K. Chua, S. M. Chou, T. S. Wong, *Int. J. Adv. Manuf. Technol.* **1998**, *14*, 146–152.
[32] N. Shahrubudin, T. C. Lee, R. Ramlan, *Procedia Manuf.* **2019**, *35*, 1286–1296.
[33] L. Chen, S. Zhou, M. Li, F. Mo, S. Yu, J. Wei, *Catalysts* **2022**, *12*, 1081.
[34] L. Liu, A. Corma, *Nat. Rev. Chem.* **2021**, *5*, 256–276.
[35] Y. Liu, E. Lotero, J. G. Goodwin, *J. Mol. Catal. A Chem.* **2006**, *245*, 132–140.
[36] Z. Khan, F. Javed, Z. Shamair, A. Hafeez, T. Fazal, A. Aslam, W. B. Zimmerman, F. Rehman, *J. Ind. Eng. Chem.* **2021**, *103*, 80–101.
[37] D. Stratiev, I. Shishkova, M. Ivanov, R. Dinkov, B. Georgiev, G. Argirov, V. Atanassova, P. Vassilev, K. Atanassov, D. Yordanov, A. Popov, A. Padovani, U. Hartmann, S. Brandt, S. Nenov, S. Sotirov, E. Sotirova, *ACS Omega* **2021**, *6*, 7626–7637.
[38] L. Zhang, Q. Hu, Y. Qin, H. Liu, H. Liu, G. Cao, X. Gao, L. Song, Z. Sun, *Microporous Mesoporous Mater.* **2023**, *359*, 112627.
[39] R. A. Sheldon, J. M. Woodley, *Chem. Rev.* **2018**, *118*, 801–838.
[40] S. Singh, P. Kumar Sharma, S. Chaturvedi, P. Kumar, A. Deepak Nannaware, A. Kalra, P. Kumar Rout, *Food Chem.* **2024**, *435*, 137217.
[41] M. K. Debe, *Nature* **2012**, *486*, 43–51.
[42] J. García-Serna, R. Piñero-Hernanz, D. Durán-Martín, *Catal. Today* **2022**, *387*, 237–243.
[43] M. Gao, G. Zhang, L. Zhao, J. Gao, C. Xu, *Ind. Eng. Chem. Res.* **2023**, *62*, 1215–1226.
[44] Q. Wu, *Fuel* **2023**, *332*, 126132.
[45] M. S. Akhtar, S. Ali, W. Zaman, *Catalysts* **2024**, *14*, 841.
[46] H. Li, M. Li, H. Nie, *Microporous Mesoporous Mater.* **2014**, *188*, 30–36.
[47] A. Tanimu, K. Alhooshani, *Energy & Fuels* **2019**, *33*, 2810–2838.
[48] M. Hattori, N. Okuyama, H. Kurosawa, M. Hara, *J. Am. Chem. Soc.* **2023**, *145*, 7888–7897.
[49] G. Pacchioni, *ACS Catal.* **2024**, *14*, 2730–2745.
[50] M. Zabilskiy, V. L. Sushkevich, M. A. Newton, J. A. van Bokhoven, *ACS Catal.* **2020**, *10*, 14240–14244.
[51] M. H. Morcali, *Resour. Conserv. Recycl.* **2020**, *159*, 104891.
[52] H. Tang, Z. Peng, R. Tian, L. Ye, J. Zhang, M. Rao, G. Li, *J. Environ. Chem. Eng.* **2023**, *11*, 110237.
[53] D. Chen, Y. Cheng, N. Zhou, P. Chen, Y. Wang, K. Li, S. Huo, P. Cheng, P. Peng, R. Zhang, L. Wang, H. Liu, Y. Liu, R. Ruan, *J. Clean. Prod.* **2020**, *268*, 121725.
[54] S. Wang, Z. Shen, A. Osatiashtiani, S. A. Nabavi, P. T. Clough, *Chem. Eng. J.* **2024**, *486*, 150170.
[55] A. M. Alkadhem, F. Tavares, N. Realpe, G. Lezcano, A. Yudhanto, M. Subah, V. Manaças, J. Osinski, G. Lubineau, P. Castaño, *Fuel* **2023**, *349*, 128717.
[56] A. Kazemi, M. A. Pordsari, M. Tamtaji, F. Zainali, S. Keshavarz, H. Baesmat, F. Manteghi, A. Ghaemi, S. Rohani, W. A. Goddard III, *Sep. Purif. Technol.* **2025**, *361*, 131328.
[57] A. M. Alkadhem, M. A. A. Elgzoly, S. A. Onaizi, *J. Environ. Chem. Eng.* **2020**, *8*, 103968.
[58] A. M. Alkadhem, M. A. A. Elgzoly, A. Alshami, S. A. Onaizi, *Colloids Surfaces A Physicochem. Eng. Asp.* **2021**, *616*, 126258.
[59] E. Arici, B. Y. Kaplan, A. M. Mert, S. Alkan Gursel, S. Kinayyigit, *Int. J. Hydrogen Energy* **2019**, *44*, 14175–14183.
[60] S. Mitchell, N. L. Michels, J. Pérez-Ramírez, *Chem. Soc. Rev.* **2013**, *42*, 6094.
[61] M. Y. Tsang, A. Sinelshchikova, O. Zaremba, F. Schöfbeck, A. D. Balsa, M. R. Reithofer, S. Wuttke, J. M. Chin, *Adv. Funct. Mater.* **2024**, *34*, 2308376.
[62] C. Ortega, D. Otyuskaya, E.-J. Ras, L. D. Virla, G. S. Patience, H. Dathe, *Can. J. Chem. Eng.* **2021**, *99*, 1288–1306.
[63] F. Akhtar, L. Andersson, S. Ogunwumi, N. Hedin, L. Bergström, *J. Eur. Ceram. Soc.* **2014**, *34*, 1643–1666.
[64] I. Melián-Cabrera, *Ind. Eng. Chem. Res.* **2021**, *60*, 18545–18559.
[65] A. Wang, J. Li, T. Zhang, *Nat. Rev. Chem.* **2018**, *2*, 65–81.
[66] X. Zeng, S. Shahgaldi, S. K. Mitra, X. Li, *Energy Convers. Manag.* **2025**, *326*, 119496.
[67] S. Li, H. Yang, S. Wang, M. Dong, J. Wang, W. Fan, *Microporous Mesoporous Mater.* **2022**, *329*, 111538.
[68] B. Li, Z. Hu, B. Kong, J. Wang, W. Li, Z. Sun, X. Qian, Y. Yang, W. Shen, H. Xu, D. Zhao, *Chem. Sci.* **2014**, *5*, 1565.
[69] M. Hartmann, M. Thommes, W. Schwieger, *Adv. Mater. Interfaces* **2021**, *8*, 2001841.
[70] S. M. Rao, E. Saraçi, R. Gläser, M.-O. Coppens, *Chem. Eng. J.* **2017**, *329*, 45–55.
[71] A. Kumari, K. Singh, O. Hinrichsen, V. V Buwa, *Chem. Eng. J.* **2025**, *510*, 161695.
[72] A. Tripodi, F. Conte, I. Rossetti, *Ind. Eng. Chem. Res.* **2021**, *60*, 908–915.
[73] A. Shamiri, N. Aliabadi, *Chem. Eng. J. Adv.* **2021**, *8*, 100177.
[74] M. Salciccioli, M. Stamatakis, S. Caratzoulas, D. G. Vlachos, *Chem. Eng. Sci.* **2011**, *66*, 4319–4355.
[75] S. Li, in *React. Eng.* (Ed.: S. Li), Butterworth-Heinemann, Boston **2017**, pp. 265–310.
[76] A. Morgado Lopes, V. Wernert, L. Sorbier, V. Lecocq, M. Antoni, R. Denoyel, *Microporous Mesoporous Mater.* **2021**, *310*, 110640.
[77] J. M. P. Q. Delgado, *Heat Mass Transf.* **2006**, *42*, 279–310.
[78] Z. Guo, Z. Sun, N. Zhang, M. Ding, J. Wen, *Chem. Eng. Sci.* **2017**, *173*, 578–587.
[79] K. C. Metaxas, N. G. Papayannakos, *Chem. Eng. J.* **2008**, *140*, 352–357.
[80] B. Kraushaar-Czarnetzki, S. P. Müller, in *Synth. Solid Catal.*, John Wiley & Sons, Ltd, New Jersey, USA **2009**, pp. 173–199.
[81] Jan Písecký, *Handbook of Milk Powder Manufacture*, Niro A/S, Copenhagen, Denmark, **1997**.
[82] P. Mäki-Arvela, I. Simakova, Z. Vajglová, N. Kumar, D. Y. Murzin, *Catal. Today* **2023**, *423*, 113933.
[83] M. Absi-Halabi, A. Stanislaus, H. Al-Zaid, *Appl. Catal. A Gen.* **1993**, *101*, 117–128.
[84] J. Gálvez, J. P. Correa Aguirre, M. A. Hidalgo Salazar, B. Vera Mondragón, E. Wagner, C. Caicedo, *Polymers (Basel)*. **2020**, *12*, 92111.
[85] S. P. Verkleij, G. T. Whiting, S. P. Esclapez, M. M. Mertens, A.-J. Bons, M. Burgers, B. M. Weckhuysen, *Catal. Sci. Technol.* **2018**, *8*, 2175–2185.
[86] Z. Vajglová, N. Kumar, P. Mäki-Arvela, K. Eränen, M. Peurla, L. Hupa, D. Y. Murzin, *Org. Process Res. Dev.* **2019**, *23*, 2456–2463.
[87] S. Mitchell, N. L. Michels, K. Kunze, J. Pérez-Ramírez, *Nat. Chem.* **2012**, *4*, 825–831.
[88] Y. J. Lee, Y. W. Kim, N. Viswanadham, K. W. Jun, J. W. Bae, *Appl. Catal. A Gen.* **2010**, *374*, 18–25.
[89] N. L. Michels, S. Mitchell, J. Pérez-Ramírez, *ACS Catal.* **2014**, *4*, 2409–2417.
[90] K. Yang, D. Zhang, M. Zou, L. Yu, S. Huang, *ChemCatChem* **2021**, *13*, 1414–1423.
[91] A. M. Alkadhem, H. O. Mohamed, T. Hoffmann, J. Fan, V. E. Musteata, S. C. Ogg, J. Ruiz-Martinez, E. Tsotsas, P. Castaño, *Chem. Eng. J.* **2025**, *509*, 161126.
[92] S. Afandizadeh, E. A. Foumeny, *Appl. Therm. Eng.* **2001**, *21*, 669–682.
[93] J. Hagen, in *Ind. Catal.*, John Wiley & Sons, Ltd, New Jersey, USA **2015**, pp. 211–238
[94] G. Eigenberger, W. Ruppel, in *Ullmann's Encycl. Ind. Chem.*, John Wiley & Sons, Ltd, New Jersey, USA **2012**.
[95] J. Xu, G. F. Froment, *AIChE J.* **1989**, *35*, 88–96.
[96] D. Nemec, J. Levec, *Chem. Eng. Sci.* **2005**, *60*, 6947–6957.
[97] E. A. Foumeny, F. Benyahia, *Heat Recover. Syst. CHP* **1991**, *11*, 127–130.
[98] E. A. Foumeny, S. Roshani, *Chem. Eng. Sci.* **1991**, *46*, 2363–2364.
[99] Y. Duan, M. Xu, X. Zhou, X. Huai, *Particuology* **2014**, *17*, 125–130.
[100] V. Tukač, J. Hanika, *Chem. Eng. Sci.* **1992**, *47*, 2227–2232.

[101] H. L. Huynh, W. M. Tucho, Q. Shen, Z. Yu, *Chem. Eng. J.* **2022**, *428*, 131106.
[102] M. Liao, Y. Chen, Z. Cheng, C. Wang, X. Luo, E. Bu, Z. Jiang, B. Liang, R. Shu, Q. Song, *Appl. Energy* **2019**, *252*, 113435.
[103] J. Kim, L. H. Park, J.-M. Ha, E. D. Park, *Catalysts* **2019**, *9*, 363.
[104] A. R. de la Osa, A. De Lucas, J. Díaz-Maroto, A. Romero, J. L. Valverde, P. Sánchez., *Catal. Today* **2012**, *187*, 173–182.
[105] S. R. Vatcha, *Colloids Surfaces A Physicochem. Eng. Asp.* **1998**, *133*, 99–105.
[106] S. R. Kulkarni, V. K. Velisoju, F. Tavares, A. Dikhtiarenko, J. Gascon, P. Castaño, *Catal. Rev. – Sci. Eng.* **2022**, *65*, 174–237, https://doi.org/10.1080/01614940.2022.2025670.
[107] M. Hettel, C. Antinori, O. Deutschmann, *Emiss. Control Sci. Technol.* **2016**, *2*, 188–203.
[108] A. M. Gänzler, M. Casapu, D. E. Doronkin, F. Maurer, P. Lott, P. Glatzel, M. Votsmeier, O. Deutschmann, J.-D. Grunwaldt, *J. Phys. Chem. Lett.* **2019**, *10*, 7698–7705.
[109] H. T. Bi, N. Ellis, I. A. Abba, J. R. Grace, *Chem. Eng. Sci.* **2000**, *55*, 4789–4825.
[110] K. Muroyama, L.-S. Fan, *AIChE J.* **1985**, *31*, 1–34.
[111] C. R. Bemrose, J. Bridgwater, *Powder Technol.* **1987**, *49*, 97–126.
[112] D. Wu, Z. Gu, Y. Li, *Chem. Eng. Sci.* **2015**, *135*, 431–440.
[113] L. F. Acevedo-Córdoba, O. J. Vargas-Montañez, E. A. Velasco-Rozo, I. D. Mora-Vergara, J. N. Díaz de León, D. Pérez-Martínez, E. M. Morales-Valencia, V. G. Baldovino-Medrano, *Catal. Today* **2024**, *429*, 114474.
[114] D. Kunii, O. Levenspiel, *Chem. Eng. Sci.* **1997**, *52*, 2471–2482.
[115] S. Aghamohammadi, M. Haghighi, A. Ebrahimi, *Microporous Mesoporous Mater.* **2019**, *279*, 371–386.
[116] Y. Li, X. Li, L. Chang, D. Wu, Z. Fang, Y. Shi, *Catal. Today* **1999**, *51*, 73–84.
[117] M. Zakeri, A. Samimi, M. S. Afarani, A. Salehirad, *Particuology* **2017**, *32*, 160–166.
[118] C. Couroyer, M. Ghadiri, P. Laval, N. Brunard, F. Kolenda, *Oil & Gas Sci. Technol. L Inst. Fr. Du Pet.* **2000**, *55*, 67–85.
[119] A. N. J. Stevenson, I. M. Hutchings, *J. Mater. Sci. Lett.* **1996**, *15*, 688–690.
[120] S. Kukade, P. Kumar, P. V. C. Rao, N. V Choudary, *Powder Technol.* **2016**, *301*, 472–477.
[121] G. Larsen, *J. Am. Chem. Soc.* **1997**, *119*, 11560.
[122] E. Tronconi, G. Groppi, T. Boger, A. Heibel, *Chem. Eng. Sci.* **2004**, *59*, 4941–4949.
[123] S. Uhlenbruck, F. Tietz, *Mater. Sci. Eng. B* **2004**, *107*, 277–282.
[124] S. Roy, A. Nagel, K. A. Weidenmann, *Thermochim. Acta* **2020**, *684*, 178488.
[125] M. E. Z. Velthoen, A. Lucini Paioni, I. E. Teune, M. Baldus, B. M. Weckhuysen, *Chem. – A Eur. J.* **2020**, *26*, 11995–12009.
[126] Y. Zhang, Y. Zhou, A. Qiu, Y. Wang, Y. Xu, P. Wu, *Ind. Eng. Chem. Res.* **2006**, *45*, 2213–2219.
[127] S. Zhang, Y. Gong, L. Zhang, Y. Liu, T. Dou, J. Xu, F. Deng, *Fuel Process. Technol.* **2015**, *129*, 130–138.
[128] G. A. Somorjai, Y. Li, *Nano Letters* **2010**, *10*, 3409–3413, https://doi.org/10.1021/nl101807g.
[129] D. Y. Murzin, *Engineering Catalysis*, De Gruyter, Berlin, Boston **2020**.
[130] K. Zhang, X. Jiang, M. J. Forte, M. Sun, M. AlAbdullah, M. AlAmer, M. Aljishi, E. AlSayed, W. AlSadat, B. C. Gates, A. Katz, *Catal. Sci. Technol.* **2024**, *14*, 4740–4755.
[131] M. S. Beheshti, M. Behzad, J. Ahmadpour, H. Arabi, *Microporous Mesoporous Mater.* **2020**, *291*, 109699.
[132] X. Du, X. Kong, L. Chen, *Catal. Commun.* **2014**, *45*, 109–113.
[133] J. Freiding, B. Kraushaar-Czarnetzki, *Appl. Catal. A Gen.* **2011**, *391*, 254–260.
[134] M. Campanati, G. Fornasari, A. Vaccari, *Catal. Today* **2003**, *77*, 299–314.
[135] V. G. Baldovino-Medrano, M. T. Le, I. Van Driessche, E. Bruneel, C. Alcázar, M. T. Colomer, R. Moreno, A. Florencie, B. Farin, E. M. Gaigneaux, *Catal. Today* **2015**, *246*, 81–91.
[136] T. A. Nijhuis, A. E. W. Beers, T. Vergunst, I. Hoek, F. Kapteijn, J. A. Moulijn, *Catal. Rev.* **2001**, *43*, 345–380.
[137] S. P. S. Andrew, *Chem. Eng. Sci.* **1981**, *36*, 1431–1445.
[138] L. S. Kershenbaum, *AIChE J.* **1982**, *28*, 173.
[139] K. Galejová, L. Obalová, K. Jirátová, K. Pacultová, F. Kovanda, *Chem. Pap.* **2009**, *63*, 172–179.
[140] V. G. Baldovino-Medrano, B. Farin, E. M. Gaigneaux, *ACS Catal.* **2012**, *2*, 322–336.
[141] V. G. Baldovino-Medrano, B. Kartheuser, E. M. Gaigneaux, *Catal. Today* **2019**, *338*, 81–92.
[142] S. T. Islam, S. K. Samanta, A. K. Lohar, A. Bandyopadhyay, *Mater. Res. Express* **2019**, *6*, 095204.
[143] I. T. Cameron, F. Y. Wang, C. D. Immanuel, F. Stepanek, *Chem. Eng. Sci.* **2005**, *60*, 3723–3750.
[144] A. Szulc, E. Skotnicka, M. K. Gupta, J. B. Królczyk, *Powder Technol.* **2024**, *431*, 119092.
[145] J. Litster, B. Ennis, *The Science and Engineering of Granulation Processes*, Springer Dordrecht, Dordrecht, the Netherlands **2004**.
[146] D. Zapater, S. R. Kulkarni, F. Wery, M. Cui, J. Herguido, M. Menendez, G. J. Heynderickx, K. M. Van Geem, J. Gascon, P. Castaño, *Prog. Energy Combust. Sci.* **2024**, *105*, 101176.
[147] M. A. Doheim, *Powder Technol.* **2022**, *404*, 117512.
[148] S. M. Iveson, J. D. Litster, K. Hapgood, B. J. Ennis, *Powder Technol.* **2001**, *117*, 3–39.
[149] J. Kim, K. C. Song, O. Wilhelm, S. E. Pratsinis, *Chemie Ing. Tech.* **2001**, *73*, 461–468.
[150] H. Leuenberger, M. Lanz, *Adv. Powder Technol.* **2005**, *16*, 3–25.
[151] F. Händle, *The Art of Ceramic Extrusion*, Springer Cham, Cham, Switzerland **2019**.
[152] Z. Vajglová, N. Kumar, P. Mäki-Arvela, K. Eränen, M. Peurla, L. Hupa, M. Nurmi, M. Toivakka, D. Y. Murzin, *Ind. Eng. Chem. Res.* **2019**, *58*, 18084–18096.
[153] Z. Asgar Pour, M. M. Abduljawad, Y. A. Alassmy, L. Cardon, P. H. M. Van Steenberge, K. O. Sebakhy, *Catalysts* **2023**, *13*, 656.
[154] A. Aranzabal, D. Iturbe, M. Romero-Sáez, M. P. González-Marcos, J. R. González-Velasco, J. A. González-Marcos, *Chem. Eng. J.* **2010**, *162*, 415–423.
[155] S. Klisch, D. Gilbert, E. Breaux, A. Dalier, S. Gupta, B. Jakobi, G. J. Schneider, *J. Chem. Educ.* **2024**, *101*, 3292–3300.
[156] B. Yeskendir, J. P. Dacquin, Y. Lorgouilloux, C. Courtois, S. Royer, J. Dhainaut, *Mater. Adv.* **2021**, *2*, 7139–7186.
[157] L. Lakiss, J. P. Gilson, V. Valtchev, S. Mintova, A. Vicente, A. Vimont, R. Bedard, S. Abdo, J. Bricker, *Microporous Mesoporous Mater.* **2020**, *299*, 110114.
[158] A. H. Valekar, K.-H. Cho, U.-H. Lee, J. S. Lee, J. W. Yoon, Y. K. Hwang, S. G. Lee, S. J. Cho, J.-S. Chang, *RSC Adv.* **2017**, *7*, 55767–55777.
[159] A. Santomaso, P. Lazzaro, P. Canu, *Chem. Eng. Sci.* **2003**, *58*, 2857–2874.
[160] N. Rahmanian, M. Ghadiri, X. Jia, F. Stepanek, *Powder Technol.* **2009**, *192*, 184–194.
[161] ASTM International. Standard Test Method for Calcium and Magnesium in Water by EDTA Titration; ASTM D4058-96; ASTM International: West Conshohocken, PA, **1996**.
[162] R. W. Baldwin, Preparation of Catalyst Pellets Having Sustained Hardness and Attrition Resistance, **n.d.**
[163] S. S. Kulkarni, P. H. M. Janssen, B. H. J. Dickhoff, *Powder Technol.* **2023**, *427*, 118694.
[164] M. Zarezadeh-Mehrizi, A. Afshar Ebrahimi, A. Rahimi, *Sci. Iran.* **2018**, *25*, 1434–1439.
[165] J. E. H. Moisés G. Sanchez, Extruded Alumina Catalyst Support Having Controlled Distribution of Pore Sizes, **1981**.
[166] L. Vandevivere, M. Vangampelaere, C. Portier, C. de Backere, O. Häusler, T. De Beer, C. Vervaet, V. Vanhoorne, *Pharmaceutics* **2021**, *13*, 210.
[167] E. Gryczová, K. Kubova Dvorackova, M. Rabiškova, *Ces. a Slov. Farm.* **2009**, *58*, 9–13.
[168] R. T. Shete, B. N. Thorat, P. D. Amin, *Pharm Sci* **2022**, *28*, 459–469.
[169] D. B. Bukur, V. H. Carreto-Vazquez, W. Ma, *Appl. Catal. A Gen.* **2010**, *388*, 240–247.
[170] Beeckman, J. WL, *Catalyst Engineering Technology: Fundamentals and Applications*, John Wiley & Sons, New Yersey, USA **2020**.
[171] T. Mäurer, Investigation of Mass Transport Phenomena in the Conversion of Methanol to Olefins over Technical Alumina/ZSM-5 Catalysts; Dissertation, Karlsruher Institut für Technologie (KIT), Institut für Chemische Verfahrenstechnik (CVT), **2004**.
[172] S. P. Müller, M. Kucher, C. Ohlinger, B. Kraushaar-Czarnetzki, *J. Catal.* **2003**, *218*, 419–426.
[173] D. Wu, M. Tang, *Powder Technol.* **2019**, *352*, 79–90.
[174] A. S. Burbidge, J. Bridgwater, *Chem. Eng. Sci.* **1995**, *50*, 2531–2543.

[175] B. Wan, W. Chen, T. Lu, F. Liu, Z. Jiang, M. Mao, *Resour. Conserv. Recycl.* **2017**, *125*, 37–47.
[176] A. Marnot, K. Koube, S. Jang, J. Kacher, N. Thadhani, B. Brettmann, *Virtual Phys. Prototyp.* **2023**, *18*, e2279149.
[177] J. Benbow, J. Bridgwater, *Paste Flow and Extrusion*, Clarendon Press, Oxford, United Kingdom **1993**.
[178] P. Pitayachaval, T. Baothong, *MATEC Web Conf.* **2018**, *213*, 1013.
[179] Z. Jiang, A. Palacios, B. Zou, Y. Zhao, W. Deng, X. Zhang, Y. Ding, *Renew. Sustain. Energy Rev.* **2022**, *159*, 112134.
[180] A. Duque, P. Manzanares, M. Ballesteros, *Renew. Energy* **2017**, *114*, 1427–1441.
[181] C. Karunanithy, K. Muthukumarappan, *Ind. Crops Prod.* **2011**, *33*, 188–199.
[182] C. Karunanithy, K. Muthukumarappan, in *Green Biomass Pretreatment for Biofuels Production* (Ed: T. Gu), Springer, Netherlands, Dordrecht **2013**, pp. 31–65.
[183] D. Sonaglio, A. O. Beringhs, A. Porfírio, B. Bataille, *Powder Technol*. **2012**, *230*, 54–62.
[184] T. O. Althaus, E. J. Windhab, *Powder Technol*. **2011**, *211*, 10–18.
[185] Onoda, G. Y, Hench, L. L, *Ceramic Processing Before Firing*, Wiley-Interscience, New York, USA **1978**.
[186] D. Ballardini, L. Sighicelli, C. Orsenigo, L. Visconti, E. Tronconi, P. Forzatti, A. Bahamonde, E. Atanes, J. P. Gomez Martin, F. Bregani, in *11th Int. Congr. Catal. –40th Anniv*. (Eds.: J. W. Hightower, W. Nicholas Delgass, E. Iglesia, A. T. Bell), Elsevier, New York, NY, USA **1996**, pp. 1359–1368.
[187] M. Bankmann, R. Brand, B. H. Engler, J. Ohmer, *Catal. Today* **1992**, *14*, 225–242.
[188] J. M. Thomas, *Angew. Chemie Int. Ed.* **2009**, *48*, 3390–3391.
[189] R. J. Kowalski, C. Li, G. M. Ganjyal, *J. Food Eng.* **2018**, *234*, 50–56.
[190] A. Schittny, H. Ogawa, J. Huwyler, M. Puchkov, *Eur. J. Pharm. Biopharm.* **2018**, *132*, 127–145.
[191] R. P. Chhabra, J. F. Richardson, *Non-Newtonian Flow and Applied Rheology*, Elsevier Ltd, Oxford, United Kingdom **2008**.
[192] A. V Borisov, O. I. Aksenova, M. G. Kulikova, G. V Alexeev, K. S. Maslova, *{IOP} Conf. Ser. Earth Environ. Sci.* **2021**, *640*, 072012.
[193] Z. Li, C. Sun, A. Naeem, Q. Li, L. Yang, Z. Jin, Y. Guan, L. Chen, W. Zhu, L. Ming, *Dry. Technol.* **2024**, *42*, 2328–2347.
[194] A. Singh, G. Van den Mooter, *Adv. Drug Deliv. Rev.* **2016**, *100*, 27–50.
[195] D. E. Dobry, D. M. Settell, J. M. Baumann, R. J. Ray, L. J. Graham, R. A. Beyerinck, *J. Pharm. Innov.* **2009**, *4*, 133–142.
[196] R. Vehring, W. R. Foss, D. Lechuga-Ballesteros, *J. Aerosol Sci.* **2007**, *38*, 728–746.
[197] M. Mezhericher, A. Levy, I. Borde, *Dry. Technol.* **2007**, *25*, 1025–1032.
[198] X. An, F. Liu, Y. J. Jung, S. Kar, *Nano Lett.* **2013**, *13*, 909–916.
[199] D. S. Jung, T. H. Hwang, S. Bin Park, J. W. Choi, *Nano Lett.* **2013**, *13*, 2092–2097.
[200] A. B. D. Nandiyanto, A. Suhendi, T. Ogi, R. Umemoto, K. Okuyama, *Chem. Eng. J.* **2014**, *256*, 421–430.
[201] A. B. D. Nandiyanto, K. Okuyama, *Indones. J. Sci. Technol.* **2017**, *2*, 152.
[202] A. B. D. Nandiyanto, A. Suhendi, O. Arutanti, T. Ogi, K. Okuyama, *Langmuir* **2013**, *29*, 6262–6270.
[203] A. B. D. Nandiyanto, A. Suhendi, T. Ogi, T. Iwaki, K. Okuyama, *Colloids Surfaces A Physicochem. Eng. Asp.* **2012**, *396*, 96–105.
[204] A. B. D. Nandiyanto, N. Hagura, F. Iskandar, K. Okuyama, *Acta Mater.* **2010**, *58*, 282–289.
[205] A. Suhendi, A. B. D. Nandiyanto, M. M. Munir, T. Ogi, L. Gradon, K. Okuyama, *Langmuir* **2013**, *29*, 13152–13161.
[206] N. Hagura, A. B. D. Nandiyanto, F. Iskandar, K. Okuyama, *Chem. Lett.* **2009**, *38*, 1076–1077.
[207] P. Walzel, *Chem. Eng. & Technol.* **2011**, *34*, 1039–1048.
[208] B. Bhandari, *Dry. Technol.* **2015**, *33*, 128–129.
[209] W. D. Wu, K. C. Patel, S. Rogers, X. D. Chen, *Dry. Technol.* **2007**, *25*, 1907–1916.
[210] C. Clanet, J. C. Lasheras, *J. Fluid Mech.* **1999**, *383*, 307–326.
[211] W. N. Wang, A. Purwanto, I. W. Lenggoro, K. Okuyama, H. Chang, H. D. Jang, *Ind. & Eng. Chem. Res.* **2008**, *47*, 1650–1659.
[212] J. Vicente, J. Pinto, J. Menezes, F. Gaspar, *Powder Technol.* **2013**, *247*, 1–7.
[213] P. Schuck, R. Jeantet, B. Bhandari, X. D. Chen, Í. T. Perrone, A. F. de Carvalho, M. Fenelon, P. Kelly, *Dry. Technol.* **2016**, *34*, 1773–1790.
[214] D. L. Pearce, *Dry. Technol.* **2006**, *24*, 777–781.
[215] E. M. Both, A. M. Karlina, R. M. Boom, M. A. I. Schutyser, *Food Hydrocoll.* **2018**, *75*, 202–210.
[216] C. Sadek, P. Schuck, Y. Fallourd, N. Pradeau, C. Le Floch-Fouéré, R. Jeantet, *Dairy Sci. Technol.* **2015**, *95*, 771–794.
[217] M. G. Abiad, O. H. Campanella, M. T. Carvajal, *Int. J. Food Prop.* **2014**, *17*, 1303–1316.
[218] M. Mezhericher, A. Levy, I. Borde, *Chem. Eng. Sci.* **2011**, *66*, 884–896.
[219] J. C. Lin, J. W. Gentry, *Aerosol Sci. Technol.* **2003**, *37*, 15–32.
[220] R. Mondragon, L. Hernandez, J. Enrique Julia, J. Carlos Jarque, S. Chiva, B. Zaitone, C. Tropea, *Chem. Eng. Sci.* **2011**, *66*, 2734–2744.
[221] M. Griesing, H. Grosshans, T. Hellwig, R. Sedelmayer, S. R. Gopireddy, W. Pauer, E. Gutheil, H.-U. Moritz, *Chemie Ing. Tech.* **2016**, *88*, 929–936.
[222] E. M. Littringer, A. Mescher, S. Eckhard, H. Schröttner, C. Langes, M. Fries, U. Griesser, P. Walzel, N. A. Urbanetz, *Dry. Technol.* **2012**, *30*, 114–124.
[223] I. C. Kemp, D. E. Oakley, *Dry. Technol.* **2002**, *20*, 1699–1750.
[224] I. C. Kemp, T. Hartwig, R. Herdman, P. Hamilton, A. Bisten, S. Bermingham, *Dry. Technol.* **2016**, *34*, 1243–1252.
[225] M. Mezhericher, A. Levy, I. Borde, *Dry. Technol.* **2008**, *26*, 265–282.
[226] G. Finotello, J. T. Padding, K. A. Buist, A. Jongsma, F. Innings, J. A. M. Kuipers, *Int. J. Multiph. Flow* **2019**, *114*, 154–167.
[227] M. Dosta, J. D. Litster, S. Heinrich, *Adv. Powder Technol.* **2020**, *31*, 947–953.
[228] M. Mezhericher, A. Levy, I. Borde, *Chem. Eng. Process. Process Intensif.* **2010**, *49*, 1205–1213.
[229] K. Patel, X. Chen, *J. Food Process Eng.* **2005**, *28*, 567–594.
[230] S. Wang, T. A. G. Langrish, *Adv. Powder Technol.* **2009**, *20*, 220–226.
[231] W. Ranz, W. Marshall, *Chem. Eng. Prog.* **1952**, *48*, 141–146.
[232] M. Mezhericher, A. Levy, I. Borde, *Dry. Technol.* **2010**, *28*, 278–293.
[233] T. A. G. Langrish, T. K. Kockel, *Chem. Eng. J.* **2001**, *84*, 69–74.
[234] T. A. G. Langrish, *Chem. Eng. J.* **2008**, *137*, 677–680.
[235] X. D. Chen, S. X. Q. Lin, *AIChE J.* **2005**, *51*, 1790–1799.
[236] S. X. Q. Lin, X. D. Chen, *Dry. Technol.* **2006**, *24*, 1329–1334.
[237] X. D. Chen, G. Z. Xie, *Food Bioprod. Process.* **1997**, *75*, 213–222.
[238] S. X. Q. Lin, X. D. Chen, *Dry. Technol.* **2005**, *23*, 1395–1406.
[239] S. X. Q. Lin, X. D. Chen, *Chem. Eng. Process. Process Intensif.* **2007**, *46*, 437–443.
[240] K. C. Patel, X. D. Chen, *Food Bioprod. Process.* **2008**, *86*, 185–197.
[241] K. Patel, X. Chen, *Dry. Technol. – DRY TECHNOL* **2008**, *26*, 1334–1343.
[242] A. R. Abrahamsen, D. Geldart, *Powder Technol.* **1980**, *26*, 35–46.
[243] I. Golovin, G. Strenzke, R. Dürr, S. Palis, A. Bück, E. Tsotsas, A. Kienle, *Processes* **2018**, *6*, 246.
[244] E. Diez, K. Meyer, A. Bück, E. Tsotsas, S. Heinrich, *Chem. Eng. Res. Des.* **2018**, *139*, 104–115.
[245] J. Du, A. Bück, E. Tsotsas, *Powder Technol.* **2020**, *363*, 195–206.
[246] A. K. Singh, E. Tsotsas, *Powder Technol.* **2020**, *364*, 417–428.
[247] C. A. M. da Silva, J. J. Butzge, M. Nitz, O. P. Taranto, *Adv. Powder Technol.* **2014**, *25*, 195–210.
[248] L. Mörl, S. Heinrich, M. Peglow, in *Granulation* (Eds: A. D. Salman, M. J. Hounslow, J. P. K. Seville), Elsevier Science, Amsterdam, the Netherland, B.V **2007**, pp. 21–188.
[249] C. P. Coronel-Aguilera, M. F. San Martín-González, *LWT – Food Sci. Technol.* **2015**, *62*, 187–193.
[250] A. M. Alkadhem, H. O. Mohamed, S. R. Kulkarni, T. Hoffmann, D. Zapater, V. E. Musteata, E. Tsotsas, P. Castaño, *Powder Technol.* **2024**, *438*, 119602.
[251] G. Grünewald, B. Westhoff, M. Kind, *Dry. Technol.* **2010**, *28*, 349–360.
[252] M. Peglow, U. Cunäus, E. Tsotsas, *Chem. Eng. Sci.* **2011**, *66*, 1916–1922.
[253] G. I. Tardos, M. I. Khan, P. R. Mort, *Powder Technol.* **1997**, *94*, 245–258.
[254] M. Hemati, R. Cherif, K. Saleh, V. Pont, *Powder Technol.* **2003**, *130*, 18–34.
[255] Y. Chen, J. Yang, R. N. Dave, R. Pfeffer, *Powder Technol.* **2009**, *191*, 206–217.
[256] T. Schaefer, *Arch. Pharm. Chem. Sci.* **1977**, *5*, 51–60.
[257] L. Benelli, D. F. Cortés-Rojas, C. R. F. Souza, W. P. Oliveira, *Powder Technol.* **2015**, *273*, 145–153.
[258] R. Sukarsono, S. Riyadi, D. H. S. Rinanti, *J. Phys. Conf. Ser.* **2019**, *1198*, 22079.
[259] J. B. Gegenheimer, Modellierung der Agglomeration in der Wirbelschichtgranulation; Dissertation, Karlsruher Institut für Technologie (KIT), Karlsruhe, Germany, **2017**.
[260] M. Liu, B. Liu, Y. Shao, J. Wang, *Nucl. Eng. Des.* **2014**, *271*, 68–72.

[261] D. P. S. W. J. Lackey, J. D. Sease, *Nucl. Technol.* **1977**, *35*, 227–237.
[262] W. L. Davies, W. T. Gloor, *J. Pharm. Sci.* **1971**, *60*, 1869–1874.
[263] M. Foroughi-Dahr, N. Mostoufi, R. Sotudeh-Gharebagh, J. Chaouki, in *Ref. Modul. Chem. Mol. Sci. Chem. Eng.*, Elsevier, Amsterdam **2017**.
[264] A. Palamanit, S. Prachayawarakorn, P. Tungtrakul, S. Soponronnarit, *Food Bioprocess Technol.* **2016**, *9*, 1317–1326.
[265] D. M. Jones, in *Flavor Encapsulation*, American Chemical Society, Washington, DC **1988**, pp. 17–158.
[266] *Handbook of Fluidization and Fluid-Particle Systems* (Ed: W. C. Yang), CRC Press, Boca Raton, FL **2003**.
[267] D. Jones, *Drug Dev. Ind. Pharm.* **1994**, *20*, 3175–3206.
[268] A. Faure, P. York, R. C. Rowe, *Eur. J. Pharm. Biopharm.* **2001**, *52*, 269–277.
[269] D. E. Wurster, *J. Am. Pharm. Assoc. (Scientific ed.)* **1959**, *48*, 451–454.
[270] K. Dewettinck, A. Huyghebaert, *Trends Food Sci. Technol.* **1999**, *10*, 163–168.
[271] F. N. Christensen, P. Bertelsen, *Drug Dev. Ind. Pharm.* **1997**, *23*, 451–463.
[272] X. X. Cheng, R. Turton, *Pharm. Dev. Technol.* **2000**, *5*, 323–332.
[273] S. Shelukar, J. Ho, J. Zega, E. Roland, N. Yeh, D. Quiram, A. Nole, A. Katdare, S. Reynolds, *Powder Technol.* **2000**, *110*, 29–36.
[274] Fluid Bed Technology, https://foodfeedfinechemicals.glatt.com/technology-know-how/technologies/fluid-bed-technology/, **n.d.**
[275] M. E. S. L. Z. C. Vecchio F. Fabiani, A. Gazzaniga, *Drug Dev. Ind. Pharm.* **1998**, *24*, 269–274.
[276] G. Strenzke, R. Dürr, A. Bück, E. Tsotsas, *Powder Technol.* **2020**, *375*, 210–220.
[277] T. Charinpanitkul, W. Tanthapanichakoon, P. Kulvanich, K.-S. Kim, *J. Ind. Eng. Chem.* **2008**, *14*, 661–666.
[278] H. S. Tan, A. D. Salman, M. J. Hounslow, *Chem. Eng. Sci.* **2006**, *61*, 1585–1601.
[279] U. Vengateson, R. Mohan, *Resour. Technol.* **2016**, *2*, S124–S135.
[280] A. Rozhkov, B. Prunet-Foch, M. Vignes-Adler, *Phys. Fluids* **2003**, *15*, 2006–2019.
[281] J. Bouffard, M. Kaster, H. Dumont, *Drug Dev. Ind. Pharm.* **2005**, *31*, 923–933.
[282] P. Munnik, P. E. de Jongh, K. P. de Jong, *Chem. Rev.* **2015**, *115*, 6687–6718.
[283] X. Liu, J. G. Khinast, B. J. Glasser, *Chem. Eng. Sci.* **2008**, *63*, 4517–4530.
[284] W. M. H. Sachtler, G. Schulz-Ekloff, S. Ernst, J. J. Friplat, K. Tanabe, H. Hattori, J. F. Le Page, M. Baerns, E. Körting, in *Handb. Heterog. Catal.*, John Wiley & Sons, Ltd, Chichester **1997**, pp. 365–426.
[285] A. Lekhal, B. J. Glasser, J. G. Khinast, *Chem. Eng. Sci.* **2001**, *56*, 4473–4487.
[286] S.-Y. Lee, R. Aris, *Catal. Rev.* **1985**, *27*, 207–340.
[287] S. Melis, A. Varma, C. J. Pereira, *Chem. Eng. Sci.* **1997**, *52*, 165–169.
[288] R. Baratti, V. Feckova, M. Morbidelli, A. Varma, *Ind. Eng. Chem. Res.* **1997**, *36*, 3416–3420.
[289] E. R. Becker, J. Wei, *J. Catal.* **1977**, *46*, 365–371.
[290] R. T. Zimmermann, S. Weber, J. Bremer, V. Idakiev, R. Pashminehazar, T. L. Sheppard, L. Mörl, K. Sundmacher, *Chem. Eng. J.* **2023**, *457*, 140921.
[291] R. T. Zimmermann, K. Sundmacher, *Ind. Eng. Chem. Res.* **2024**, *63*, 7556–7564.
[292] L. Barthe, S. Desportes, M. Hemati, K. Philippot, B. Chaudret, *Chem. Eng. Res. Des.* **2007**, *85*, 767–777.
[293] L. Barthe, M. Hemati, K. Philippot, B. Chaudret, *Chem. Eng. Res. Des.* **2008**, *86*, 349–358.
[294] S. Desportes, D. Steinmetz, M. Hémati, K. Philippot, B. Chaudret, *Powder Technol.* **2005**, *157*, 12–19.
[295] G. Lezcano, S. R. Kulkarni, V. K. Velisoju, V. E. Musteata, I. Hita, A. Ramirez, A. Dikhtiarenko, J. Gascon, P. Castaño, *Mol. Catal.* **2022**, *527*, 112399.
[296] L. Barthe, K. Philippot, B. Chaudret, N. Le Bolay, M. Hemati, *Powder Technol.* **2014**, *257*, 198–202.
[297] L. Barthe, S. Desportes, D. Steinmetz, M. Hemati, *Chem. Eng. Res. Des.* **2009**, *87*, 915–922.
[298] A. H. Ahmadi Motlagh, K. Pougatch, A. Maturi, M. Salcudean, J. R. Grace, D. Grecov, J. McMillan, *Ind. Eng. Chem. Res.* **2019**, *58*, 4396–4411.
[299] Z. Jiang, C. Rieck, A. Bück, E. Tsotsas, *Chem. Eng. Sci.* **2020**, *211*, 115289.
[300] Z. Jiang, C. Rieck, A. Bück, E. Tsotsas, **2018**.
[301] K. Terrazas-Velarde, M. Peglow, E. Tsotsas, *Chem. Eng. Sci.* **2009**, *64*, 2631–2643.
[302] Z. Y. Zhou, S. B. Kuang, K. W. Chu, A. B. Yu, *J. Fluid Mech.* **2010**, *661*, 482–510.
[303] J. Kumar, M. Peglow, G. Warnecke, S. Heinrich, L. Mörl, *Chem. Eng. Sci.* **2006**, *61*, 3327–3342.
[304] K. Liffman, *J. Comput. Phys.* **1992**, *100*, 116–127.
[305] Y. Lin, K. Lee, T. Matsoukas, *Chem. Eng. Sci.* **2002**, *57*, 2241–2252.
[306] A. K. Singh, E. Tsotsas, *Powder Technol.* **2019**, *355*, 449–460.
[307] M. A. de Pastre, Y. Quinsat, C. Lartigue, *Int. J. Interact. Des. Manuf.* **2022**, *16*, 1471–1496.
[308] H. N. Chia, B. M. Wu, *J. Biol. Eng.* **2015**, *9*, 4.
[309] N. Labonnote, A. Rønnquist, B. Manum, P. Rüther, *Autom. Constr.* **2016**, *72*, 347–366.
[310] A. Le-Bail, B. C. Maniglia, P. Le-Bail, *Curr. Opin. Food Sci.* **2020**, *35*, 54–64.
[311] I. Astm, *Addit. Manuf. Princ. Vocab. ASTM West Conshohocken*, PA, USA **2021**.
[312] R. Melentiev, G. Harakály, J. Stögerer, G. Mitteramskogler, A. Wagih, G. Lubineau, C. A. Grande, *Addit. Manuf.* **2024**, *85*, 104156.
[313] S. Nohut, J. Schlacher, I. Kraleva, M. Schwentenwein, R. Bermejo, *Int. J. Appl. Ceram. Technol.* **2024**, *21*, 89–104.
[314] Carbon Dioxide Capture for Storage in Deep Geologic Formations: Results from the CO^2 Capture Project Volume Five: CCS Technology Development and Demonstration Results 2015-2022, IEAGHG/CO^2 Capture Project (Ed: K. F. Gerdes) London, UK **2022**.
[315] O. Santoliquido, G. Bianchi, P. Dimopoulos Eggenschwiler, A. Ortona, *Int. J. Appl. Ceram. Technol.* **2017**, *14*, 1164–1173.
[316] J. A. Gonzalez, J. Mireles, Y. Lin, R. B. Wicker, *Ceram. Int.* **2016**, *42*, 10559–10564.
[317] M. Pelanconi, P. Blyweert, G. Bianchi, V. Nicolas, D. Viganò, S. Bottacin, V. Fierro, A. Celzard, A. Ortona, *Carbon N. Y.* **2023**, *213*, 118252.
[318] A. Lind, Ø. Vistad, M. F. Sunding, K. A. Andreassen, J. H. Cavka, C. A. Grande, *Mater. Des.* **2020**, *187*, 108377.
[319] C. Busse, H. Freund, W. Schwieger, *Chem. Eng. J.* **2024**, *489*, 151139.
[320] J. N. Stuecker, J. E. Miller, R. E. Ferrizz, J. E. Mudd, J. Cesarano, *Ind. Eng. Chem. Res.* **2004**, *43*, 51–55.
[321] M. A. S. R. Saadi, A. Maguire, N. T. Pottackal, M. S. H. Thakur, M. M. Ikram, A. J. Hart, P. M. Ajayan, M. M. Rahman, *Adv. Mater.* **2022**, *34*, 2108855.
[322] M. L. Griffith, L. D. Harwell, J. T. Romero, E. Schlienger, C. L. Atwood, J. E. Smugeresky, In Proceedings of the Solid Freeform Fabrication Symposium, Univ. Texas Austin TX, **1997**, pp 387-393.
[323] H. Maleki, V. Bertola, *Catal. Sci. Technol.* **2020**, *10*, 3140–3159.
[324] Y. He, C. J. Tuck, E. Prina, S. Kilsby, S. D. R. Christie, S. Edmondson, R. J. M. Hague, F. R. A. J. Rose, R. D. Wildman, *J. Biomed. Mater. Res. Part B Appl. Biomater.* **2017**, *105*, 1645–1657.
[325] ohnson M. Group, CATACEL SSR catalyst for steam reforming, https://matthey.com/products-and-markets/chemicals/catacel-ssr-catalyst-steam-reforming, **2018**.
[326] S. Subhadarshini, K. Ghosh, M. Pumera, *Mater. Today* **2024**, *74*, 34–45.
[327] Z. Wu, J. Xu, P. Guo, L. Ding, Q. Li, Y. Wang, *Chem. Eng. J.* **2025**, *505*, 159757.
[328] J. Sheng, M. Gao, N. Zhao, K. Zhao, Y. Shi, W. Wang, *Fuel* **2025**, *382*, 133703.
[329] S. Reid, F. Lecarpentier, D. Symons, M. Watson, *Chem. Eng. Sci.* **2025**, *302*, 120783.
[330] M. Khakzad, Z. Sepasi, M. Mosadegh, Z. Alsup, M. Minary-Jolandan, *Ceram. Int.* **2025**, *51*, 19355–19365.
[331] A. Ortona, C. D'Angelo, S. Gianella, D. Gaia, *Mater. Lett.* **2012**, *80*, 95–98.
[332] Y. Kang, J. Cai, L. Zhang, H.-W. Wang, R.-B. Jin, Y. de Rancourt de Mimérand, X. Jin, J. Guo, *ACS Appl. Mater. Interfaces* **2023**, *15*, 31849–31866.
[333] H. M. Bui, P. F. Großmann, T. Gros, M. Blum, A. Berger, R. Fischer, N. Szesni, M. Tonigold, O. Hinrichsen, *Appl. Catal. A Gen.* **2022**, *643*, 118760.
[334] H. M. Bui, P. F. Großmann, A. Berger, A. Seidel, M. Tonigold, N. Szesni, R. Fischer, B. Rieger, O. Hinrichsen, *Chem. Eng. J.* **2023**, *458*, 141361.
[335] H. M. Bui, T. Kratky, I. Lee, R. Khare, M. Hiller, S. Wedig, S. Günther, O. Hinrichsen, *Catal. Commun.* **2023**, *182*, 106738.
[336] S. Maleksaeedi, H. Eng, F. E. Wiria, T. M. H. Ha, Z. He, *J. Mater. Process. Technol.* **2014**, *214*, 1301–1306.
[337] J. J. Bolívar Caballero, T. Han, R. Svanberg, I. N. Zaini, H. Yang, R. Gond, P. Cao, T. Lewin, P. G. Jönsson, W. Yang, *Energy Convers. Manag.* **2023**, *287*, 117071.

[338] C. Li, X. Yao, R. Zhang, H. Zheng, S. Yuan, X. Yu, B. Li, M. Zhu, S. T. Tu, *Chem. Eng. J.* **2024**, *487*, 150467.
[339] S. Chang, X. Huang, C. Y. Aaron Ong, L. Zhao, L. Li, X. Wang, J. Ding, *J. Mater. Chem. A* **2019**, *7*, 18338–18347.
[340] Y. De Vos, A. J. J. Koekkoek, G. Bonura, S. Todaro, M. Kus, A. Vansant, G. Gerritsen, C. Cannilla, H. C. L. Abbenhuis, V. Middelkoop, *Mater. Sci. Eng. B* **2024**, *310*, 117759.
[341] X. Xu, B. He, Y. Wang, Y. Xi, D. Liu, Z. Ji, L. Bai, F. Dong, Z. Lu, X. Wang, *Chem. Eng. J.* **2023**, *474*, 145504.
[342] J. Luyten, S. Mullens, I. Thijs, *KONA Powder Part. J.* **2010**, *28*, 131–142.
[343] K. Li, Y. Zhang, W. Shen, Z. Liu, Q. Ma, J. Zhang, F. Luo, *Fuel* **2025**, *380*, 133129.
[344] A. G. Hasib, S. Niauzorau, W. Xu, S. Niverty, N. Kublik, J. Williams, N. Chawla, K. Song, B. Azeredo, *Addit. Manuf.* **2021**, *41*, 101967.
[345] Y. Zhou, O. A. Qamar, G. Byoung Hwang, C. Knapp, G. Li, G. Lubineau, Y. Tai, *Chem. Eng. J.* **2024**, *500*, 157336.
[346] J. I. I. I. Cesarano, T. A. Baer, P. Calvert, *Recent Developments in Freeform Fabrication of Dense Ceramics from Slurry Deposition*, Sandia National Laboratories, Albuquerque, NM, United States **1997**.
[347] I. I. J. Cesarano, P. D. Calvert, (Albuquerque, NM), *Freeforming Objects with Low-Binder Slurry*, Sandia National Laboratories, Albuquerque, NM **2000**.
[348] M. Furman, S. Corbel, G. Wild, O. Zahraa, *Chem. Eng. Process. Process Intensif.* **2010**, *49*, 35–41.
[349] Z. Wang, J. Wang, M. Li, K. Sun, C. Liu, *Sci. Rep.* **2014**, *4*, 5939.
[350] A. Ambrosi, J. G. S. Moo, M. Pumera, *Adv. Funct. Mater.* **2016**, *26*, 698–703.
[351] C. Parra-Cabrera, C. Achille, S. Kuhn, R. Ameloot, *Chem. Soc. Rev.* **2018**, *47*, 209–230.
[352] C. Tinajero, G. Palmara, M. Zanatta, V. Sans, *Chem. Eng. J.* **2025**, *505*, 159442.
[353] S. Reid, F. Lecarpentier, D. Symons, M. Watson, *Catal. Today* **2023**, *418*, 114155.
[354] J. C. Martínez-Fuentes, I. Martínez-López, J. Bueno-Ferrer, G. G. Pastor, E. Guillén-Bas, A. Davó-Quiñonero, D. Lozano-Castelló, A. Bueno-López, *J. CO2 Util.* **2024**, *88*, 102951.
[355] B. Hüner, N. Demir, M. Fatih Kaya, *Fuel* **2024**, *366*, 131172.
[356] I. Martínez-López, A. Davó-Quiñonero, E. Guillén-Bas, I. Martín-García, E. Bailón-García, D. Lozano-Castelló, A. Bueno-López, *ChemCatChem* **2025**, *17*, e202401806.
[357] R. Meng, Y. Jiang, J. Jiang, J. Liu, C. Kong, Z. Zhang, *Fuel* **2025**, *391*, 134727.
[358] Y. Jiang, J. Jiang, R. Meng, C. Kong, Z. Zhang, Y. Liao, *Sep. Purif. Technol.* **2025**, *360*, 131230.
[359] G. Bonura, S. Todaro, V. Middelkoop, Y. de Vos, H. C. L. Abbenhuis, G. Gerritsen, A. J. J. Koekkoek, C. Cannilla, F. Frusteri, *J. CO2 Util.* **2023**, *70*, 102458.
[360] Y. Wang, S. Lin, M. Li, C. Zhu, H. Yang, P. Dong, M. Lu, W. Wang, J. Cao, Q. Liu, X. Feng, H. Hu, N. Tsubaki, M. Wu, *Appl. Catal. B Environ.* **2024**, *340*, 123211.
[361] K. Baamran, S. Lawson, A. A. Rownaghi, F. Rezaei, *JACS Au* **2024**, *4*, 101–115.
[362] J. Ma, W. Guo, C. Ni, X. Chen, W. Li, J. Zheng, W. Chen, Z. Luo, J. Wang, Y. Guo, *Environ. Sci. Technol.* **2024**, *58*, 12189–12200.
[363] Y. Wei, S. Wang, M. Chen, J. Han, G. Yang, Q. Wang, J. Di, H. Li, W. Wu, J. Yu, *Adv. Mater.* **2024**, *36*, 2302912.
[364] L. Long, K. Xu, K. Bing Tan, D. Cai, Y. Yang, S.-F. Zhou, G. Zhan, *Chem. Eng. Sci.* **2023**, *266*, 118278.
[365] X. Guo, C. Chen, H. Jiao, W. Wu, Y. Jin, Z. Liang, B. Jiang, *Ind. Crops Prod.* **2025**, *225*, 120513.
[366] Z. Yang, X. Yang, M. Zhu, Y. Niu, C. Zhang, P. Li, Y. Zhang, Z. Xu, Q. Li, *Appl. Catal. B Environ.* **2023**, *331*, 122646.
[367] R. Xing, R. Huang, R. Su, J. Kong, M. D. Dickey, W. Qi, *Chem Bio Eng.* **2024**, *1*, 264–273.
[368] F. Xie, X. Cui, X. Zhi, D. Yao, B. Johannessen, T. Lin, J. Tang, T. B. F. Woodfield, L. Gu, S. Z. Qiao, *Nat. Synth.* **2023**, *2*, 129–139.
[369] C. Huo, Z. Qiu, Z. Wei, X. Tian, X. Huang, Y. Nan, Y. Xiang, R. Zhang, Z. Wu, D. Li, *Addit. Manuf.* **2024**, *80*, 103962.
[370] J. Zhu, J. Liu, J. Zhu, S. Lu, R. Yan, K. Cheng, H. Cheng, H. Liu, H. Li, W. Zhu, *Inorg. Chem.* **2023**, *62*, 20050–20061.
[371] P. Balla, D. Shin, S.-J. Park, G. Kwak, S. Kim, *Fuel* **2025**, *390*, 134772.
[372] W. Chen, Y. Wu, J. He, W. Jiang, X. She, Y. Song, H. Ji, H. Xu, H. Li, *Ceram. Int.* **2024**, *50*, 10990–11002.
[373] A. Pajares, J. Andrade-Arvizu, D. Jain, M. Monai, J. Lefevere, P. R. de la Piscina, N. Homs, B. Michielsen, *Chem. Eng. J.* **2024**, *482*, 149048.
[374] C. Jacquot, A. Vamvakeros, A. Pavlišič, S. W. T. Price, H. Dong, D. Matras, L. Protasova, B. Likozar, S. D. M. Jacques, A. M. Beale, V. Middelkoop, *Chem. Eng. J. Adv.* **2023**, *16*, 100538.
[375] M. Rebber, H. Sannemüller, M. Jaruszewski, D. Pfannkuche, A. Urakawa, D. Koziej, *Chem. Mater.* **2023**, *35*, 3849–3858.
[376] S. Zhang, J. Shen, P. Zhang, T. B. H. Schroeder, J. Chen, C. Carnevale, S. Salmon, X. Fang, *Adv. Mater. Technol.* **2024**, *9*, 2400025.
[377] N. Weber, M. Möntmann, M. Wessling, R. Keller, *Chem. Eng. J.* **2024**, *486*, 150031.
[378] O. Bazta, F. J. Botana, J. J. Calvino, M. A. Cauqui, J. M. Gatica, H. Vidal, L. González-Rovira, J. López-Castro, M. P. Yeste, G. Blanco, J. C. Hernández-Garrido, *Chem. Eng. J.* **2025**, *506*, 159939.
[379] L. Zhang, H. Liu, B. Song, J. Gu, L. Li, W. Shi, G. Li, S. Zhong, H. Liu, X. Wang, J. Fan, Z. Zhang, P. Wang, Y. Yao, Y. Shi, J. Lu, *Nat. Commun.* **2024**, *15*, 2046.
[380] S. Guo, X. Gao, Y. Huang, R. Zhou, F. Chen, C. Cai, K. Zhou, R. Chen, *ACS ES&T Water* **2025**, *5*, 33–41.
[381] F. Pope, M. Fowler, D. Giesen, L. Drangai, G. Rothenberg, *Chem. Eng. & Technol.* **2024**, *47*, 932–939.
[382] K. Mori, T. Fujita, H. Hata, H.-J. Kim, T. Nakano, H. Yamashita, *ACS Appl. Mater. Interfaces* **2023**, *15*, 51079–51088.
[383] B. Guo, J. Lin, F. Mo, Y. Ding, T. Zeng, H. Liang, L. Wang, X. Chen, J. Mo, D. Li, H. Y. Yang, J. Bai, *Small* **2024**, *20*, 2312216.
[384] H.-J. Kim, K. Mori, T. Nakano, H. Yamashita, *Adv. Funct. Mater.* **2023**, *33*, 2303994.
[385] J. Tourneur, L. Joanny, L. Perrin, S. Paul, B. Fabre, *ACS Appl. Eng. Mater.* **2023**, *1*, 2676–2684.
[386] P. Guan, Y. Zhao, Y. Wu, W. Li, X. Zhang, X. Gao, X. Ou, W. S. Chai, Y. He, H. N. Li, *Mater. Today Sustain.* **2025**, *29*, 101086.
[387] M. Á. Gracia-Pinilla, N. A. Ramos-Delgado, C. Rosero-Arias, R. Sanders, S. Bartling, J. Winczewski, H. Gardeniers, A. Susarrey-Arce, *RSC Sustain.* **2024**, *2*, 3897–3908.
[388] P. Chen, X. Zhang, W. Wang, G. Xu, S. Dong, M. Cai, J.-C. Liu, J.-L. Song, *ChemNanoMat* **2024**, *10*, e202400469.
[389] G. Verma, M. Islam, A. Gupta, *Adv. Compos. Hybrid Mater.* **2025**, *8*, 109.
[390] L. Ding, H. Yan, L. Zhang, R. Bai, Q. Du, C. Xu, H. Gu, S. Guo, G. Cheng, Q. Fu, S. Liu, K. Yin, Q. Li, Y. Wang, *Adv. Energy Mater.* **2024**, *14*, 2402301.
[391] R. Wang, Y. Gong, P. Wang, W. He, Y. Song, M. Xin, Q. Jiang, Y. Sha, T. Cao, H. Song, W. Lin, *J. Mater. Chem. A* **2023**, *11*, 13945–13955.
[392] R. Wang, Y. Gong, P. Wang, A. Zheng, Z. Wang, Y. Sha, Q. Jiang, M. Xin, D. Cao, H. Song, W. Lin, *Addit. Manuf.* **2024**, *79*, 103890.
[393] L. Mastroianni, A. De Jesus Medina Ferrer, A. M. De Domenico, K. Eränen, M. Di Serio, D. Murzin, V. Russo, T. Salmi, *Chem. Eng. J.* **2024**, *501*, 157691.
[394] C. Gao, X. Li, W. Xu, Y. Chen, T. Luo, R. Gao, J. Cui, X. Chu, X. Wen, W. Zhou, *Addit. Manuf.* **2025**, *98*, 104644.
[395] M. Nowakowska, A. Rokicińska, P. Kuśtrowski, P. Michorczyk, *Ceram. Int.* **2023**, *49*, 1902–1910.
[396] L. Mastroianni, V. Russo, K. Eränen, M. Di Serio, D. Y. Murzin, T. Salmi, *Catal. Sci. Technol.* **2024**, *14*, 1336–1348.
[397] P. K. Rai, A. Singh, S. Bishwanathan, P. K. Gupta, D.-Y. Wang, M. Islam, A. Gupta, *Sci. Technol. Adv. Mater.* **2024**, *25*, 2421740.
[398] L. Ding, L. Zhang, G. Li, S. Chen, H. Yan, H. Tu, J. Su, Q. Li, Y. Tang, Y. Wang, *Energy & Environ. Mater.* **2024**, *7*, e12740.
[399] T. Y. K. Ho, K. S. Pung, D. W. H. Lock, Z. Du, C. L. Gan, *Adv. Funct. Mater.* **2024**, *34*, 2406132.
[400] J. Cai, X. Jiang, L. Zhang, B. Couturaud, W.-Z. Tang, Y.-Y. Zhang, R.-B. Jin, Y. de Rancourt de Mimérand, X. Jin, J. Guo, *ACS Appl. Nano Mater.* **2024**, *7*, 19936–19951.
[401] H. Dory, E. Petit, S. El-Sayegh, L. Badouric, V. Castro, M. Bechelany, D. Voiry, P. Miele, L. Lajaunie, C. Salameh, *Adv. Eng. Mater.* **2025**, *27*, 2401546.
[402] Y. Wu, J. He, W. Huang, W. Chen, S. Zhou, X. She, W. Zhu, F. Huang, H. Li, H. Xu, *Fuel* **2023**, *332*, 126021.
[403] Y. Wu, J. He, K. Zhong, S. Wang, X. Zhu, X. She, W. Jiang, H. Li, H. Xu, *Sep. Purif. Technol.* **2025**, *354*, 128399.

[404] J. Luo, V. Ruta, I. S. Kwon, J. Albertazzi, N. Allasia, O. Nevskyi, V. Busini, D. Moscatelli, G. Vilé, *Adv. Funct. Mater.* **2024**, *34*, 2404794.
[405] I. S. O. Barbosa, Y. A. Manrique, D. Paiva, J. L. Faria, R. J. Santos, C. G. Silva, *RSC Adv.* **2025**, *15*, 2275–2286.
[406] C. Busse, H. Freund, W. Schwieger, *Chem. Eng. Process. – Process Intensif.* **2018**, *124*, 199–214.
[407] A. Elkoro, L. Soler, J. Llorca, I. Casanova, *Appl. Mater. Today* **2019**, *16*, 265–272.
[408] M. Rebber, M. Trommler, I. Lokteva, S. Ehteram, A. Schropp, S. König, M. Fröba, D. Koziej, *Adv. Funct. Mater.* **2022**, *32*, 2112914.
[409] W. Guo, Y. Liu, Y. Sun, Y. Wang, W. Qin, B. Zhao, Z. Liang, L. Jiang, *Adv. Funct. Mater.* **2021**, *31*, 2100768.
[410] G. Pantoleontos, N. D. Vlachos, S. Lorentzou, G. Karagiannakis, N. I. Tsongidis, M. Syrigou, S. Gianella, L. Ferrari, A. Ortona, M. Pelanconi, *Chem. Eng. J. Adv.* **2023**, *16*, 100539.
[411] J. I. I. I. Cesarano, B. H. King, H. B. Denham, *Recent Developments in Robocasting of Ceramics and Composites*, Sandia National Laboratories, Albuquerque, NM, United States, **1998**.
[412] M. A. Jafari, W. Han, F. Mohammadi, A. Safari, S. C. Danforth, N. Langrana, *Rapid Prototyp. J.* **2000**, *6*, 161–175.
[413] J. W. Choi, H. C. Kim, R. Wicker, *J. Mater. Process. Technol.* **2011**, *211*, 318–328.
[414] V. G. Rocha, E. García-Tuñón, C. Botas, F. Markoulidis, E. Feilden, E. D'Elia, N. Ni, M. Shaffer, E. Saiz, *ACS Appl. Mater. Interfaces* **2017**, *9*, 37136–37145.
[415] C. Credi, R. Bernasconi, M. Levi, L. Magagnin, *J. Mater. Res. Technol.* **2023**, *22*, 1855–1867.
[416] I. Cazin, M. O. Gleirscher, M. Fleisch, M. Berer, M. Sangermano, S. Schlögl, *Addit. Manuf.* **2022**, *57*, 102977.
[417] N. Nekoonam, S. A. Sheikholeslami, S. Tisato, P. Zhu, R. Montazeri, Z. Hosneolfat, D. Helmer, *Addit. Manuf.* **2025**, *101*, 104713.
[418] Two-Photon Grayscale Lithography (2GL®) for prototyping and mastering Nanoscribe GmbH: Eggenstein-Leopoldshafen, Germany, https://www.nanoscribe.com/en/products/quantum-x/, (accessed October, 2025).
[419] K. Pongraktham, K. Somnuk, *ACS Omega* **2024**, *9*, 27578–27591.
[420] K. F. Jensen, *Chem. Eng. Sci.* **2001**, *56*, 293–303.
[421] V. Hessel, T. Noël, in *Ullmann's Encycl. Ind. Chem.*, Wiley-VCH Verlag GmbH & Co. KGaA, Weinheim, Germany **2012**.
[422] A. Gavriilidis, P. Angeli, E. Cao, K. K. Yeong, Y. S. S. Wan, *Chem. Eng. Res. Des.* **2002**, *80*, 3–30.
[423] M. I. Domínguez, M. A. Centeno, M. Martínez, T. L. F. Bobadilla, Ó. H. Laguna, J. A. Odriozola, *Chem. Eng. Res. Des.* **2021**, *171*, 13–35.
[424] J. Banhart, *Prog. Mater. Sci.* **2001**, *46*, 559–632.
[425] X. Zhang, J. Zhou, Y. Zheng, H. Wei, Z. Su, *Chem. Eng. J.* **2021**, *420*, 129700.
[426] V. Smeets, E. M. Gaigneaux, D. P. Debecker, *ChemCatChem* **2022**, *14*, e202101132.
[427] M. V Twigg, J. T. Richardson, *Ind. Eng. Chem. Res.* **2007**, *46*, 4166–4177.
[428] G. Zhao, J. A. Moulijn, F. Kapteijn, F. M. Dautzenberg, B. Xu, Y. Lu, *Catal. Rev.* **2024**, *66*, 1870–1950.
[429] X. Chen, J. Li, Y. Wang, Y. Zhou, Q. Zhu, H. Lu, *Appl. Catal. A Gen.* **2020**, *607*, 117839.
[430] Z. Li, B. Li, C. Yu, *Adv. Mater.* **2023**, *35*, 2211221.
[431] Y. Feng, Y. Ling, Y. Wang, P. Li, R. Xiao, G. Yang, T. Li, *Renew. Sustain. Energy Rev.* **2025**, *219*, 115846.
[432] T. Westermann, T. Melin, *Chem. Eng. Process. Process Intensif.* **2009**, *48*, 17–28.
[433] W. Yang, T. T. Fidelis, W.-H. Sun, *ACS Omega* **2020**, *5*, 83–88.
[434] H. Li, Y. Jiao, K. Davey, S. Z. Qiao, *Angew. Chemie* **2023**, *135*, e202216383.
[435] R. Gómez-Bombarelli, J. N. Wei, D. Duvenaud, J. M. Hernández-Lobato, B. Sánchez-Lengeling, D. Sheberla, J. Aguilera-Iparraguirre, T. D. Hirzel, R. P. Adams, A. Aspuru-Guzik, *ACS Cent. Sci.* **2018**, *4*, 268–276.
[436] C. Chen, S. P. Ong, *Nat. Comput. Sci.* **2022**, *2*, 718–728.
[437] B. Deng, P. Zhong, K. Jun, J. Riebesell, K. Han, C. J. Bartel, G. Ceder, *Nat. Mach. Intell.* **2023**, *5*, 1031–1041.
[438] A. Merchant, S. Batzner, S. S. Schoenholz, M. Aykol, G. Cheon, E. D. Cubuk, *Nature* **2023**, *624*, 80–85.
[439] L. Chanussot, A. Das, S. Goyal, T. Lavril, M. Shuaibi, M. Riviere, K. Tran, J. Heras-Domingo, C. Ho, W. Hu, A. Palizhati, A. Sriram, B. Wood, J. Yoon, D. Parikh, C. L. Zitnick, Z. Ulissi, *ACS Catal.* **2021**, *11*, 6059–6072.
[440] R. Tran, J. Lan, M. Shuaibi, B. M. Wood, S. Goyal, A. Das, J. Heras-Domingo, A. Kolluru, A. Rizvi, N. Shoghi, A. Sriram, F. Therrien, J. Abed, O. Voznyy, E. H. Sargent, Z. Ulissi, C. L. Zitnick, *ACS Catal.* **2023**, *13*, 3066–3084.
[441] S. Choung, W. Park, J. Moon, J. W. Han, *Chem. Eng. J.* **2024**, *494*, 152757.
[442] K. Broderick, E. Lopato, B. Wander, S. Bernhard, J. Kitchin, Z. Ulissi, *Appl. Catal. B Environ.* **2023**, *320*, 121959.
[443] T. Toyao, Z. Maeno, S. Takakusagi, T. Kamachi, I. Takigawa, K. Shimizu, *ACS Catal.* **2020**, *10*, 2260–2297.
[444] Shambhawi, O. Mohan, T. S. Choksi, A. A. Lapkin, *Catal. Sci. Technol.* **2024**, *14*, 515–532.
[445] X. Ma, Z. Li, L. E. K. Achenie, H. Xin, *J. Phys. Chem. Lett.* **2015**, *6*, 3528–3533.
[446] T. Toyao, K. Suzuki, S. Kikuchi, S. Takakusagi, K. Shimizu, I. Takigawa, *J. Phys. Chem. C* **2018**, *122*, 8315–8326.
[447] J. Noh, S. Back, J. Kim, Y. Jung, *Chem. Sci.* **2018**, *9*, 5152–5159.
[448] S. Shambhawi, G. Csányi, A. A. Lapkin, *Chemistry–Methods* **2021**, *1*, 444–450.
[449] M. M. Montemore, J. W. Medlin, *Catal. Sci. Technol.* **2014**, *4*, 3748–3761.
[450] R. A. Hoyt, M. M. Montemore, I. Fampiou, W. Chen, G. Tritsaris, E. Kaxiras, *J. Chem. Inf. Model.* **2019**, *59*, 1357–1365.
[451] O. Mamun, K. T. Winther, J. R. Boes, T. Bligaard, *npj Comput. Mater.* **2020**, *6*, 177.
[452] L. Grajciar, C. J. Heard, A. A. Bondarenko, M. V Polynski, J. Meeprasert, E. A. Pidko, P. Nachtigall, *Chem. Soc. Rev.* **2018**, *47*, 8307–8348.
[453] B. R. Goldsmith, J. Esterhuizen, J.-X. Liu, C. J. Bartel, C. Sutton, *AIChE J.* **2018**, *64*, 2311–2323.
[454] Z. Li, S. Wang, W. S. Chin, L. E. Achenie, H. Xin, *J. Mater. Chem. A* **2017**, *5*, 24131–24138.
[455] Z. W. Ulissi, M. T. Tang, J. Xiao, X. Liu, D. A. Torelli, M. Karamad, K. Cummins, C. Hahn, N. S. Lewis, T. F. Jaramillo, K. Chan, J. K. Nørskov, *ACS Catal.* **2017**, *7*, 6600–6608.
[456] R. Jinnouchi, R. Asahi, *J. Phys. Chem. Lett.* **2017**, *8*, 4279–4283.
[457] B. Blaiszik, L. Ward, M. Schwarting, J. Gaff, R. Chard, D. Pike, K. Chard, I. Foster, *MRS Commun.* **2019**, *9*, 1125–1133.
[458] J. R. Kitchin, *Nat. Catal.* **2018**, *1*, 230–232.
[459] Y. Y. Li, J. Bridgwater, *Powder Technol.* **2000**, *108*, 65–73.
[460] E. T. H. Olofsson, *Development of a Digital Twin of the Catalyst Extrusion Process from Combining Physics-Based and Data-Driven Models*, Technical University of Denmark, Kgs. Lyngby, Denmark **2023**.
[461] T. Savage, N. Basha, O. K. Matar, A. del Rio Chanona, in *33rd Eur. Symp. Comput. Aided Process Eng.* (Eds: A. C. Kokossis, M. C. Georgiadis, E. Pistikopoulos), Elsevier, Amsterdam **2023**, pp. 511–517.
[462] E. McGowan, V. Gawade, W. (Grace) Guo, *Sensors* **2022**, *22*, 494.
[463] K. Asami, M. Kuehne, T. Röver, C. Emmelmann, *Metals (Basel).* **2025**, *15*, 505.
[464] S. Wang, J. Di, D. Wang, X. Dai, Y. Hua, X. Gao, A. Zheng, J. Gao, *Pharmaceutics* **2022**, *14*, 183.
[465] S. Shirazian, M. Kuhs, S. Darwish, D. Croker, G. M. Walker, *Int. J. Pharm.* **2017**, *521*, 102–109.
[466] J. Lee, S. Hube, S. Elgeti, *Eng. Comput.* **2023**, *40*, 989–1004.
[467] R. Osen, U. Schweiggert-Weisz, in *Ref. Modul. Food Sci.*, Elsevier, Amsterdam **2016**.
[468] A. Das, E. L. Gilmer, S. Biria, M. J. Bortner, *ACS Appl. Polym. Mater.* **2021**, *3*, 1218–1249.
[469] A. R. Alves, M. F. Simões, S. Simões, J. Gomes, *Particuology* **2024**, *92*, 180–195.
[470] M. Singh, S. Shirazian, V. Ranade, G. M. Walker, A. Kumar, *Powder Technol.* **2022**, *403*, 117380.
[471] A. S. Galushko, V. P. Ananikov, *ACS Catal.* **2024**, *14*, 161–175.
[472] P. Xu, X. Ji, M. Li, W. Lu, *npj Comput. Mater.* **2023**, *9*, 42.
[473] E. Mäki-Lohiluoma, N. Säkkinen, M. Palomäki, O. Winberg, H. X. Ta, T. Heikkinen, E. Kiljunen, A. Kauppinen, *Int. J. Pharm.* **2021**, *609*, 121146.
[474] A. Nastaj, K. Wilczyński, *Polymers (Basel)* **2021**, *13*, 1547.
[475] J. Burr, A. Sarishvili, D. Just, N. Katsaouni, K. Moser, *Chemie Ing. Tech.* **2023**, *95*, 1555–1562.
[476] P. G. Smith, A. W. Nienow, *Chem. Eng. Sci.* **1983**, *38*, 1223–1231.

[477] M. Hussain, J. Kumar, M. Peglow, E. Tsotsas, *Chem. Eng. Sci.* **2013**, *101*, 35–45.
[478] M. J. Hounslow, R. L. Ryall, V. R. Marshall, *AIChE J.* **1988**, *34*, 1821–1832.
[479] S. Bhoi, S. R. Kolan, A. Bück, E. Tsotsas, *Powder Technol.* **2024**, *433*, 119271.
[480] I. Ali, *Adv. Contin. Discret. Model.* **2025**, *2025*, 12.
[481] M. Raissi, P. Perdikaris, G. E. Karniadakis, *J. Comput. Phys.* **2019**, *378*, 686–707.
[482] W. H. AlAlaween, M. Mahfouf, A. D. Salman, *Powder Technol.* **2016**, *302*, 265–274.
[483] J. A. Westerhuis, P. M. J. Coenegracht, C. F. Lerk, *Int. J. Pharm.* **1997**, *156*, 109–117.
[484] Y. Miyamoto, S. Ogawa, M. Miyajima, M. Matsui, H. Sato, K. Takayama, T. Nagai, *Int. J. Pharm.* **1997**, *149*, 25–36.
[485] E. Murtoniemi, J. Yliruusi, P. Kinnunen, P. Merkku, K. Leiviskä, *Int. J. Pharm.* **1994**, *108*, 155–164.
[486] H. Yu, J. Fu, L. Dang, Y. Cheong, H. Tan, H. Wei, *Ind. Eng. Chem. Res.* **2015**, *54*, 10825–10834.

Manuscript received: July 8, 2025
Revised manuscript received: September 24, 2025
Accepted manuscript online: September 30, 2025
Version of record online: ■■, ■■